THE ISO HANDBOOK

Volume II:

CAM – The ISO Camera

Joris Blommaert[1,2], Ralf Siebenmorgen[1], Alain Coulais[3], Leo Metcalfe[1], Marc-Antoine Miville-Deschênes[3], Koryo Okumura[3], Stephan Ott[1], Andy Pollock[1,4], Marc Sauvage[5] and Jean-Luc Starck[5]

SAI-99-057/Dc, Version 2.0

June, 2003

[1] ISO Data Centre, Astrophysics Division, Space Science Department of ESA, Villafranca del Castillo, P.O. Box 50727, E-28080 Madrid, Spain
[2] Instituut voor Sterrenkunde, Katholieke Universiteit Leuven, Celestijnenlaan 200B, B-3001 Leuven, Belgium
[3] Institut d'Astrophysique Spatiale, Université Paris XI, 91405 Orsay
[4] Computer & Scientific Co. Ltd., 230 Graham Road, Sheffield S10 3GS
[5] CEA, DSM/DAPNIA, CE-Saclay, F-91191 Gif-sur-Yvette, Cedex, France

Document Information

Document:	The ISO Handbook
Volume:	II
Title:	CAM – The ISO Camera
Reference Number:	SAI/99-057/Dc
Issue:	Version 2.0
Issue Date:	June 2003
Authors:	J. Blommaert, R. Siebenmorgen, A. Coulais et al.
Editors:	T. Müller, J. Blommaert & P. García-Lario
Web-Editor:	J. Matagne

Document History

The ISO Handbook, Volume II: CAM – The ISO Camera, is based on the following documents:

- The *ISOCAM Observer's Manual* (Version 1.0, March 1994), produced by the ISOCAM consortium.
- The *Addendum to the ISOCAM Observer's Manual* (SAI/96-160/Dc, Version 1.1, July 26, 1996), R.Siebenmorgen, M. Sauvage and D. Levine.
- The *ISOCAM Data Users Manual* (SAI/95-222/Dc, Version 4.0, December 1998), R. Siebenmorgen, J.-L. Starck, M. Sauvage, D.A. Cesarsky, J. Blommaert and S. Ott.
- Earlier versions of *The ISO Handbook on CAM – The ISO Camera* (previously called Volume III), SAI-99-057/Dc.
- All other documents listed in the Bibliography.

Document Change Record

Date	Revision	Comments
28/06/99	Draft 1.0	Draft Version 1.0 of ISO Handbook Volume III (CAM) for comments; Observer's Manual and Addendum merged with the IDUM information
16/07/99	Version 1.0	First version, related to OLP 8.0
15/11/00	Version 1.1	update, related to OLP 9.5
31/07/01	Version 1.2	update, related to OLP 10.0
17/06/02	Version 1.3	update, now Volume II
30/06/03	Version 2.0	update, printed version

Acknowledgments

ISOCAM would not have been the successful instrument it was without the enthusiastic and capable contribution of many colleagues in France and throughout Europe and the World (see the lists of co-investigators and laboratories).

The *Centre National d'Études Spatiales* (CNES) and the *Direction de Sciences de la Matière* of the *Commissariat à l'Energie Atomique* (DSM/CEA) are thanked for their support to build ISOCAM. Further funding was provided by the *Istituto di Tecnologie e Studio delle Radiazioni Extraterrestri* (TESRE) and the *Osservatorio Astronomico di Padova* (ground support equipment), as well as by the *Royal Observatory, Edinburgh* and the *Stockholm Observatory* (optical components).

The CEA and the *Centre National de la Recherche Scientifique* (CNRS) gave their generous support providing the personnel to build, test, and exploit the scientific and calibration results gathered during operations and for further understanding ISOCAM throughout the Post Operations Phase.

PI team and *European Space Agency* (ESA) personnel worked closely together during the Development Phase for testing and preparation of a wide range of in-flight procedures and command sequences. The joint PI/ESA Instrument Dedicated Team formed in those pre-launch times went on to maintain and calibrate the instrument through all aspects of its in-flight operations, closely supported by the 'home team' at CEA, Saclay and the *Institut d'Astrophysique Spatiale* (IAS), Orsay. Similar joint efforts sustained the Off-Line Processing (OLP) pipeline and CAM Interactive Analysis (CIA) development work. This collaborative approach persisted throughout the Post-Operations Phase.

Principal Investigator

Cesarsky, C. J. (SAp[1])

Co-investigators

The co-investigators played a central role in defining the technical characteristics of ISOCAM in order to carry out the science programmes agreed upon by all of them. The untimely death of Serge Cazes prevented him from celebrating the success of the mission with the rest of the ISOCAM team.

Cazes, S. (IAS)

Cesarsky, D. A. (IAS/MPE)

Chedin, A. (LMD)

Combes, M. (OPM)

Franceschini, A. (DAP)

Gorisse, M. (SAp)

Hawarden, T. (ROE)

Léna, P. (OPM)

Longair, M. S. (ROE)

Mandolesi, R. (TESRE)

Nordh, L. (SO)

Persi, P. (IAS-CNR)

Pérault, M. (ENS)

Rouan, D. (OPM)

Sargent, A. (CalTech)

[1] See the affiliation acronyms in the list of laboratories

Sibille, F. (OdL) Project Scientist.
Vigroux, L. (SAp)
Wade, R. (ROE)

Collaborators

Many people collaborated to define, build, test and use ISOCAM during Ground Testing, Performance Verification Phase and In-Orbit Operations; several of them continued their involvement throughout the three and a half years of the Post-Operations Phase.

Construction and Ground Calibration Phase

People listed here include those that participated in the mechanical, optical and cryo-mechanical studies that led to the definition of ISOCAM. as well as those who designed and built the on-board electronic subsystems, developed the on-board software and worked on the Ground Support Equipment. Others participated in the development of the extensive software systems and procedures later used for the in-flight calibration, system tests and uplink subsystems or in the Off-Line Processing (OLP) pipeline.

Abergel, A. (IAS) Ground calibration.
Agnese, P. (SAp) LW detector development and characterisation.
Altieri, B. (ESA) Operational Engineer and in-flight calibration.
Attad, E. (ROE) Optical design.
Auguéres, J-L. (SAp) Software development manager and pre-launch IDT leader.
Auternaud, D. (Aerospatiale Cannes) Team manager for construction and integration of ISOCAM.
Beresne, J. (OPM) SW electronic development.
Bonnal, J. (SAp) Mechanical subsystems and hardware.
Bortoletto, F. (OAP) Real time assessment software.
Bouère, A. (SAp) Electronic hardware.
Boulade, O. (SAp) Ground calibration and ground tests.
Cazes, S. (IAS) Optical studies and design of the ground calibration facilities.
Cesarsky, D. (IAS) PGA, ISOCAM simulator, RTA, QLA, CUS and OLP software.
Claret, A. (SAp) Ground calibration, in-flight calibration preparation and glitch models.
Cretolle, J. (SAp) Ground test equipment and on-board electronics.
Davies, J. (ROE) Characterisation of optical components.
Désert F-X. (IAS) Ground calibration, ISOCAM photometric model and ISOCAM Observers' Manual.
Doumayrou, E. (SAp) Ground tests and hardware.
Engelmann J-J. (SAp) Cosmic ray environment.
Epstein, G. (OPM) Ground test equipment and SW electronics development.
Gallais, P. (SAp) Ground calibration and QLA development.
Gastaud, R. (SAp) Development of QLA and CIA.
Gorisse, M. (SAp) Conceptual studies and LW detector.
Imbault, D. (SAp) ISOCAM team manager, construction phase.
Lapegue, J. (SAp) Quality assurance responsible, construction phase.
Metcalfe, L. (ESA) Responsible for in-flight calibration preparations, CUS.
Mosquet, N. (IAS) Ground calibration facilities.

Okumura, K. (ESA) In-flight calibration preparation.

Ott, S. (ESA) Responsible for CIA and OLP development.

Palazzi, E. (TESRE) Auto Analysis.

Pérault, M. (ENS) Responsible for ISOCAM's ground calibration, ISOCAM photometric model and ISOCAM Observers' Manual.

Perrier, F. (OPM) Configuration control and RTA/QLA software.

Poindron, E. (SAp) Development of the on-board software.

Pollock, A. (ESA/Computer & Scientific Co., UK) Software architect for Auto Analysis.

Puget, P. (OPM) Development of the Internal Calibration Device, in-flight calibration preparation.

Purkins, T. (ROE) Manager of the ROE team.

Rio, Y. (SAp) Development of real time software, PGA and ground tests.

Robert, T. (SAp) ISOCAM project controller.

Rouan, D. (OPM) SW detector development.

Roy, A. (SAp) Ground tests.

Saint-Pé, O. (OPM) Development of the Internal Calibration Device.

Sauvage, M. (SAp) ISOCAM Observer's Manual.

Sauvageon, A. (SAp) Uplink software.

Sibille, F. (OdL) Optical studies.

Siebenmorgen, R. (ESA) In-flight calibration preparation, user support.

Sirou, F. (LMD) Cryo-mechanics.

Soufflot, A. (IAS) Management of the ground calibration facility.

Sam-Lone, J. (ESA) Development of CIA.

Starck, J.L. (SAp) Development of CIA.

Tiphène, D. (OPM) SW detector development.

Ventura G. (TESRE) Spacecraft simulator and EGSE development.

Vigroux, L. (SAp) ISOCAM system engineer, ground calibration and pre-launch tests, in-flight calibration preparation.

Vivares, F. (IAS) Development of CIA.

Operations Phase

The following are the people who participated in the operational phase of ISOCAM. The list includes those actively involved with the day-to-day operations within the CAM Instrument Dedicated Team (CIDT) at VilSpa, and those in the 'home team' within the CAM Instrument Support Team (CIST) at CEA, Saclay and IAS, Orsay, and anyone that contributed to a better understanding of ISOCAM by producing software code used in CIA and/or the Off-Line Processing (OLP) pipeline.

Abergel, A. (IAS) Detector transient response corrections.

Altieri, B. (ESA) CIDT member, operational engineer, calibration.

Aussel, H. (SAp) CIST member, Calibration and development of data reduction algorithms.

Babar, A. (IPAC) CIA, calibration and development of data reduction algorithms.

Biviano, A. (OAT) CIDT member, calibration and development of data reduction algorithms.

Blommaert, J. (ESA) CIDT member, calibration and development of data reduction algorithms.

Bontemps, S. (SAp) Calibration and development of data reduction algorithms.

Boulade, O. (SAp) Early CIDT member, calibration and operational engineering, CIST member.
Boulanger, F. (IAS) Calibration and development of data reduction algorithms.
Cesarsky, D. (IAS) CIDT member during the PV Phase, CIST member, OLP software, head of the IAS ISO Centre
Claret, A. (SAp) Part-time CIDT, CIST, development of data reduction algorithms, glitch models.
Delaney, M. (ESA) CIA and development of data reduction algorithms, CIA User's Manual.
Delattre Ch. (SAp) Calibration and development of data reduction algorithms.
Désert F-X. (IAS) Calibration and development of data reduction algorithms.
Didelon, P. (SAp) ISOCAM database.
Dzitko, H. (SAp) CIST member, glitch models.
Elbaz, D. (SAp) CIST member, development of data reduction algorithms.
Fadda, D. (SAp) Development of data reduction algorithms.
Gallais, P. (SAp) CIDT member, RTA/QLA maintenance, instrument engineer.
Gastaud, R. (SAp) CIA development.
Guest, S. (RAL) CIDT member, CIA and OLP development.
Landriu, D. (SAp) CIA development.
Laurent, O. (SAp) CIST, calibration and development of data reduction algorithms.
Lemonon, L. (SAp) Development of data reduction algorithms.
Metcalfe, L. (ESA) Operational CIDT leader, calibration scientist.
Miville-Deschênes, M-A. (IAS) Calibration and development of data reduction algorithms.
Okumura, K. (ESA/IAS) CIDT member, calibration and development of data reduction algorithms.
Ott, S. (ESA) CIDT member, responsible for OLP and CIA development.
Pérault, M. (ENS) Calibration procedures and development.
Pollock, A. (ESA/Computer & Scientific Co., UK) Software architect for Auto Analysis pipeline.
Reach, W. (IAS) Calibration.
Román, P. (ESA) CIDT Member, calibration.
Roussel, H. (SAp) Development of data reduction algorithms.
Sauvage, M. (SAp) CIA software development, calibration and development of data reduction algorithms; head of the SAp ISO Centre
Sauvageon, A. (SAp) Early CIDT member, uplink software and configuration control.
Siebenmorgen, R. (ESA) CIDT member and ISOCAM resident astronomer, IDUM.
Starck, J.L. (SAp) CIA and development of data reduction algorithms, IDUM.
Tran, D. (SAp) Calibration and development of data reduction algorithms.
Vigroux, L. (SAp) CIDT during PV Phase, CIST, development of data reduction algorithms.

Post Operations Phase

The Post Operations phase lasted three and half years from mid-1998 until the end of 2001. During that period, both the CAM Interactive Analysis (CIA) and the Off-Line Processing (OLP) pipeline were improved and upgrades of the corpus of calibration files were performed. New algorithms were produced as a consequence of a better understanding of the behaviour of ISOCAM's detectors and the availability of more in-depth optical models.

Abergel, A. (IAS) Calibration and development of data reduction algorithms, transient response corrections

Aussel, H. (SAp) CIA, calibration and development of data reduction algorithms.
Babar, A. (IPAC) CIA, calibration and development of data reduction algorithms.
Blommaert, J. (ESA) Calibration and development of data reduction algorithms, CAM Handbook.
Bontemps, S. (SAp) Calibration and development of data reduction algorithms.
Boulanger, F. (IAS) Calibration and development of data reduction algorithms.
Cesarsky, D. (IAS/MPE) OLP software, POPS french manager and head of the IAS ISO Centre.
Chanial, P. (SAp) CIA development.
Coulais, A. (IAS) Calibration and development of data reduction algorithms, transient response corrections
Désert F-X. (IAS) Calibration and development of data reduction algorithms.
Delaney, M. (ESA) CIA Development.
Elbaz, D. (SAp) Calibration and development of data reduction algorithms.
Fadda, D. (SAp) Calibration and development of data reduction algorithms.
Fouks, B. (IAS,IREE) Calibration and development of data reduction algorithms, transient response corrections
Gastaud, R. (SAp) CIA and development of data reduction algorithms.
Guest, S. (RAL) CIA development.
Kong, M. (IPAC) Calibration and development of data reduction algorithms.
Landriu, D. (SAp) CIA development.
Laurent, O. (SAp) Calibration and development of data reduction algorithms.
Lemonon, L. (SAp) Calibration and development of data reduction algorithms.
Metcalfe, L. (ESA) Calibration and community support, ISG Leader.
Miville-Deschênes, M-A. (IAS) Calibration and development of data reduction algorithms.
Okumura, K. (ESA/IAS) Calibration and development of data reduction algorithms, ray-tracing model.
Ott, S. (ESA) POPS ISG-CAM leader, responsible for CIA development.
Pérault, M. (ENS) Calibration and development of data reduction algorithms.
Pollock, A. (Computer & Scientific Co., UK) Software Architect for Auto Analysis pipeline.
Román, P. (ESA) Calibration and development of data reduction algorithms.
Roussel, H. (SAp) Calibration and development of data reduction algorithms.
Sauvage, M. (SAp) Head of the SAp ISO Centre, POPS french co-manager, CIA software development.
Siebenmorgen, R. (ESA) CAM resident astronomer, CAM Handbook.
Starck, J.L. (SAp) Development of data reduction algorithms.
Tran, D. (SAp) Calibration and development of data reduction algorithms.
van Buren, D. (IPAC) Calibration and development of data reduction algorithms.
Võ, T. (ESA) Calibration development.
Wozniak, H. (ODM) Development of data reduction algorithms.

List of laboratories

CalTech (California Institute of Technology, USA)
CNES (Centre National d'Études Spatiales, Paris, France)
CNRS (Centre National de la Recherche Scientifique, France)
DAP (Dipartimento di Astronomia, Padova, Italy)

DSM/CEA (Direction de Sciences de la Matière/Commissariat à l'Energie Atomique, France)
ENS (École Normale Supérieure, France)
ESA-ESTEC (European Space Agency, ESTEC, The Netherlands)
ESA-VILSPA (European Space Agency, VILSPA, Spain)
IAS (Institut d'Astrophysique Spatiale, Orsay, France)
IAS-CNR (Istituto di Astrofisica Spaziale, Rome, Italy)
IPAC (Infrared Processing and Analysis Center, USA)
IREE (Institute of Radio Engineering and Electronics of Russian Academy of Sciences, Moscow, Russia)
LMD (Laboratoire de Météorologie Dynamique, France)
MPE (Max-Planck-Institut für extraterrestrische Physik, Germany)
OAP (Osservatorio Astronomico di Padova, Italy)
OAT (Osservatorio Astronomico di Trieste, Italy)
OdL (Observatoire de Lyon, France)
ODM (Observatoire de Marseille, France)
OPM (Observatoire de Paris-Meudon, France)
RAL (Rutherford Appleton Laboratories, UK)
ROE (Royal Observatory Edinburgh, Scotland)
SAp (Service d'Astrophysique, DAPNIA/CEA/Saclay, France)
SO (Stockholm Observatory, Sweden)
TESRE (Istituto di Tecnologie e Studio delle Radiazoni Extraterrestri, Italy)

Contents

List of Figures

List of Tables

Chapter 1

Introduction

1.1 Purpose

The CAM Handbook is one in a series of five[1] documents that explain the operations of the Infrared Space Observatory (ISO) and its four instruments, the data received from the instruments and the processing carried out on the data. Volume I gives an overview of the entire ISO mission and it explains the operations of the ISO satellite while the remaining four explain the individual instruments (CAM, LWS, PHT and SWS). The CAM document is intended to provide all information necessary to understand the offered ISOCAM standard data products, as processed by Version 10 of the Off-Line Processing (OLP) system, retrievable from the legacy ISO Data Archive (IDA) at:

`http://www.iso.vilspa.esa.es/`

Besides OLP 10 software processing steps and product specific details, background information is provided about the ISOCAM instrument itself, its observational modes and all aspects of calibration.

Although it tries to contain as completely as possible ISOCAM related information, it should be stressed that this manual is not intended to support interactive data analysis. For specific algorithms to process and improve the results interactively we refer to the *ISOCAM Interactive Analysis User's Manual*, [28] and to the ISO's web page for the ISOCAM instrument:

`http://www.iso.vilspa.esa.es/` → `ISO Explanatory Library` → `CAM`.

This volume of the ISO Handbook serves as the reference for both the processing as well as the correct interpretation of ISOCAM data as available from the ISO Data Archive.

1.2 Structure

In this document we present information on:

- the ISOCAM instrument and its observing modes,
- the processing steps carried out on the raw data,
- the calibration of the instrument,
- the uncertainties in the data,
- the final ISOCAM archive products.

[1] Originally six documents were planned with Volume I on the *ISO Mission* and II on the *ISO Satellite* but both have now been merged in Volume I in Version 2.0.

An overview of the ISOCAM instrument is given in Chapter 2. In Chapter 3 the modes in which ISOCAM could observe are presented. The in-orbit performance is described in Chapter 4 together with estimates of the uncertainties expected in ISOCAM data. A summary of the various ISOCAM data products available in the ISO Data Archive is given in Chapter 5. The results of the individual calibration measurements are archived in calibration libraries, which are described in Chapter 6. An overview of the Off-Line Processing (OLP) pipeline for ISOCAM data is given in Chapter 7. The main caveats applicable to the automatic data processing system (OLP) are described in Chapter 8. Finally, a short description on how to get started with ISOCAM data is presented in Chapter 9.

Several appendices are attached to give more detailed information on individual subjects.

1.3 How to Contact Us

A broad collection of information about ISOCAM and its interactive analysis system is available on our instrument web page:

`http://www.iso.vilspa.esa.es/` → `ISO Explanatory Library` → `CAM`.

In addition you may contact us by sending an e-mail to the ISO helpdesk at:

`helpdesk@iso.vilspa.esa.es`

1.4 ISOCAM Publications

1.4.1 Acknowledgements and guidelines

Any paper published based on **ISO data** should contain the following text, as a footnote to the title.

Based on observations with ISO, an ESA project with instruments funded by ESA Member States (especially the PI countries: France, Germany, the Netherlands and the United Kingdom) and with the participation of ISAS and NASA.

Should the journal in question not permit footnotes to the title, the above text should appear as a footnote the first time ISO is mentioned.

The preferred reference for the ISO mission is:

The Infrared Space Observatory (ISO) mission, Kessler, M.F. et al. 1996, A&A 315, L27

Any paper published based on **ISOCAM data** should acknowledge the instrument with the following reference:

ISOCAM in flight, Cesarsky, C.J. et al. 1996, A&A 315, L32

If you used the **ISOCAM Interactive Analysis** (CIA) to reduce your ISOCAM data please write in the acknowledgments:

The ISOCAM data presented in this paper were analysed using 'CIA', a joint development by the ESA Astrophysics Division and the ISOCAM Consortium. The ISOCAM Consortium is led by the ISOCAM PI, C. Cesarsky.

The preferred reference to CIA is:

Design and Implementation of CIA, the ISOCAM Interactive Analysis System, Ott S. et al. 1997, in ASP Conf. Ser. Vol. 125, Astronomical Data Analysis Software and Systems (ADASS) VI, eds. G. Hunt & H.E. Payne (San Francisco: ASP), 34

1.4.2 Inventory of publications

In order to offer a complete bibliographic information to the ISO Data Archive users, we try to keep track of all publications involving ISO data, and of all observations used for these publications. As a result, in IDA next to any selected observation, the button 'Articles' provides the references of the publications involving this particular observation and a link to their Astrophysics Data System (ADS) entry[2]. Your contribution in this matter can greatly help keeping an information as comprehensive as possible and we therefore ask you to kindly provide the following information for each of your publications:
- complete reference of the paper
- list of TDT numbers and instrument modes of the observations that you have exploited for the publication.

You can send the information either by e-mail to:
helpdesk@iso.vilspa.esa.es
or by normal mail to:
ISO Project Scientist
(ISO Preprints)
ESA Satellite Tracking Station
Villafranca del Castillo
P.O. Box 50727
28080 Madrid

[2]`http://adswww.harvard.edu/`

Chapter 2

Instrument Description

2.1 Introduction

The ISOCAM instrument on board the Infrared Space Observatory ISO was designed to map selected areas of the sky in the spectral region from 2.5 to 18 μm at various spatial and spectral resolutions.

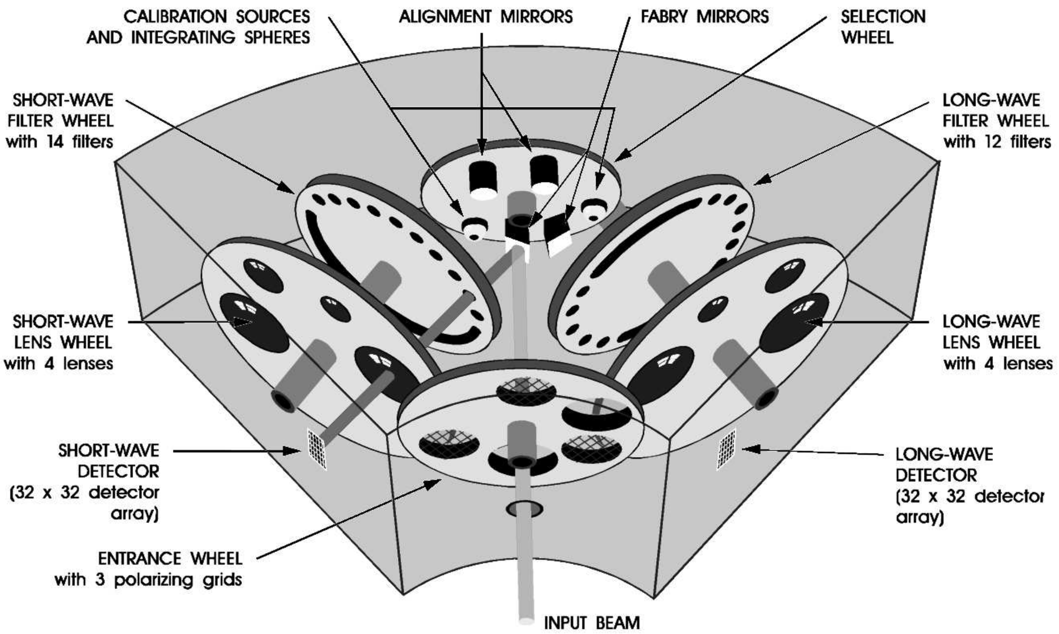

Figure 2.1: *The layout of ISOCAM.*

With ISOCAM, spectral features at wavelengths inaccessible from the ground were studied. The morphology of objects at a scale of a few arcseconds was investigated through broad and narrow band filters. Spectral imaging was also possible with Circular Variable Filters (CVF) at a spectral resolution of up to $\Delta\lambda/\lambda = 40$.

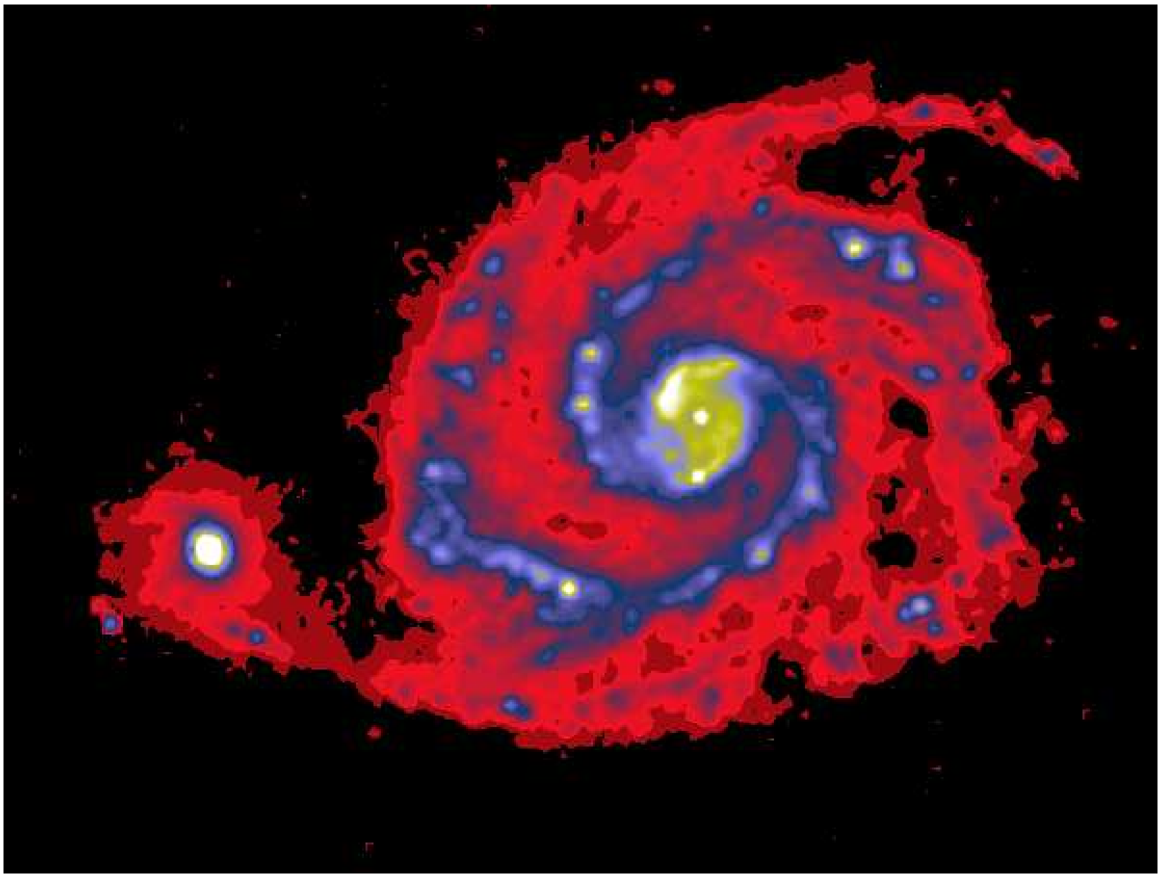

Figure 2.2: *One of the first ISOCAM raster observations was pointed at the M51 galaxy. The image is the sum of two LW3 (14.3 μm) filter raster measurements (Sauvage et al. 1996, [51])*

The spatial resolution was determined by the diffraction limit at longer wavelengths, and was limited mainly by undersampling of the PSF at shorter wavelengths. For a 60 cm diameter telescope the diameter in arcseconds of the Airy disc (FWHM) is given by $\lambda/D = \lambda$ [μm]/3, or $2.4 \cdot \lambda/D = 0.8 \cdot \lambda$ [μm] for the first dark ring. Regarding the optical performance of ISO, images of point sources were made, clearly showing up to the fifth Airy diffraction ring. A detailed description of the telescope and the pointing system is given in the ISO Handbook Volume I, [40].

ISOCAM provided imaging capabilities across a field of view of up to $3'$ diameter. It consisted of two optical channels, used one at a time, each of which containing a 32×32 pixels infrared detector array. The short wavelength channel (SW) operated between 2.5 and 5.2 μm; the long wavelength channel (LW) between 4 and 18 μm. Each channel included lenses covering a range of magnifications (yielding fields of view having 1.5, 3, 6 and $12''$ per pixel), fixed filters and CVFs. During the ISO pre-flight thermal vacuum tests it was discovered that the apparent output voltage of one of the LW detector columns ('column 24') was always at zero Volts. In space it was found that, because of the repositioning jitter in the camera wheels, the edges of the array (essentially the outermost columns), did not always receive sufficient light when using the $6''$ per pixel lens.

2.2 Optical Design

2.2.1 General description

The optical design of the camera (Figure 2.1) was based on an imaging lens focussing the sky image provided by the ISO telescope onto the detector. At the focal plane of the ISO telescope, a field mirror (called 'Fabry mirror' in Figure 2.1) imaged the telescope exit pupil onto the camera pupil. The filters and the CVF were located at the camera pupil position. An aperture stop was placed inside the filter mounts. For the CVF, an aperture stop was located before the precise pupil location. The field mirror was also used as a field stop.

Radiation from the sky entered the camera via a pyramidal mirror and first encountered an entrance wheel offering the alternatives of a clear aperture or a set of three polarising grids with position angles 120 degrees apart; the zero orientation was defined as the spacecraft y- axis (for a description of the spacecraft axes, see the ISO Handbook Volume I, [40]). The selection between the two channels of the camera, SW and LW, was achieved by opting to use one of four tilted field mirrors mounted on the selection wheel. These field mirrors were placed in the focal plane of the telescope, and depending upon which of them was in position, the telescope beam was fed into one of the two channels.

Each channel included a filter wheel, with bandpass filters and Circular Variable Filters (CVFs). The SW channel contained 13 filters (including two redundant ones), and a CVF for the 2.273 to 5.122 μm range. The LW channel contained 10 filters, and 2 CVF's covering the 4.956 to 17.34 μm ranges. The spectral resolution was about 40 for the CVF's and ranged from 2 to 30 for the bandpass filters.

In each channel a lens, mounted on a wheel, re-imaged the focal plane of the telescope onto the array. Four different lenses on the wheel provided four different magnification factors matching the fixed physical pixel size to the desired pixel field of view (pfov hereafter) on the sky. The pfov for the different lenses were: 1.5, 3, 6 or 12$''$ (see Table 2.1).

Each of the field mirrors, described earlier, yielded an image of the telescope pupil. This image was located between the field mirror and the lens, in the plane of the filter wheel. Each filter carried a diaphragm, actually a hole punched through a sheet of metal, which acted as an aperture stop. For the CVF, of course, such a stop could not be implemented at this location (i.e. precisely at the filter location). Instead, a stop was placed 6 mm ahead of the plane of the pupil image, slightly oversized because of the beam aperture. The fixed filters were tilted with respect to the optical axis, to avoid ghosting due to back-reflected light. For mechanical reasons, the CVF had its plane normal to the axis. This, together with the poorer aperture stop, produced more straylight for the CVF than for the fixed filters (see Section 4.9).

The field mirror acted as a field stop for the light coming from the telescope. For each channel, there were actually two possible field mirrors providing two different fields of view: 198×198 arcsec^2, and 87×87 arcsec^2.

With the 1.5$''$ and 3$''$ pfov, only the central part of the 3$'$ diameter unvignetted field of view provided by the telescope beam was used by ISOCAM; the field of view of the camera was then limited by the size of the detector array.

In the 6$''$ pfov, there was some vignetting in the corners of the 3×3 arcmin^2 square field of view covered by the array, since the system was designed to match the 3$'$ diameter unvignetted field of view of the telescope. The vignetting can be up to 20% in extreme cases because of the wheel repositioning jitter (see Section 2.2.2).

With the 12$''$ pfov, the field stop was always the field mirror, and the outer part of the detector array was not illuminated.

The Point Spread Function (PSF) is a convolution of the diffraction figure of the 60 cm telescope with the sky sampling of the pfov. The PSF (see Section 4.6) was undersampled with the 12$''$ and the 6$''$ pfov; it covered about 2 pixels for the 3$''$ pfov, and it was better sampled with the 1.5$''$ pfov. The PSF was

Table 2.1: *Efective field of view for different combinations of pfov and lenses*

pfov	Field mirror	Effective field of view
$1.5''$	small	$45'' \times 45''$
$3''$	small	$87'' \times 87''$
$3''$	large	$1.5' \times 1.5'$
$6''$	large	$3' \times 3'$
$12''$	large	$3.3' \times 3.3'$

uniform over the circular $3'$ field of view, but was somewhat degraded in the corners of the square $3'$ field of view.

Due to the tilted field mirror, there was a small field distortion. For the $6''$ pfov, an object which would have given an image of 32 pixels on the top of the array gave an image of only about 31 pixels at the bottom of the array (see Section 4.10).

Since it was not possible to have a broad-band anti-reflection coating on the detector, light was reflected back from the detector. This reflection was a source of straylight. To avoid strong ghosts the fixed filters were tilted with respect to the optical axis. Nevertheless, secondary reflections on the wheels, and on the filter mounts caused residual ghost images (see Section 4.9). The worst case arose for the $3''$ pfov where light coming from the whole $3'$ field of view fell on the golden connecting strips at the edges of the photosensitive part of the detectors. To reduce this effect in the specific case of the $3''$ pfov, the optional small field mirror was provided to define a field better matched to the array size in this optical configuration. This field mirror was undersized to take into account positioning tolerances. Only 29×29 pixels were illuminated with this small field mirror and the $3''$ pfov lens. When the CVF was used in combination with the $3''$ pfov, the use of the small field mirror was mandatory. The most frequently applied optical configurations, as recommended by the instrument team and selected by the observers, were:

Small field mirror:

- $1.5''$ pfov with filters or CVF.
- $3''$ pfov with the CVF.
- $3''$ pfov with filters and very high background,
  or in the presence of a bright source in the $3'$ field of view.

Large field mirror:

- $3''$ pfov and normal background.
- $6''$ pfov.
- $12''$ pfov.

2.2.2 The edge columns

There was a certain amount of play in ISOCAM's wheels. This caused the field mirror to occasionally shift the field of view away from column 0 or 31, the edge-columns of the detector array. Column 0 was more often affected than column 31. The vignetting can be seen in LW measurements when the background is strong. The shift of the field of view also occured in the SW channel, as evidenced in the trend analysis of the CAM daily calibration measurements (Gallais & Boulade 1998, [35]).

2.2.3 Polariser displacement

Sources observed through the three polarisers were displaced by several pixels on the detector array as compared to the source position obtained through the entrance hole. The displacement was strongly dependent upon the polariser in place. Taking the source position obtained through the entrance hole as the nominal (zero) position and measuring the relative displacement (x, y) of the source centre for each polariser, the results given in Table 2.2 were obtained. For polarisation observations using the observing mode designed for extended sources, the displacements of the different polarisers were compensated for by offsetting the spacecraft pointing (Section 3.4) in opposition to the numbers given in Table 2.2. As a consequence of this approach it was possible to take, as a first order approximation, the polariser images directly obtained, and to calculate the Stokes vector without applying further registration techniques.

Table 2.2: *Polariser displacements.*

Polariser	$x \pm \Delta x$ [$''$]	$y \pm \Delta y$ [$''$]
P1	-3.4 ± 0.1	-11.2 ± 0.3
P2	-8.9 ± 0.1	$+0.6 \pm 0.3$
P3	-3.0 ± 0.1	-4.7 ± 0.3

2.3 The SW Array

For the short wavelength channel, the detector array was an InSb 32 × 32 pixels Charge Injection Device (CID), manufactured by the Société Anonyme des Télécommunications. At the time of the ESA Call for 'Proposals for ISO instruments', it was already qualified and offered the advantages of a low operating temperature and a large radiation tolerance, compatible with the ISO mission, including the 89% filling factor of the $100 \times 100\,\mu m^2$ pixels and the charge injection efficiency. The effective quantum efficiency was 0.3 at $4\,\mu$m, with a flat curve towards shorter wavelengths, and a cut-off at $5.2\,\mu$m.

Hybrid electronics for control and readout were designed to work at 4 K, close to the chip. The array and its cold electronics were housed behind a titanium cover which provided a shield against cosmic ray particles and straylight.

2.3.1 Readout and integration time (SW)

The readout of the SW array was an elaborated form of CID readout. Measurement of the pixel charges was done by sensing the voltages of the 32 output lines after sequentially injecting the pixel charges into the substrate through column voltage gates. The analogue chain used an adaptive filter followed by a high gain preamplifier. The filtering scheme gave a periodic signal with 32 peaks corresponding to the pixel intensities. The baseline was measured before and after each injection, giving 65 measurements. The true value of the pixel charge was provided by the difference between the peak measurement and the mean value between the 2 adjacent baseline measurements. This scheme held for the 32 photosensitive lines, and also for 2 blind reference lines used for removing the correlated pick-up noise. The data were stored in a 34×33 frame for the baseline measurements, and a 34×32 frame for the peak measurements. The allowed integration times were: 0.28 s, 2 s, 6 s, 20 s and 60 s.

The array was little affected by charge particle induced glitches, therefore long integration times were practical. Long on-chip integration times reduced the impact of the high readout noise of this device.

There were three possible readout modes:

- normal: the exposures were transmitted to the ground station at the specified integration time.
- sampled: only every n'th exposure was transmitted to the ground station
- accumulated: n exposures were co-added on board and only the co-added image was transmitted to the ground station

When the integration time was 0.28 seconds, four images were averaged on board before downlink as the telemetry rate only allowed to send one image every second.

2.3.2 Noise (SW)

The noise on the SW channel had several origins: detector noise, amplifier noise, electrical cross-talk and pick-up noise.

The output signal was very small, a few mV, and the lines were very easily affected by pick-up noise. To reduce the impact of this noise source, the signals from the 2 blind lines (see Section 2.3.1) went through the electronic chain as if they were pixel lines. They were used as a reference for the correlated pick-up noise. A correlation matrix between the pixels on the reference lines and the actual pixels was used to remove the correlated noise.

Cross-talk between pixels arose in the connecting wires between the array and the cold electronics. Since odd and even lines had geometrically separated outputs, the cross-talk had a strong parity characteristic. Echoes of a bright source on line n were found on lines $n-2$ and $n+2$, but not on lines $n-1$ and $n+1$. A cross-talk matrix was used in the data processing (see Section 5.5.1) to remove this effect.

After removal of the correlated noise and of the electrical cross-talk, the remaining noise can be very well modelled by a constant readout noise and the photon shot noise. The readout noise was about 700 e^-/pixel rms.

2.3.3 Linearity and saturation (SW)

The SW array, like every CID, was non-linear. Deviation from linearity reached 20% at 2/3 of the dynamic range. The device saturated at 10^6 e^-/pixel.

2.3.4 Gain and encoding (SW)

The Analogue to Digital Converter (ADC), and the programmable offset and gain controls were shared by the SW and the LW channels. For the SW channel, the offset was automatically set and the gain was 2. This setting of the gain was recommended, to provide a good sampling of the noise, while preserving the whole dynamic range of the array. In these conditions, one Analogue to Digital Unit (ADU) corresponded to 360 e^-, the pixel saturated at 3000 ADU, and the noise was 2 ADU rms.

2.3.5 Dead pixels (SW)

Four pixels remained throughout the mission at a high readout signal and did not provide any useful information. The positions of these pixels are given in the CCGSWDEAD calibration file (see Section 6.1.1).

2.4 The LW Array

At the time of the ESA Call for 'Proposals for ISO instruments', there was no array available in Europe suitable for usage in the long wavelength channel of ISOCAM. A specific development programme was

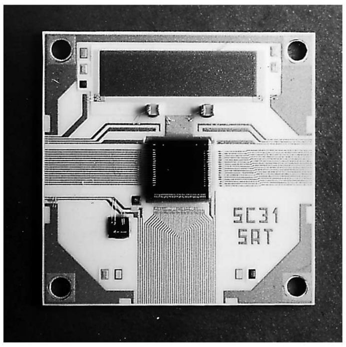

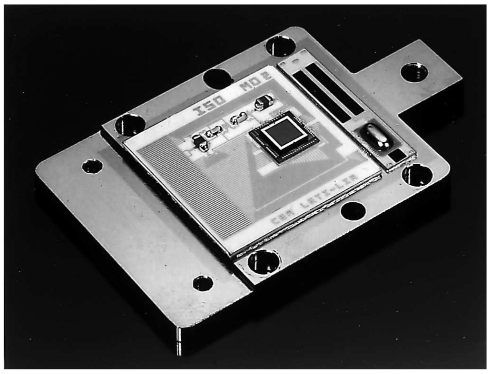

Figure 2.3: *ISOCAM detectors.*

undertaken at the Laboratoire d'imagerie Infrarouge (CEA/LETI) in Grenoble. It led to a 32×32 gallium doped silicon photoconductor array hybridized by indium bumps to a direct voltage readout circuit. The pixel pitch was $100\,\mu$m and the detectors were $500\,\mu$m thick. A 25 V bias voltage was applied to the photoconductor, providing the optimum trade-off between responsivity and the overhead required to allow for stabilisation of detector response. With this bias voltage, the responsivity at $15\,\mu$m was 10^{14} V/W, corresponding to a photoconductive-gain $\times$ quantum efficiency product of $\eta \cdot G \approx 1$. To a first approximation, at shorter wavelengths, the responsivity decreased with λ, and there was a long wavelength cut-off at $18\,\mu$m.

To obtain a 100% filling factor, the front surface was doped to ensure a good electrical surface conductivity and the bias voltage was applied to an aluminum frame on the side of the optically sensitive area. An external guard, 3 pixels wide, was added around the 32×32 sensitive pixel frame to prevent field line distortion in the detectors at the edges. The cross-talk was very low, and remained below 1.5%, even for the $12''$ pfov which had the fastest lens of the camera (numerical aperture $\approx$ f/1).

2.4.1 Readout and integration time (LW)

For each pixel, the readout circuit had an integration capacitance of 0.12 pF and a MOSFET follower stage with a gain of 0.8. A double-sampling readout scheme was used, first resetting the output capacitance and measuring this reset level, then integrating and measuring the level at the end of the integration. The reset level and end of integration level were stored and transmitted to the ground in two separate 32×32 frames. The integration times allowed were: 0.28 s, 2 s, 5 s, 10 s, or 20 s.

As for the SW detector there were three different readout modes:

- normal: the exposures were transmitted to the ground station at the specified integration time.
- sampled: only every n'th exposure was transmitted to the ground station

- accumulated: n exposures were co-added on board and only the co-added image was transmitted to the ground station

When the on-chip integration time was 0.28 seconds, four images were averaged on board before being downlinked as the telemetry rate only supported downlinking of one image every second. Only for special calibration measurements was the sampled mode used with 0.28 seconds integration time, in order to get a higher time resolution than in the accumulated mode. Long on-chip integrations were limited by the rate of occurence of cosmic ray induced glitches. The glitch rate was such that the use of the available 20 second on-chip integration time was discouraged during the mission.

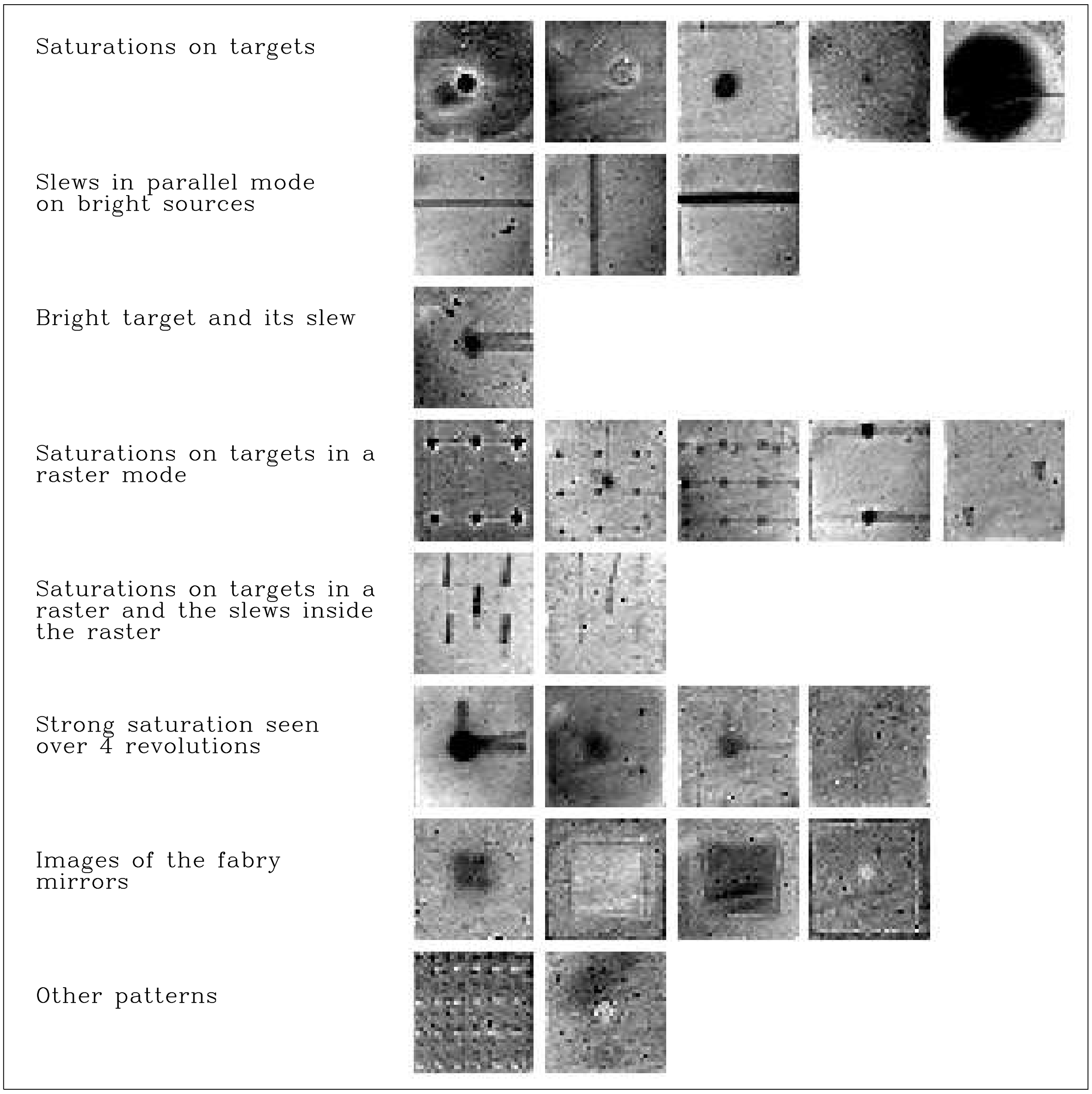

Figure 2.4: *Gallery of LW saturation remnants (from Boulade & Gallais 2000, [14])*

2.4.2 Noise (LW)

The noise of the array in the LW channel consisted of several components: a high frequency term which is well approximated by a constant readout noise of ≈180 e^-/pixel rms added to the photon shot noise, and a low frequency term which becomes important only after several tens of readouts (depending on the flux intensity and the integration time). At high level, $> 10^6$ e^-/pixel, an amplifier noise becomes dominant and limits the signal-to-noise ratio to ≤ 500 in a single exposure. The optimum performance was obtained with a signal between 2×10^4 and 1×10^5 e^-/pixel.

2.4.3 Linearity and saturation (LW)

For a given on-chip integration time, the output signal was linear with the incoming flux and saturated above 6×10^5 e^-/pixels. In-flight observations on standard stars showed that the responsivity for different integration times was always the same with an accuracy better than 1% (see Section 4.1.3).

The main effect of a saturation was a decrease of the responsivity in that part of the array which had been overilluminated. This effect was manifested in science observations as an undesirable remnant of any bright source, appearing as a hole compared to the level of the neighbouring background. If no curing of the detector was performed after a saturation event, as was usually the case during ISO operations because of the time constraints, the remnant was observed for a long time after the triggering event. It could take hours or even days for the affected pixels to recover their nominal responsivity. As the effect of the decrease of the responsivity could be observed when the detector was 'homogeneously' illuminated, flat-field measurements, such as those performed during the de-activation sequence, were well suited in identifying any serious event which could have occurred inside the revolution and which could have left a trace on the detector. Figure 2.4 gives an example of a gallery of patterns seen in the ICD measurements. The origin of the pattern is indicated in each case.

2.4.4 Gain and encoding (LW)

The on-board readout electronics had 32 independent channels, one for each column of the array. It was based on DC amplifiers followed by sample and hold circuitry. An analogue multiplexer was used to read each line and to encode the signal on 4096 levels. A programmable offset was applied before the analogue to digital converter, and the gain of the chain could be selected from among the 3 factors: 1, 2 or 4, to allow for a good sampling of the noise in low flux conditions, and to take advantage of the whole dynamic range. For general user applications the offset was automatically set, and the observer had to choose the gain; in typical conditions, a gain of 2 was selected, providing 120 e^-/ADU and a good sampling of the 1.5 ADU rms of the readout noise over the whole linear range of the array. With this gain, the dynamic range of the system was limited by the analogue to digital converter to $\approx 5\times10^5$ e^-/pixel. In case of a higher signal, a gain of 1 could be selected. Gain 4 was deprecated as it easily led to saturations of the detector, even upon the occurence of moderate glitches.

2.4.5 The missing column (LW)

Column 24 of the LW detector was disconnected. The detector was still active but there was no data available. As the orientation of column 24 on the sky (which varied as a function of satellite revolution) was known only after the observations were scheduled, it was recommended for cases where data was needed across the whole array, to execute raster observations with redundant sky coverage (using a maximum raster-step size of 23 times the pfov in the y-direction). Column 24 ran in the satellite z-direction and was offset from the center of the array in the satellite y-direction (see the ISO Handbook Volume I, [40]).

2.5 Filters

Information on the SW and LW filters is given in Tables 2.3 and 2.4. The reference wavelengths were chosen to clearly identify the different filters. Generally they are easy to remember wavelengths, and in most cases they are close to the isophotal wavelength for either a λF_λ = constant spectrum or the energy distribution of Sirius (Moneti et al. 1997, [42]). These definitions have also been applied to the ISOPHOT filter system. The transmission curves are given in Appendix A. The spectral transmission curve for each filter is the filter transmission convolved with the detector quantum efficiency. The method for colour correction of observed flux densities is explained in Appendix A. The flux calibration of the filter measurements is described in Section 4.1.1.

Table 2.3: *SW filter characteristics. λ_{ref} is the reference wavelength (Moneti et al. 1997, [42]), while λ_c is the central wavelength of the transmission curve. The range of wavelengths between the half-maximum transmission points, the approximate spectral resolution and the main scientific purpose are also indicated.*

Ident.	λ_{ref} [μm]	λ_c [μm]	$\Delta\lambda$ [μm]	λ / $\delta\lambda$	Scientific purpose
SW1	3.6	3.57	3.05–4.10	3	Cosmological filter, close to L' Common to ISOPHOT
SW2	3.3	3.30	3.2–3.4	17	PAH (3.28 μm)
SW3	4.5	4.50	4.0–5.0	5	General purpose, common to LW
SW4	2.8	2.77	2.50–3.05	5.5	General purpose
SW5	4.0	4.25	3.0–5.5	2	High sensitivity
SW6	3.7	3.72	3.45–4.00	7	Optimum L, comparison for SW7
SW7	3.0	3.05	2.9–3.2	10	Ice band
SW8	4.05	4.06	4.00–4.15	33	Br α
SW9	3.9	3.88	3.76–4.00	20	Comparison for SW8
SW10	4.6	4.70	4.53–4.88	13	CO fundamental
SW11	4.26	4.26	4.16–4.37	20	CO_2

Table 2.4: *LW filter characteristics. λ_{ref} is the reference wavelength (Moneti et al. 1997, [42]), while λ_c is the central wavelength of the transmission curve. The range of wavelengths between the half-maximum transmission points, the approximate spectral resolution and the main scientific purpose are also indicated.*

Ident.	λ_{ref} [μm]	λ_c [μm]	$\Delta\lambda$ [μm]	λ / $\delta\lambda$	Scientific purpose
LW1	4.5	4.50	4.0–5.0	5	General purpose, common to SW
LW2	6.7	6.75	5.0–8.5	2	General purpose
LW3	14.3	15.0	12.0–18.0	3	High sensitivity
LW4	6.0	6.0	5.5–6.5	6	UIR feature
LW5	6.8	6.75	6.5–7.0	14	General purpose, comparison for LW4
LW6	7.7	7.75	7.0–8.5	5	UIR feature, comparison for LW7
LW7	9.6	9.62	8.5–10.7	4	Silicate band
LW8	11.3	11.4	10.7–12.0	9	UIR feature, comparison for LW7
LW9	14.9	15.0	14.0–16.0	8	General purpose, CO_2
LW10	12.0	10.5	8.0–15.0	2	IRAS Band 1, common to ISOPHOT

2.6 Circular Variable Filters (CVF)

The CVF is a multi-layer thin film interference filter mounted on the filter wheel. Its substrate is a sector of a ring. The thickness of each layer of thin film is a function of the polar angle on the sector. An elementary area of the ring behaves as a narrow bandpass filter. Both its central wavelength and its bandpass are functions of the polar angle on the sector, and thus of the position of the filter wheel. The flux and wavelength calibration are described in Sections 4.8 and 4.8.1. The first and last two steps of each sector suffer significant vignetting.

Table 2.5: *Wavelength range and spectral resolution of the different CVF segments.*

CVF segment	$\lambda_{begin} \rightarrow \lambda_{end}$ [μm]	$\Delta\lambda$ [μm/step]	FWHM [μm]	$\lambda/\delta\lambda$
CVF SW	$2.273 \rightarrow 5.122$	$0.0252 \rightarrow 0.0252$	$0.0954 \rightarrow 0.125$	41
CVF1 LW	$4.956 \rightarrow 9.583$	$0.062 \rightarrow 0.0483$	$0.134 \rightarrow 0.220$	$37 \rightarrow 43$
CVF2 LW	$8.782 \rightarrow 17.34$	$0.110 \rightarrow 0.090$	$0.258 \rightarrow 0.336$	$34 \rightarrow 52$

2.7 The Internal Calibration Device (ICD)

The internal calibration device was designed to provide a reproducible, but not absolute, calibration reference. Calibration of the SW channel required source temperatures up to 350 K which are difficult to fit in the low thermal dissipation budget of ISO. To achieve the required emission, a small resistor was mounted on a thin Kapton film. The low thermal conductivity of the Kapton film prevented heat losses towards the ISOCAM base plate and ensured that almost all the energy would be radiated. This emitter fed, through a small input hole, an integrating sphere mounted on the selection wheel. In the calibration mode, the output hole of the integrating sphere took the place of the field mirror. The brightness uniformity was better than 1% over the unvignetted circular $3'$ field of view of ISO. Two spheres were included in the system, one for each channel, with entrance holes adapted to the flux required for each array. The temperature of the emitter could vary in the range 150 K to 350 K.

This design had two limitations. From the point of view of the optical design, the beam aperture of the ICD was defined only by the aperture stop at the filter location. It was therefore different from the ISO telescope f/15 beam. Nevertheless, SW flat-fields were obtained using the ICD (see Section 4.5). The second limitation was due to the presence of some low level emission bands from the Kapton film support which was heated by conduction. They can be seen at long wavelengths in the spectrum of the calibration device. This precluded the usage of this system as an absolute flux calibration reference. However, it was used for flat-fielding the SW array and for trend analysis (see Section 3.7.3). The ICD was also used to 'flash' the detectors after leaving the Van Allen radiation belts or after a saturation event. A large current pulse was sent to the IR emitters at the beginning of a calibration sequence to speed up the heating of the emitter before setting the current to its required stable value. To avoid saturation of the detectors during this heating period, the filter wheel was set on a blind (dark) position. Therefore, it was not possible to make a calibration of the arrays without going for a short time to a dark position.

2.8 Wheel Step Number and Optical Components

Most ISOCAM data products report wheel positions by their angular displacement with respect to some fixed and arbitrary zero position; the angular displacement is measured in step numbers [1]. The calibration

[1] A step number is in fact the count of gear teeth from the zero position

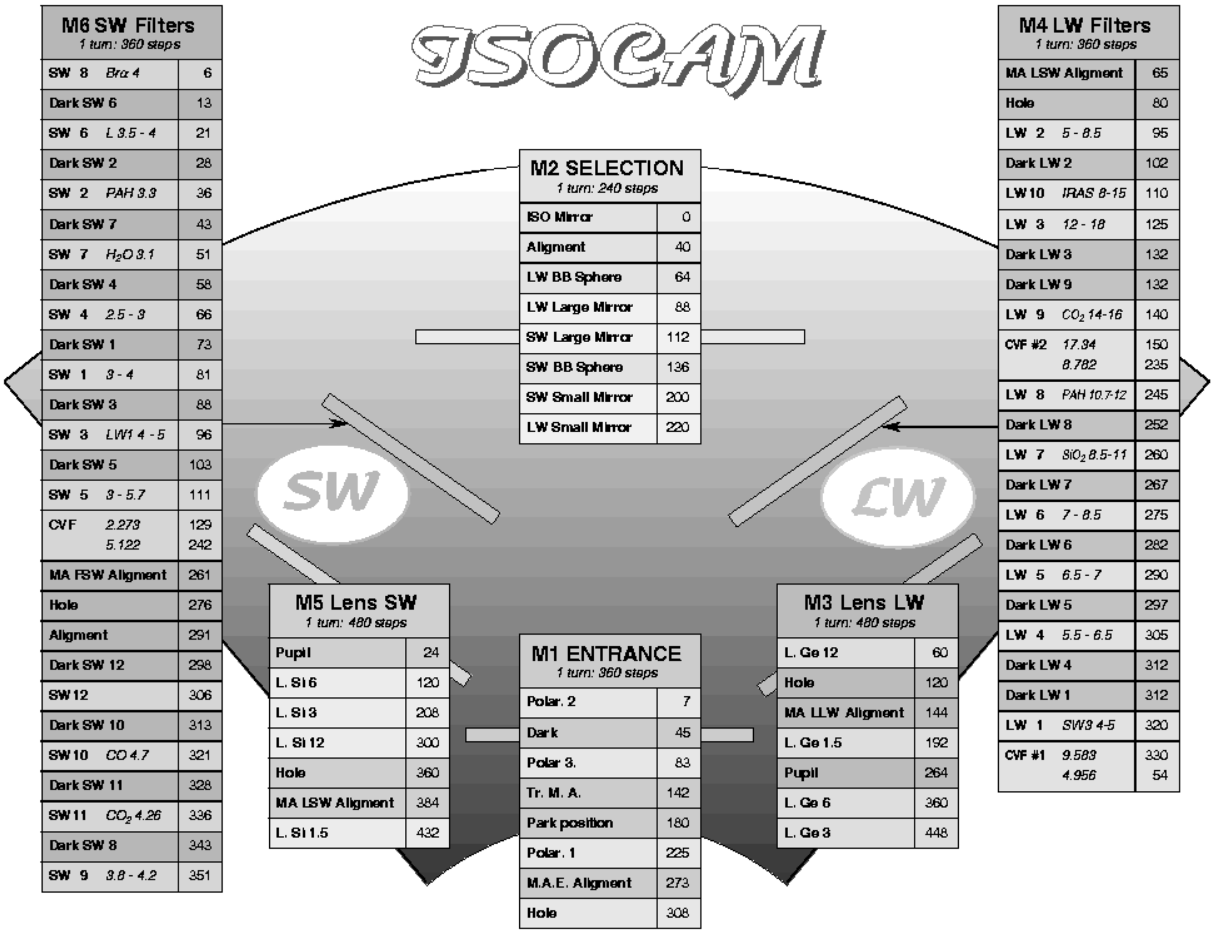

Figure 2.5: *The correspondence between wheel step numbers and optical components.*

file CWHEELS gives the more descriptive names used among observers for the optical element in the path (such as 'Hole', 'LW10', etc) for each wheel position (Section 6.1.14). The correspondance between wheel step numbers and optical components is shown in Figure 2.5.

Chapter 3

Instrument Modes and Astronomical Observation Templates

ISOCAM had three main imaging modes: photometric, spectrophotometric and polarimetric. Measurement strategies included single pointing (i.e. staring) observations, celestial rasters and beam-switch measurements.

The observing modes were configurable via three dedicated Astronomical Observation Templates (AOT):

- CAM01 – General Observation, including single pointing, raster and micro-scanning
- CAM03 – Beam-switch
- CAM04 – Spectrophotometry

In the following sections the different observing modes will be discussed in more detail. Because of the special requirements of the *polarimetric* observations, the very flexible Calibration Up-link System (CUS) was used for their implementation, rather than implementing them through an AOT. Other operations which were performed outside the AOTs were many calibration measurements (using the CUS), occasional tests of other observing modes, the activation and de-activation of the instrument and engineering and calibration observations performed during handover between VILSPA (Villafranca, Spain) and Goldstone ground stations (see the ISO Handbook Volume I, [40]).

3.1 Photometric Imaging (CAM01 and CAM03)

CAM01 (general observation mode) was dedicated to photometric imaging. It was possible to select either of the wavelength channels (LW or SW), various pfov's and one or more of the broad and narrow band fixed filters, as well as sets of discrete CVF positions. It was a very flexible AOT which allowed up to 64 such observing configurations within a single Target Deticated Time (TDT). CAM01 supported staring observations as well as celestial raster maps having a raster step-size between $2''$ and $180''$. With the raster, one could not only cover areas larger than the field of view of the camera, but could also improve the flat-field accuracy using micro-scanning techniques. Rastering was recommended for the detection of weak, confused or extended sources, as well as in the presence of a structured background. During a raster measurement the instrument configuration remained unchanged. Rasters could be repeated with different settings up to the 64 configurations mentioned above. The orientation of the raster scan was either aligned with the spacecraft axes (i.e. parallel to the edges of the detector array) or with reference to the sky N-direction (see the ISO Handbook Volume I, [40]).

CAM03 (beam-switch) was also dedicated to photometry and allowed the subtraction of one or more nearby reference fields. It also supported the use of different channels, pfov's and filters. The method was recommended for the detection of weak isolated sources, when there was not too much structured background or for observing compact, high-contrast sources, which would suffer from smearing in a raster. Several off-target reference fields were allowed, although this option was rarely used. There was an option to repeat the cycle of on-off measurements.

The default order for performance of beam-switch observations involved first observing the target and then the background position(s). In practice this implementation proved to be ill advised, because a bright source, if observed in the first pointing of the observation, would leave a remnant on the detector which would be carried through the subsequent background measurements, contaminating them and leading to an eventual photometric error when the merged background measurements were subtracted from the on-target measurement (see Section 4.4). Therefore observers often measured the background position first, followed by the on-source position. To do this they had to 'mislead' the mission-planning software and give the background position for the on-source position and vice versa. This had the temporary disadvantage of confusing earlier versions of the Off-Line Pipeline Processing (OLP) software, which consequently produced inverted maps, a problem solved, however, in the Legacy ISO Data Archive.

3.2 Spectrophotometric Imaging (CAM04)

CAM04 (spectrophotometry) was designed for stepwise imaging across the wavelength ranges of spectral features, such as dust bands, complex molecules, or gas emission lines, as well as for spectral imaging scans across virtually the full wavelength range covered by the camera. A spectrum was obtained by following a given sky pixel or region through a series of narrow-band images. A complete CVF spectrum took at most 115 steps in the short wavelength channel and 85 for each of the CVFs which together spanned the long wavelength (LW) channel.

The basic observing parameters were the same as for CAM01 though the wavelength range of the spectral scan and the CVF increment that detemined the wavelength step had also to be specified. The command logic then determined the initial ('begin') and final ('end') positions of the filter wheel closest to the requested wavelength range limits, and scanned between these positions at 'step number' intervals. A scan was always done with the same overall optical configuration of the instrument. However, within the same TDT it was always possible to perform several scans in different overall instrument configurations (channel, pfov, wavelength range, step number interval).

The spectrophotometric (CVF-scanning) mode could not be used with beam-switch or in a celestial raster map although individual CVF positions could be used in the modes CAM01 and CAM03 described above.

3.3 Stabilisation Exposures

Because of the importance of the stabilisation of the signal (see Section 4.4), measurements were often begun with a number of so-called stabilisation exposures, with the camera on-target and in the selected configuration, and allowed to adjust to the new input flux level. We note that the stabilisation exposures are retrieved, together with the science exposures, from the ISO Data Archive and are useful for data analysis purposes. In a raster measurement, stabilisation readouts were only done at the first raster position.

It was also possible to programme, within the AOT, certain calibration measurements of one's own, for example a dark measurement or a measurement of the internal calibration device (ICD). This was, however, strongly discouraged after launch as it would have disrupted the stabilisation of the signal. The general facility calibration was sufficient to calibrate the scientific measurements.

3.4 Polarimetric Imaging

Because the polarimetric imaging was more complex, it was performed with the Calibration Uplink System (CUS) and not through an AOT. Observations using this mode could be performed using one filter wheel position (broadband filter or CVF position), selected by the user, per application of the mode. Only CAM LW was supported. The target was observed through three separate polarisers. The polarisers had orientations with respect to the spacecraft axis of 0°, 120° and 240°. The angle is defined such that the +y-axis has orientation 0° and angles are measured toward the +z-axis direction (see the ISO Handbook Volume I, [40]).

ISOCAM polarisation observations start with a raster measurement without polariser on the free entrance hole. The observer could then choose:

1. to rotate the polarisers on each successive raster position, or
2. to perform the raster in one polariser followed by a rotation of the entrance/polariser wheel to the next polariser position at which another raster was performed, and so forth.

In both observing procedures, the rasters were repeated in several observing cycles. The second observing mode was in particular recommended for extended targets. The nominal spacecraft pointing was offset to compensate for the known source displacement on the detector which occured while cycling the polarisers (see Section 2.2.3). A detailed description of the performance and capabilities of polarisation measurements with ISOCAM is given in Siebenmorgen 1999, [55]. In the ISO Data Archive (IDA), the polarisation data can be found catalogued under one of the modes: CAM05 (only for point sources) or CAM99 (for point and extended sources).

3.5 'Coronography'

A limited number of observations were performed in a test mode referred to as 'coronographic' mode. In the coronographic mode the 3″ lens was used in combination with the small Fabry mirror on the CAM entrance wheel (Section 2.2.1). In this configuration the field stop (the Fabry mirror) projected a field image smaller than the detector array, so that the outer parts of the detector array were unilluminated by the sky. Light from a source positioned so that its image fell just off the edge of the Fabry mirror was discarded, so that the configuration worked similarly to a coronograph. The object to be blocked was moved just outside the edge of the field stop to map the surrounding emission. There were only a few observations done this way and they need interactive analysis to be studied.

3.6 Parallel Mode

ISOCAM was in its so-called 'parallel' mode (Siebenmorgen et al. 1996, [54]; 2000, [56]) while observations were performed with other ISO instruments and during satellite slews. In this mode the sky was observed between 12′ and 17′ away from the prime target observed by another instrument. The allowed configurations during parallel mode were as follows: LW2 (6.7 μm), 6″ pfov and gain 2; LW4 (6.0 μm), 6″ pfov and gain 2; LW3 (14.3 μm), 1.5″ pfov and gain 1; CVF position at 15 μm, 1.5″ pfov and gain 1, or dark position. These different configurations corresponded to different levels of sensitivity and were chosen as a function of the risk of saturation of the camera during any given prime-instrument TDT. For example, in the LW2, 6″ parallel mode configuration, a star brighter than about 0.5 Jy in the IRAS 12 micron band would saturate the detector.

After the observing timeline for an ISO revolution was planned, the offset positions where ISOCAM would observe in parallel mode were checked for saturation by the CAM Instrument Dedicated Team (CIDT), using the IRAS database. If a danger of saturation existed, a change of configuration was scheduled for manual uplink during the revolution.

As ISOCAM was also measuring during slews which could not be screened in advance for saturations, it was also decided to use specific parallel mode configurations for different regions of sky. For observations further than 10° from the galactic plane, the default parallel mode configuration (hardwired in the uplink system) was the one that used the LW2 filter. For observations within 10° of the galactic plane, the default parallel mode configuration (also hardwired) was the one that used the LW4 filter. For restricted locations, other parallel configurations were either observer selected or manually imposed by the instrument team before target acquisition, or before observation termination (see below). For $|b| < 1°$ and $|l| < 60°$ the LW3 option was used. This configuration was also used in the revolutions on which systematic calibration measurements were performed. For observations within 1 degree from the Galactic Centre, where the risk of saturation was even higher, the CVF 15 μm mode was used. If none of these modes would prevent a saturation, the camera was put in a dark position.

When an ISOCAM observation was scheduled, the instrument arrived on the source in one of the relatively sensitive default parallel mode configurations and it was put back in parallel mode at the end of the AOT, before leaving the source. Therefore there was a risk that the ISOCAM detector would be saturated in the parallel mode configuration even if the source was perfectly safe in the requested configuration for observing. In order to allow observations of relatively bright sources to coexist with the parallel mode, the observer could control the instrument set-up before and after the actual observation. This was done by adding to the beginning and to the end of an observation or concatenated chain of observations, dummy observations on safe off-target positions, where the desired observing configuration could be obtained.

3.7 Special Measurements

While only a small number of science observations did not use standard AOT modes (e.g. polarisation and coronographic observations), a large number of calibration and engineering test measurements were performed using the Calibration Uplink System (CUS), or other specialised commanding systems.

In IDA the special measurements are found under 'non-standard' data (CAM99) and 'engineering' data (CAM60, CAM61, CAM62 and CAM63). No science data were taken in these measurements.

3.7.1 CAM60

After leaving the Van Allen radiation belts (see the ISO Handbook Volume I, [40]), the CAM instrument was activated and put in standby.

3.7.2 CAM61

Next step in the activation sequence of CAM, was flashing the detectors (both LW and SW) with the Internal Calibration Devices (ICDs).

3.7.3 CAM62

Before entering the radiation belts, the instrument was switched off. In the so-called 'de-activation' sequence, a set of calibration measurements was performed which were used to monitor the camera's behaviour during the mission. The sequence consisted of LW dark measurements of 2 seconds on-chip integration time, LW dark measurements of 5 seconds on-chip integration time (only until revolution 125), SW dark measurements of 2 and 6 seconds (from revolution 270) and ICD illumination of the detectors through the LW2, LW3, SW1 and SW3 filters (the so-called 'internal flat-fields'; see Gallais & Boulade 1998, [35]).

3.7.4 CAM63

During the handover of the satellite control from the VILSPA station to the station in Goldstone, another set of CAM calibration measurements was performed. These started only after revolution 150 and included LW dark measurements of 5 and 2 seconds on-chip integration time. The dark current measurements obtained this way were used to model the dark current trends throughout the mission (see Section 4.2.2; Gallais & Boulade 1998, [35]; Biviano et al. 1998a, [5]; 2000, [9]). Later in the mission the sequence of measurements was modified. The 2 and 5 seconds integration darks were measured on revolutions with odd numbers. A new set of measurements of 0.28 and 10 secs were performed on the even numbered revolutions. This alternating sequence started at revolution 764.

The results of the trend analysis based on the CAM62 and CAM63 measurements is described in Gallais & Boulade 1998, [35].

3.7.5 CAM99

CAM99 data were obtained from so-called CUS (Calibration Uplink System) observations which were used in general for calibration measurements. Specific scientific observations like the coronographic mode or polarisation measurements needed special commanding and so also used the CUS that allowed more freedom and flexibility than the more conservative AOTs.

Chapter 4

Calibration and Performance

In this chapter an overview is given of different aspects of the instrument performance during the mission. The approach to the instrument calibration is explained. Important topics addressed are the conversion of the measured signal into flux density, the dark current correction, flat-fielding of the camera and the determination of the Point Spread Function (PSF). Other aspects which are important in the interpretation of the ISOCAM data are discussed like, for instance, the drifts or 'transient' behaviour of the detector signal, the effects of cosmic ray impacts, and in relation to the optics: the wheel positioning jitter, ghost reflections and straylight, and some degree of field of view or 'pincushion' distortion. At the end of the chapter a global error budget is given.

4.1 Responsivity

4.1.1 Absolute flux calibration

The absolute flux calibration of the ISOCAM instrument is based on observations of standard stars, which are believed to be the most reliable calibration sources in the 2–18 μm ISOCAM wavelength range. Before and during the ISO operations, Spectral Energy Distributions (SEDs) were provided by Martin Cohen (Cohen et al. 1992, [18]; 1995, [19] and 1996, [20]) and through an extensive pre-launch 'Ground Based Preparatory Programme' (GBPP), led by Prof. Harm Habing (Jourdain de Muizon & Habing 1992, [39]; van der Bliek et al. 1992, [61]; Hammersley et al. 1998, [36] and Hammersley & Jourdain de Muizon 2001, [37]). Later, additional SEDs were provided by Dr. Leen Decin who, through an iterative process using SWS data, produced a set of MARCS model synthetic spectra (Decin 2001, [25]; Decin et al. 2003a, [26]). The absolute flux calibration of the various models delivered is estimated to be better than 3%. A discussion on a comparison of the different provided models can be found in Decin 2001, [25].

The determination of the CVF Spectral Response Function (SRF) is discussed in Section 4.8. The fixed filters calibration relied mainly on the model spectra from the GBPP. In the GBPP, Kurucz models were fitted to the visible and near-infrared data to provide flux densities at longer wavelengths. Mostly, early- or intermediate-type stars were selected (A, F, G) and not late-type giants which can show strong molecular absorption band features which are not well addressed in the Kurucz models (Blommaert 1998, [10]). A wide range of stars with different flux densities was used (ranging from 10 mJy up to 10 Jy). In order to be able to revisit the stars regularly, they were selected from a region of sky with an almost 100% visibility to ISO (R.A. $\approx$ 16 hrs, DEC $\approx$ +55). Because of the high sensitivity of ISOCAM and the resulting higher risk for saturation, generally weaker and thus somewhat less well studied standard stars were observed. For cross-calibration with other (ISO) instruments some of the brighter calibration stars were observed in the few filters which did not saturate the camera for such bright sources.

The flux calibration observations were done in staring mode with the source at the centre of the array. Data analysis of the standard star measurements was performed within the CIA package and followed a standard procedure, including: deglitching (method='temp'), averaging the frames on the stabilised part of the measurement, flat-field correction and background subtraction. A more detailed description of the observations and the selection of the standard stars used for the calibration of the fixed filters can be found in Blommaert 1998, [10] and Blommaert et al. 2000, [11]; 2001b, [13].

The conversion from measured signal in ADU/G/s to flux density in Jy is conveyed in the so-called SENSITIV parameter which can be found in the calibration file CCG*SPEC (see Section 6.1.6). The conversion factor is given for the reference wavelength of each filter, assuming a $\lambda F_\lambda(\lambda) = constant$ spectrum. Formally the reference wavelengths are arbitrary and they have been chosen so that they clearly identify each filter and are easy to remember. Some reference wavelengths (for the filters: SW1, SW2, LW6, LW8 and LW10) are chosen for comparison with the ISOPHOT filters. The LW10 filter gives also a direct comparison with the 12 μm IRAS filter. For further details see Moneti et al. 1997, [42].

Tables 4.1 and 4.2 give the the reference wavelengths and the values of the SENSITIV parameter for the LW and SW filters, respectively. The observed spread in the SENSITIV parameter, also indicated in these tables, is caused by two factors. One is the uncertainty in the extrapolation of the near-infrared fluxes on the basis of the Kurucz models. The second is the difference in stabilisation of the signal of the various observed calibration stars. Although special care was taken to ensure that the signal had stabilised, uncertainties of the order of 5% remain.

Table 4.1: *LW SENSITIV values.*

Filter	λ_{ref} [μm]	Mean [ADU/G/s/mJy]	rms [%]
LW1	4.5	0.77	4.1
LW2	6.7	2.32	3.3
LW3	14.3	1.96	4.8
LW4	6.0	0.78	7.5
LW5	6.8	0.35	7.5
LW6	7.7	1.03	6.4
LW7	9.6	1.33	6.7
LW8	11.3	0.78	5.4
LW9	14.9	0.65	2.8
LW10	12.0	4.23	3.9

4.1.2 Trends in the responsivity

The responsivity was monitored through the mission by regularly observing the star HIC 89474 (= HR 6847) (Blommaert 1998, [10]). Filters used were LW2, LW10 and SW3. The same source was also observed throughout the spacecraft orbit, to check for possible variations as a function of the orbit phase. Figure 4.1 shows all the LW2 photometric measurements of HIC 89474 as a function of time since instrument activation, following passage of the satellite through the Van Allen belts. There is a trend of decreasing responsivity with time since activation. The difference between the response at the start of the revolution and at the end is about 6%. This value is included in the CCGLWLOSS calibration file (see Section 6.1). Figure 4.2 shows the LW2 photometry, corrected for the in-orbit trend in responsivity, and running up to revolution 801. The difference between the maximum and minimum level is less than 10% and the overall rms is 2%. There is no trend in the responsivity as a function of time through the mission, the only trend being the intra-revolution drift already described. The same conclusion holds for the LW10 measurements (and concerning the in-orbit trend, also for LW1 which was observed repeatedly on revolution 349) so that we believe that this is the general behaviour of the LW detector. SW also shows only a small variation throughout the mission (rms = 2%) and no significant trend is found.

Table 4.2: *SW SENSITIV values.*

Filter	λ_{ref} [μm]	Mean [Adu/G/s/mJy]	rms [%]
SW1	3.6	0.41	4.6
SW2	3.3	0.12	4.9
SW3	4.5	0.26	3.4
SW4	2.8	0.30	2.9
SW5	4.0	0.77	4.8
SW6	3.7	0.19	6.0
SW7	3.0	0.16	4.5
SW8	4.05	0.038	7.2
SW9	3.9	0.074	5.8
SW10	4.6	0.092	2.5
SW11	4.26	0.058	5.5

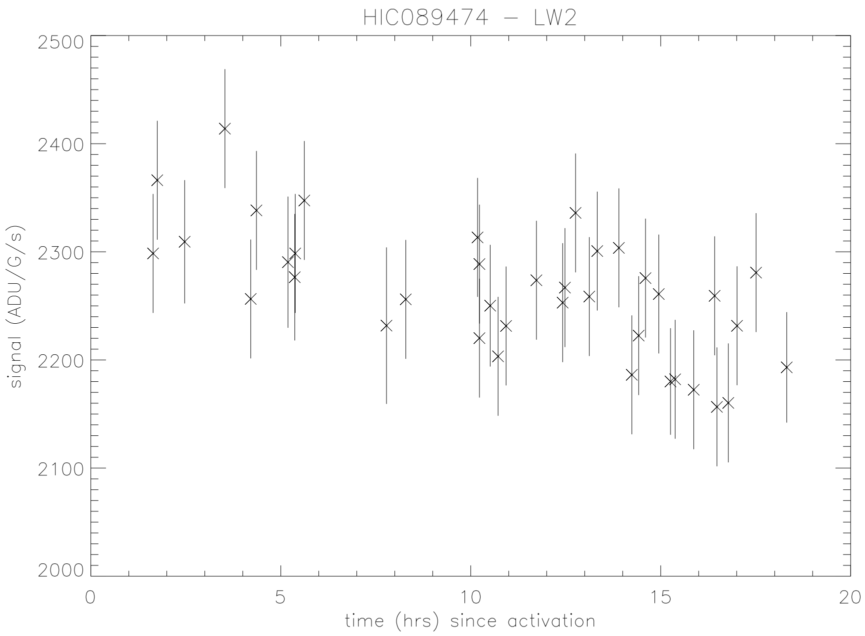

Figure 4.1: *Photometry in the LW2 filter of HIC 89474 as a function of time since activation. There is a trend of decreasing responsivity along the orbit.*

The response of the detectors was also monitored throughout the mission by measuring the ICD during each de-activation sequence at the end of a revolution. The trend analysis shows that the SW responsivity was very stable and decreased by at most 0.5% over the mission (Gallais & Boulade 1998, [35]; Boulade & Gallais 2000, [14]). The mean level of the LW 'flat-field' measurements showed a slow decrease of about 0.8% per 100 revolutions. With these measurements it is difficult to distinguish the trend of the responsivity of the detector from any trend in the ICD emissivity. Considering the fact that the measurements of standard stars did not show such a decrease it seems likely that this effect comes from a change in characteristics of the LW ICD itself.

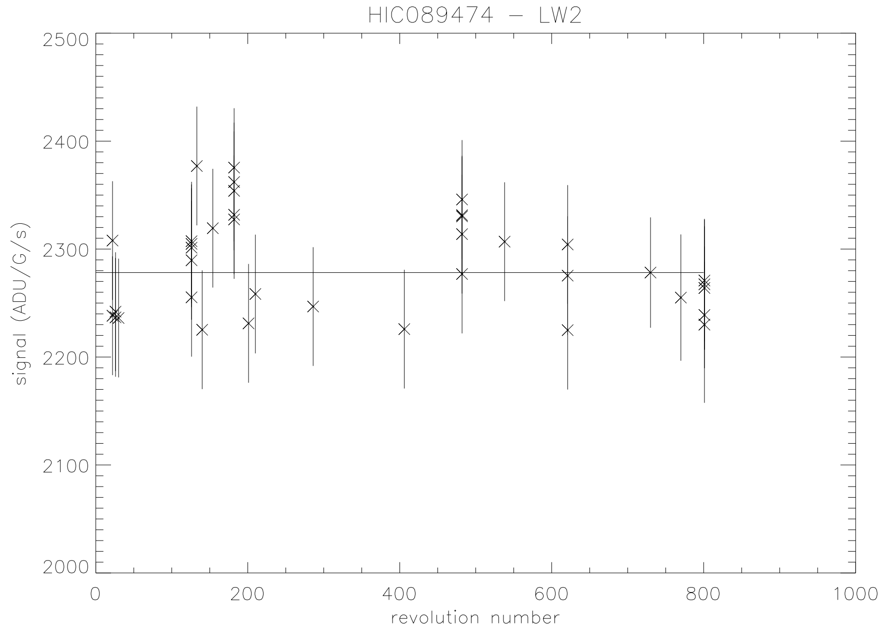

Figure 4.2: *Photometry in the LW2 filter of HIC 89474 throughout the mission as a function of revolution number. The photometry is corrected for the decrease of responsivity which occurred throughout the orbit. No significant change in responsivity through the mission is found.*

4.1.3 Responsivity and observing parameters

Observations were made to test whether any relationship could be found between the responsivity and different configurations of the camera. No, or only marginal, differences were found between different pfov's or different on-chip integration times for both detectors (Blommaert 1998, [10]; Blommaert et al. 2000, [11]).

4.2 Dark Current

With the term 'dark current' we indicate the level of the signal measured when the detector is in darkness, i.e. when no external flux reaches the detector. Strictly speaking, this is not a current, but an electronic reference level including both real dark current and electrical offsets.

4.2.1 Dark level (SW)

With the camera closed, the charge generation in the SW detectors was not due to thermal effects, but to quantum tunneling effects. It increased slowly with the logarithm of on-chip integration time. Thus very long integration times were possible without running into serious dark current accumulation problems. The dark current level and the detector noise just after launch were the same as during the ground tests, and stayed very stable for the whole duration of the mission, with the exception of a small increase in the noise (about 2.5%) after revolution 700 (Boulade & Gallais 2000, [14]). Darks obtained from calibration measurements are included in the CGSWDARK calibration file described in Section 6.1.2. The dark currents provided in the calibration file are estimated to be accurate to about 0.5 ADU/G/s (Biviano et al. 1998a, [5]).

4.2.2 Dark level (LW)

The dark level of the LW array arose as the sum of 2 effects, a leakage of charges generated during the commutation of the reset transistor, and thermal charge generation in the photoconductors. The first effect was dominant for on-chip integration times up to 10 seconds. For longer integration times, charge generation was dominant. The dark frame pattern exhibits a strong line effect with a separation between odd and even lines as can be seen in Figure 4.3.

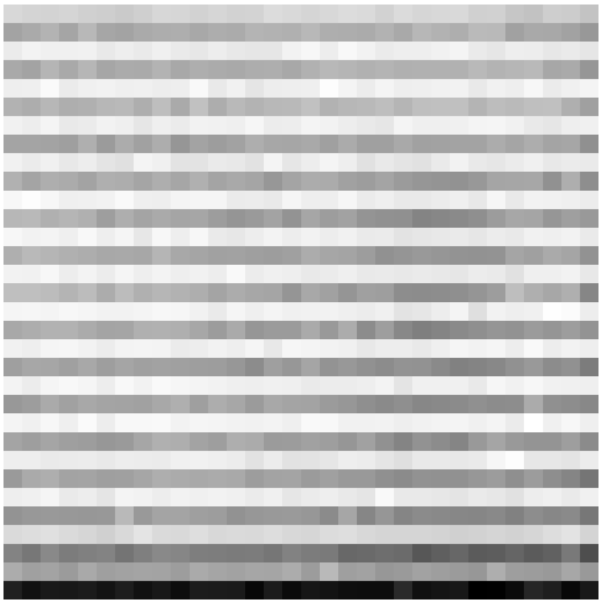

Figure 4.3: *An example of the LW dark frame, measured with 2.1 seconds on-chip integration time. Note the very evident line pattern.*

During in-orbit operations an extensive campaign was performed to study the dark current behaviour. A description of the data and the analysis performed can be found in Biviano et al. 1998a, [5]; 2000, [9] and Román & Ott 1999, [50].

Three type of significant drifts of the LW dark current were found:

- a *short term drift*, i.e. a modification of the dark current within a single revolution, from the beginning of the revolution to the end; this drift was in general non-linear, and it was different for different pixels and integration times;
- a *long term drift*, i.e. a linear decrease of dark current from a revolution to another, with a typical time scale of days; this drift was also found to be different for different pixels and integraton times;
- a correlation of the dark current with the temperature of the ISOCAM focal plane which follows a linear relation and is the same for all pixels and for all integration times.

The impact of each of these effects can be summarized as follows:

- *short term*: the drift within each revolution was $\approx \pm 0.5$ ADU from the activation to the de-activation of the instrument;

- *long term*: the drift was ≈−2ADU from the beginning to the end of the ISO mission;

- *temperature dependence*: ≈±0.25 ADU over the full range of temperature variation (few hundreths of a Kelvin).

Consequently, a model was developed that takes the different dependencies found into account and corrects the observed LW dark current per pixel as a function of the orbital position of the spacecraft and the temperature of the ISOCAM detector. The parameters of this model are provided in the CCGLWDMOD-file (Section 6.1.3). Once the corrections are applied, the median LW dark current residual amounts to ≈0.25 ADU (Biviano et al. 2000, [9]).

No similar trend was found for the SW channel.

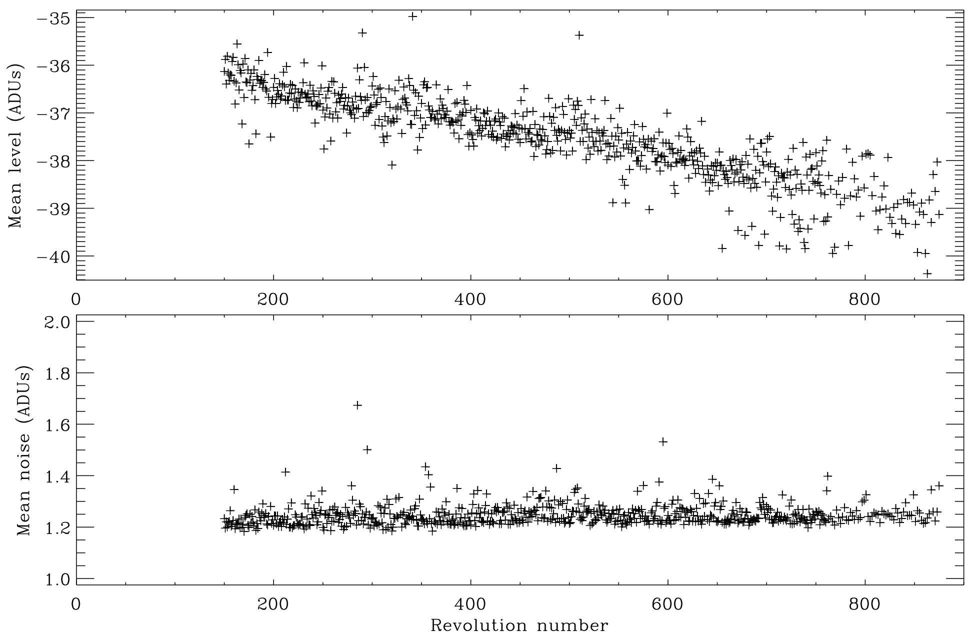

Figure 4.4: *The mean signal (top) and noise (bottom) level of the 2.1 seconds on-chip integration time handover LW dark current measurements during the ISO lifetime.*

To demonstrate the long term trend we show in Figure 4.4 the behaviour of the mean signal (top) and noise (bottom) level of the 2.1 seconds on-chip integration time handover LW dark current measurements (Section 3.7.4) through the ISO lifetime (Gallais & Boulade 1998, [35]). One immediately notes a decrease of the dark current throughout the mission. A more careful inspection demonstrates that the dark pattern on the array changed, the behaviour of odd and even lines being different.

The short term trend in the dark level, i.e. the dark current as a function of orbital position or, in effect, as a function of the time since activation of ISOCAM, is shown in Figure 4.5. Note the very similar trend in the difference between odd and even lines of the LW detector. The example is given for three revolutions with the 5 seconds on-chip integration time. For other examples see Biviano et al. 1998a, [5].

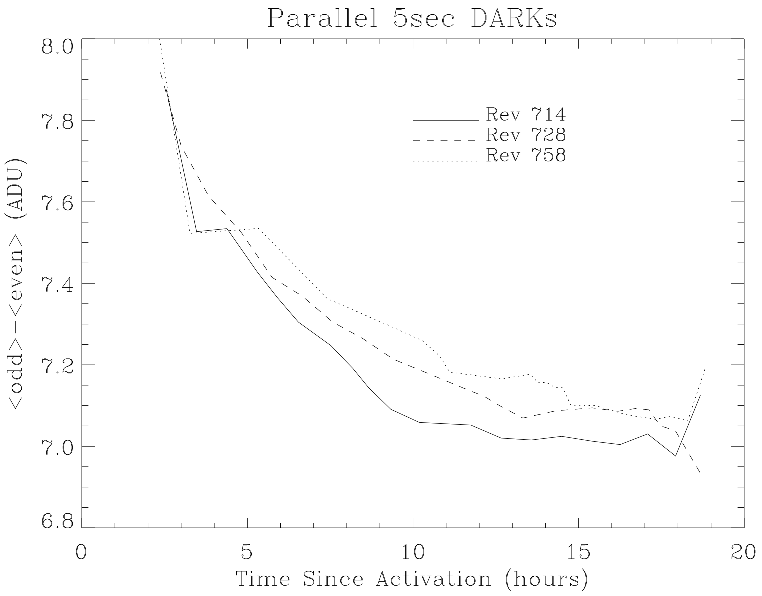

Figure 4.5: *The (median-filtered) difference of the mean dark currents of the odd and even line pixels of the LW detector. We show measurements, as a function of time since instrument activation, for 5 seconds on-chip integration time in ISOCAM parallel mode, during three ISO revolutions. No correction for the long term trend has been applied to the data so that a shift is visible from revolution to revolution.*

4.3 Glitches

Glitches are the result of an energy deposit from charged particles on the detector. This energy deposit is spatially localised on the detector and it takes a certain period of time for the detector to recover from it. These glitches were one of the main limitations in the sensitivity of the ISOCAM LW detector.

Several papers describe the nature of the detected gliches and the glitch rates (Claret & Dzitko 1998, [15]; Dzitko et al. 2000, [30]; Claret et al. 2000, [17]); and Claret & Dzitko 2001, [16]). The active zone of SW pixels is very thin (less than 10 μm) so that the SW detector has a low susceptibility to radiation effects. The LW detector, instead, has a 100 μm pitch and a much larger thickness of 500 μm leading to a much larger amount of deposited energy. Below we will discuss the main results and conclusions of the investigation of glitches affecting the LW detector.

Responsivity variations were a major challenge in maximising the sensitivity of the LW array. They could be induced by strong changes in the incident flux or by glitches. Glitch induced variations were manifested in two rather distinct problems:

1. a systematic responsivity variation after the perigee passage due to the very high radiation dose from trapped particles in the van Allen belts, and
2. (sometimes strong) responsivity variations due to the impact of individual galactic cosmic ray particles, all along the ISO orbit.

Extensive radiation tests were performed on the ground before launch using gamma-ray, proton and heavy ion accelerator beams to simulate the conditions in the van Allen belts.

High ionising radiation flux induced a responsivity increase which relaxed in a few hours. This effect was minimised if the photoconductor was under bias and exposed to a high infrared flux. Thus, in-orbit, during the perigee passage, since the experiment was switched off, a specific power supply kept the necessary bias voltage on the photoconductors, and the camera was left open to light to permit detector curing by the background infrared flux.

Outside the van Allen belts the main responsive perturbation came from galactic protons and α-particles. In addition to these external particles, the anti-reflection coating of the lenses contained radioactive thorium, which generated a dose of low energy α-particles. This flux depended on the solid angle of the lens as viewed from the array, and had a maximum for the $12''$ lens. Less frequent, but more disruptive, were incoming heavy ions. Each ion typically affected about 50 pixels, and generated a glitch followed by a decrease of responsivity.

In-orbit, the typical glitch rate and related numbers for ISOCAM detectors outside the van Allen belts were:

- Average glitch rate = 1 glitch/second
- Average number of pixels hit per glitch = 8 pixels/glitch
- The sensitivity loss was $\approx 2\%$, $\approx 5\%$ and $\approx 10\%$ for images of 2, 5 and 10 seconds on-chip integration times respectively (but the actual sensitivity loss could be higher due to glitch tails).

There was no clear variation in the glitch rate along an orbit, except just after or before the passage through the radiation belts (i.e. at the beginning or at the end of the scientific window). The glitch rate only slightly increased over the ISO operations (1995–1998). Solar activity could cause the variations observed as confirmed by the solar flare event which took place on revolution 722 in which the glitch rate became extremely high (with an increase by more than a factor of 7).

Three main families of glitches were defined by Claret & Dzitko 1998, [15]. Examples of these can be found in Figure 4.6.

- Type-A, called *common* glitches (more than 80%). These are quite easy to detect and remove from the data.
- Type-B, called *faders*; the pixel value decreases until a stabilised value is reached.
- Type-C, called *dippers*. For this type of glitches the pixel value first decreases below the stabilised value, and then increases until the stabilised value is reached.

The interpretation given in Claret & Dzitko 2001, [16] is that *common* glitches are induced by galactic protons and electrons, *faders* are induced by light galactic ions, and *dippers* are caused by particles providing higher linear energy transfer, such as heavy galactic ions.

The CAM Interactive Analysis package (see the *ISOCAM Interactive Analysis User's Manual*, [28]) contains several glitch removal methods. The different methods and their performance are discussed in Claret & Dzitko 1998, [15]. They give very good results for *common* glitches (type-A), but other type of glitches are more difficult to remove from the data. The temporal profiles of *faders* and *dippers* have some similarities with the temporal variations which are observed after a strong change of the incident flux, which also leads to a transient behaviour of the detector (Section 4.4). For example the gain variation of *dippers* (type-C glitches; see Figure 4.6) could be interpreted as an increasing signal after a flux change by a transient correction algorithm, leading to a false source detection. There is no method fully reliable and several methods should be used successively in order to get a nearly 100% glitch rejection (Ott et al. 2000, [48]), especially when the data contain strong glitches.

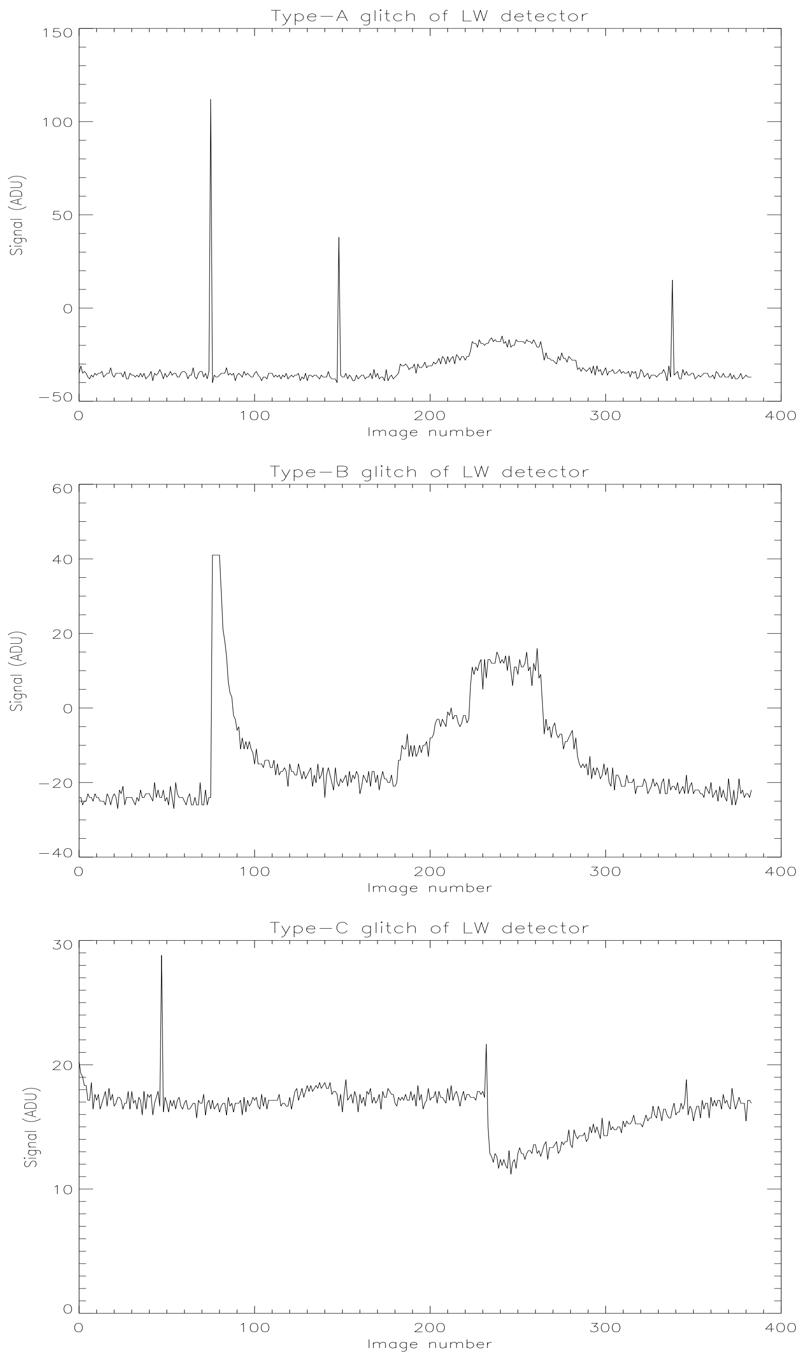

Figure 4.6: *The three main glitch families as defined in Claret & Dzitko 1998, [15]. Type-A (common) glitches have a decay time roughly as short as the rise time. For type-B (fader) glitches, the decay time is much longer than the rise time and has an exponential profile. For type-C (dipper) glitches, the detector gain is affected and the nominal sensitivity is recovered only after several readouts. Type-C glitches do not necessarily have the largest amplitudes.*

4.4 Transients

The occurrence of transients in responsivity after changes in the incident photon flux is a well known problem of extrinsic infrared photodetectors (see Fouks 1992, [31]; Coulais et al. 2000, [23] and references therein). In general, the transient response of such detectors cannot be easily described because the responses are non-linear and non-symmetrical. The transient not only strongly depends on the detector material and on the level of the incident flux, but also on the prehistory on the detector illumination and, for matrix arrays, on the signal gradient between adjacent pixels.

Both SW and LW detectors of CAM present strong responsive transient effects. Stabilisation after changes of incident flux was the main problem encountered with these arrays. After a change of incoming flux, several tens, hundreds or even thousands of readouts may be necessary to reach stabilisation at the new flux level. Because of this behaviour it was recommended for each measurement to let the signal stabilise for a number of readouts (N_{stab}), before recording the science exposures (N_{exp}). It was however, for most observations, impossible to reach a fully stabilised signal, so that methods had to be developed to correct the data for the transient behaviour. These methods will be discussed in the following subsections.

The worst cases were the following: a) switching to illumination after having the detector in the dark (the dark position of the entrance wheel); or b) after a saturating flux.

The first problem could be reduced for the LW array by keeping always light on the array (e.g. by configuring the instrument to the ISOCAM parallel mode (Section 3.6) when ISOCAM was not used in prime mode) and executing the observations in order of decreasing flux. Dark calibrations were placed at the end of the science observations, or in those revolutions with no ISOCAM science activity in prime mode. An extensive description of the responsive transients after flux steps for the two detector arrays will be described in the following subsections.

The responsive transient effect is one of the most important sources of systematic error in ISOCAM data. Therefore, it is mandatory to understand something of the nature of these transient effects and to apply transient correction methods.

4.4.1 SW transients

For SW, which accounted for only 5% of all CAM observations, a detailed physical model of the transient behaviour is lacking. Tiphène et al. 2000, [60] claim that the evolution of the responsivity with accumulated signal is likely to be related to surface traps in the semi-conductor. Those traps have to be filled first with photon-generated charges before the well begins to accumulate signal.

Starting from the observation that the lower the signal, the longer the corresponding time constant, Tiphène et al. 2000, [60] developed a model that reproduces quite well the transient behaviour, using only a small set of parameters. The model provides the asymptotic value of the stabilised signal. However, because of the limited number of test cases available it is difficult to judge whether the method is generally applicable to the full range of SW data.

4.4.2 LW transients

The transient behaviour of the LW channel has two main components: a short term drift with an amplitude of typically 40% of the total stabilised flux step, and a long term drift or transient (LTT in the following) with a typical amplitude of about 5% of the total flux step (Abergel et al. 1999, [1]). The short term response at a given time strongly depends on the illumination history of the detector, and also on the spatial structure of the sky field viewed. The LTT can affect the data for hours, but does not always occur. These effects will be described in the following subsections.

4.4.2.1 LW transients under uniform illumination

The short term transient (see Figure 4.7) of the LW channel has the following components: (1) an initial jump of about 60% of the total signal step and (2) a signal drift behaviour which depends on the flux history, on the amplitude of the current step, on the pixel position on the detector matrix and on the local spatial gradient of the illumination (Abergel et al. 1999, [1]; Coulais & Abergel 2000, [21]). Upward and downward steps are not symmetrical.

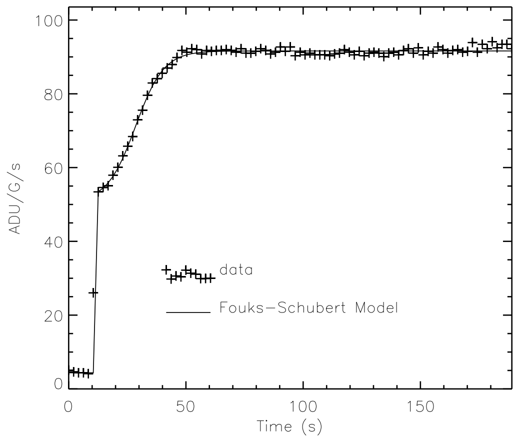

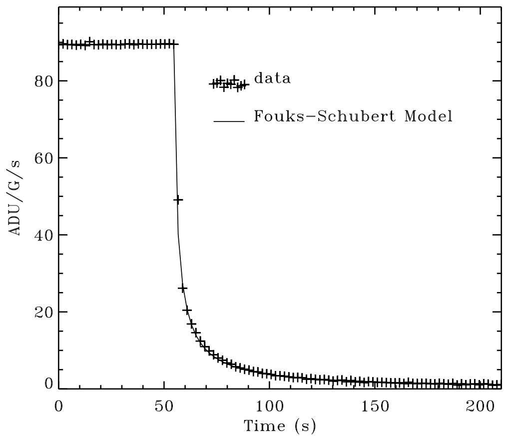

Figure 4.7: *Upward and downward steps of flux (Up : in-flight data, TDT 12900101, down : ground based test). These examples show that the transient response is clearly non-symmetrical.*

It has been shown in Coulais & Abergel 2000, [21] that under quasi-uniform illumination of the detector array the short term transient response of individual pixels can be described by an analytical model, with an accuracy of around 1% per readout (for all pixels except those near the edges of the array). This Fouks-Schubert model (FS model in the following) was initially developed for ISOPHOT Si:Ga detectors (Schubert et al. 1994, [53]; Fouks & Schubert 1995, [32]). This is not an empirical model, but a true physical model, based upon a detailed knowledge of the detector construction and properties. It is a '1-dimensional model', in the sense that: (1) the pixel surface is assumed to be uniformly illuminated; and (2) one pixel does not interact with other pixels (the cross-talk between adjacent pixels compensates each other).

The following equation describes the response for an instantaneous flux step at time $t = 0$, from the constant level J_0^∞ to the constant level J_1^∞:

$$J(t) = \beta J_1^\infty + \frac{(1-\beta) J_1^\infty J_0^\infty}{J_0^\infty + (J_1^\infty - J_0^\infty)\exp(-t/\tau)} \tag{4.1}$$

J_1^∞ is the stabilised photocurrent measured at time $t = +\infty$. It is also directly related to the observed flux, since a linear relationship is assumed between the flux and the photocurrent after stabilisation. The parameter β characterises the instantaneous jump just after the flux change. The theory gives a simple relationship between the time constant τ and J_1^∞ over several orders of magnitude: $\tau = \lambda / J_1^\infty$. Yet, the time constant is λ.

This non-linear and non-symmetrical FS model describes well the detector behaviour in response to both upward and downward flux steps, for a large range of flux changes. The description of the physics of the model, and the relevant hypotheses and simplifications are detailed in Fouks & Schubert 1995, [32] and the application to the ISOCAM LW detector is described in Coulais & Abergel 2000, [21]. Characteristic simulated outputs of the FS model are shown in Figure 4.8.

The transient effect described by the FS model is sometimes called the 'short term' transient in contrast to the long term drift (LTT). But at low input flux levels this short term transient can be very long. (e.g. CVF observations with signals exceeding the dark level by only 5 ADU/s).

The FS model is fully characterised by two parameters for each pixel: i) the amplitude of the instantaneous jump β, and ii) a constant λ in the exponential term. No significant changes of these parameters were observed during the whole lifetime of ISO, so that only one 32×32 map for each parameter is provided (CCGLWTRANS, Section 6.1.10). The FS model is used in the transient correction applied in the ISOCAM Auto Analysis (Section 7.2.5).

The application of this transient correction method to ISOCAM data (including a list of frequently asked questions about the FS model) is discussed in Coulais & Abergel 2002, [22]. Further details can be found in Coulais & Abergel 2000, [21] and Coulais et al. 2000, [23].

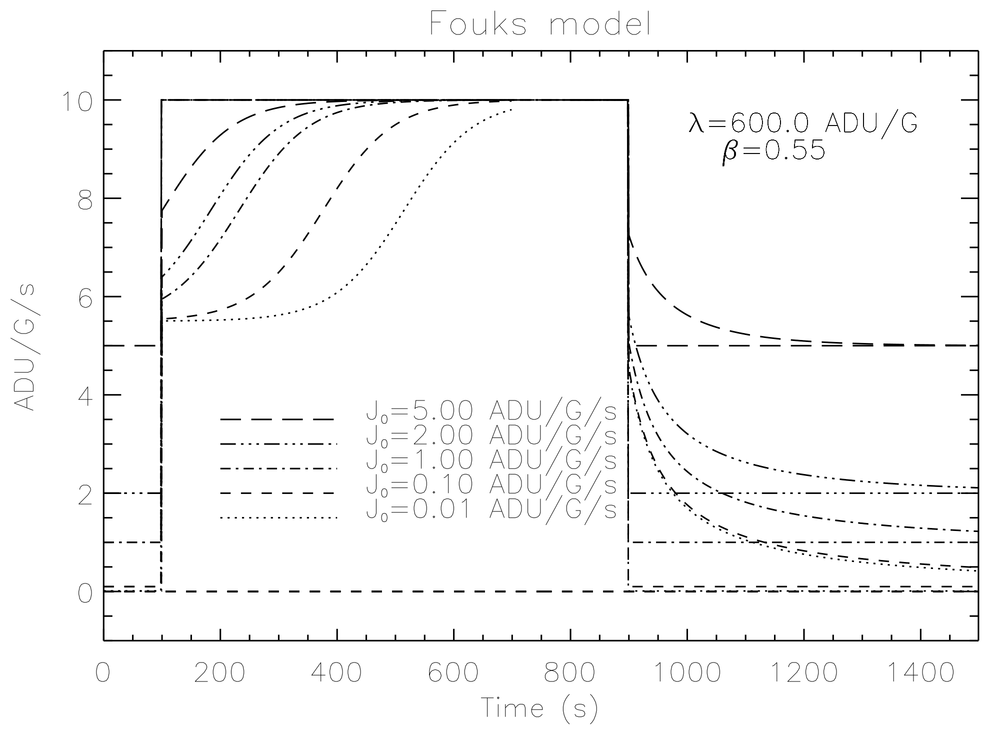

Figure 4.8: *Simulated transient responses in the Fouks-Schubert model for upward and downward flux steps. Upward steps of flux from a constant level J_0 to a constant level J_1 occur at time $t = 100$ s and downward steps from J_1 to J_0 occur at $t = 900$ s. We have taken: J_0= 0.01, 0.1, 1.0, 2.0 and 5.0 ADU/G/s, and J_1= 10 ADU/G/s. For all these simulations, the values of the parameters β and λ are constant. We see that this model is very sensitive to the initial level J_0 for the upward steps : curves from 0.01, 0.1 and 1.0 ADU/G/s are very different. When the dark level is poorly estimated, such non-linear effect can allow us to estimate the value of J_0.*

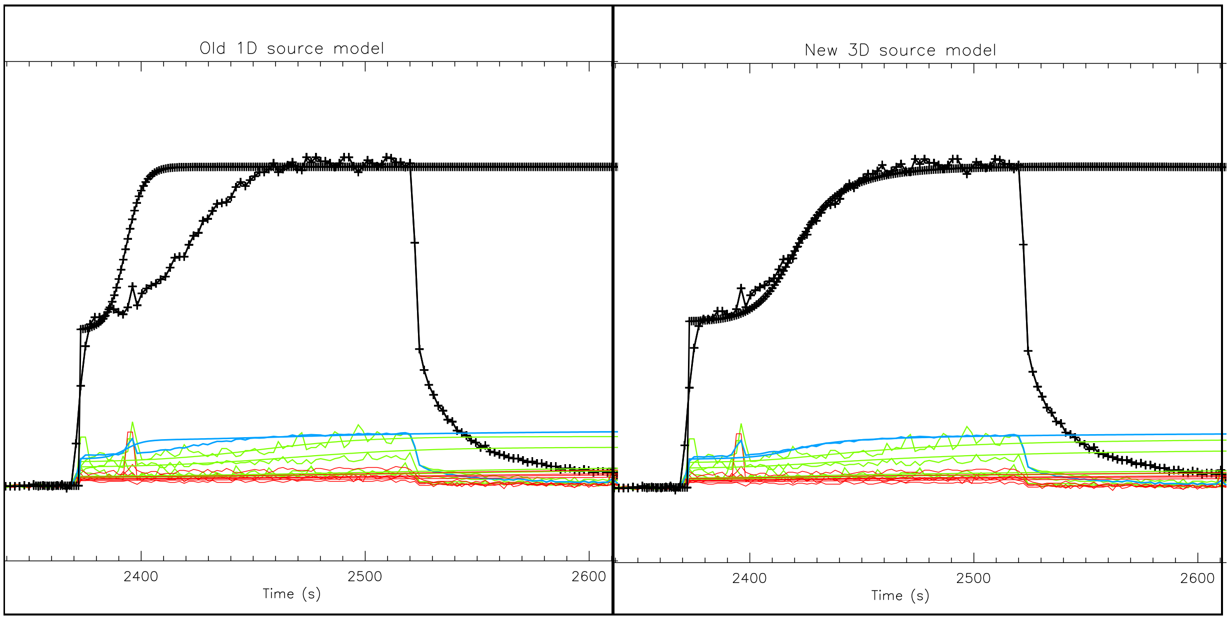

Figure 4.9: *Data taken from the TDT 35600501 (filter LW5, lens 3″). Brightest pixel: (10,15). Left panel: the data, and overplotted the 1-D Fouks-Schubert model to be used for uniform illumination case. For all the curves, the black lines are for the brigthes pixels, the blue line is the mean value of the* 3×3 *pixels, the red lines are the 4 closest pixel to the brightest, and the green lines represent the 4 diagonal pixels. Right panel: the data, and overplotted with the new model for point source transients. Since in this configuration a narrow PSF is obtained, a good agreement between the data and the new model is expected. In both cases the same* λ *and* β *values are used. The unknown parameters are* J_0 *and* J_1.

4.4.2.2 LW transients for point sources

In the LW array, the pixels are defined by the electric field applied between the upper electrode and the bottom 32×32 contacts (Vigroux et al. 1993, [63]). As a consequence of this electrical design of the array, adjacent pixels are always affected by cross-talk. Under uniform illumination, the instances of cross-talk compensate for each other. But this is not the case when the input sky exhibits strong fluctuations with angular scales around the pixel size (e.g. point sources with gradients between pixels typically higher than 20 ADU/s). The 1-D FS model, described in Section 4.4.2.1, fails for such point sources, and 3-D models are required.

A new 3-D physical model has recently been developed by Fouks & Coulais 2002, [33]. In order to test this model and compare it with the observed transient responses for CAM point sources, a simplified 2-D model, using symmetry properties of the detector array and of the point sources was derived. Under uniform illumination, this 2-D model was carefully compared with the 1-D model and both were found to give the same transients.

Without any modification, using the same (β, λ) parameters as for a uniform illumination, the new model immediately gave also the correct shape for the transients of the sharpest point sources which are very different from the transient responses predicted by the 1-D model (see Figure 4.9).

The new model works best for narrow PSFs. The model can still be improved for configurations in which the PSF is wide, for instance in the case of 1.5″ and the long wavelength filters. An example of the present status of the correction for a wide PSF, is given in Figure 4.10. The transient response of the mean value of the 3 pixels centered on the brightest pixel is accurate up to the percent-level. For the individual pixels the accuracy achieved is a few percent.

The new 3-D model is not used in the CAM OLP but is made available together with further information on request either by directly contacting Alain Coulais (currently at LERMA, Observatoire de Paris-Meudon) or through the ISO Helpdesk (`helpdesk@iso.vilspa.esa.es`).

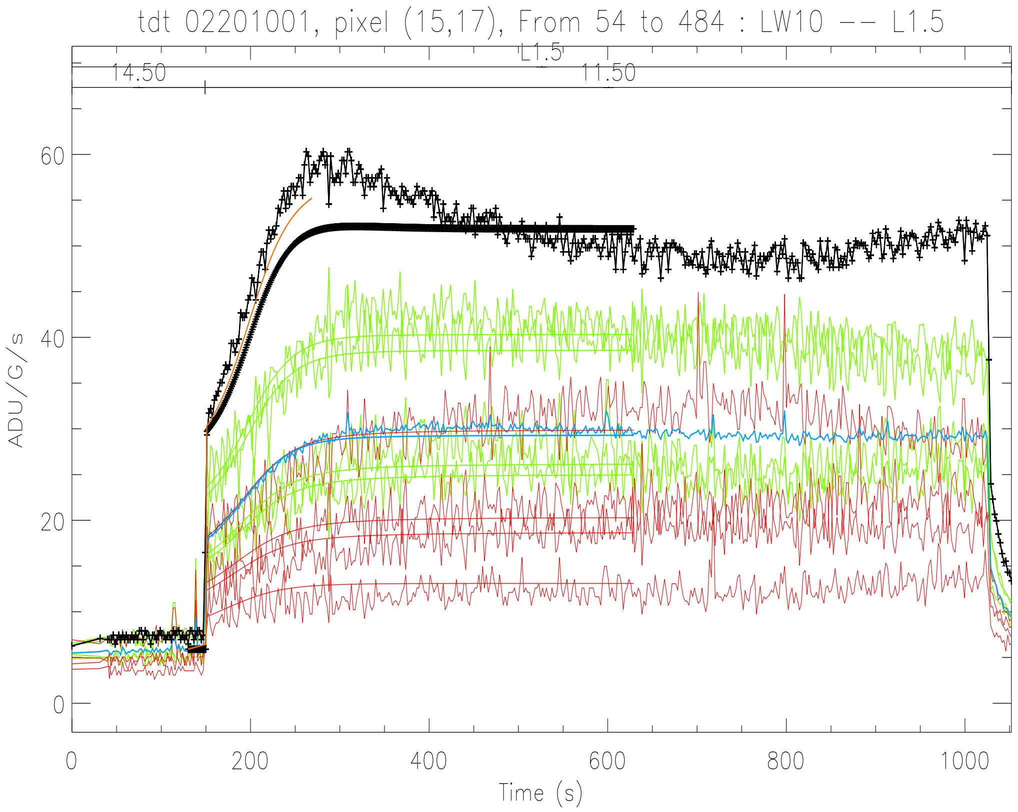

Figure 4.10: *Data taken from the TDT 02201001 (filter LW10, lens 1.5″). The different colours represent data from different pixels as explained in Figure 4.9. In this configuration, the point source has one of the largest possible FWHM of the PSF. For such a configuration the 2-D model gives a worse agreement between the data and the model on a pixel per pixel base than is found for smaller PSFs as in Figure 4.9. A better agreement is obtained for the* 3×3 *mean value. The brown curve shows a second order correction term (which may be an improvement of the method, but which has not been extensively tested yet). It should be noted that these data are difficult to process because the illumination before the observation of the source is not uniform. As usual with such non-linear models, the results are very sensitive to the initial level, and, in this case, to its profile. Here, only a mean value was used, which may produce some error for the brightest pixel.*

4.4.2.3 LW long term transients

The LW array is also affected by long term transients (LTT). After an upward flux step, a drift becomes apparent generally after the stabilisation of the short term transient, while all the instrument parameters and the input flux are constant.

This drift is characterised by a long term variation of the measured signal by a few percent (2 to 5%, see Figure 4.11). No LTT has been observed for downward steps. The LTT has never been modelled and it is not clear whether or not it may be stochastic.

From ground based data, it seems that:

1. This drift always exists for steps higher than hundreds of ADUs;
2. The lower the initial level, the higher the drift amplitude.

A similar drift effect was predicted by Vinokurov & Fouks 1991, [62]. Their physical model has been compared to several ground based data sets (Coulais et al. 2001, [24]). However, the parameters of the model have to be separately adjusted for each data set, making it unsuitable for general application. The main technical problem comes from the large uncertainty in determining the absolute dark level.

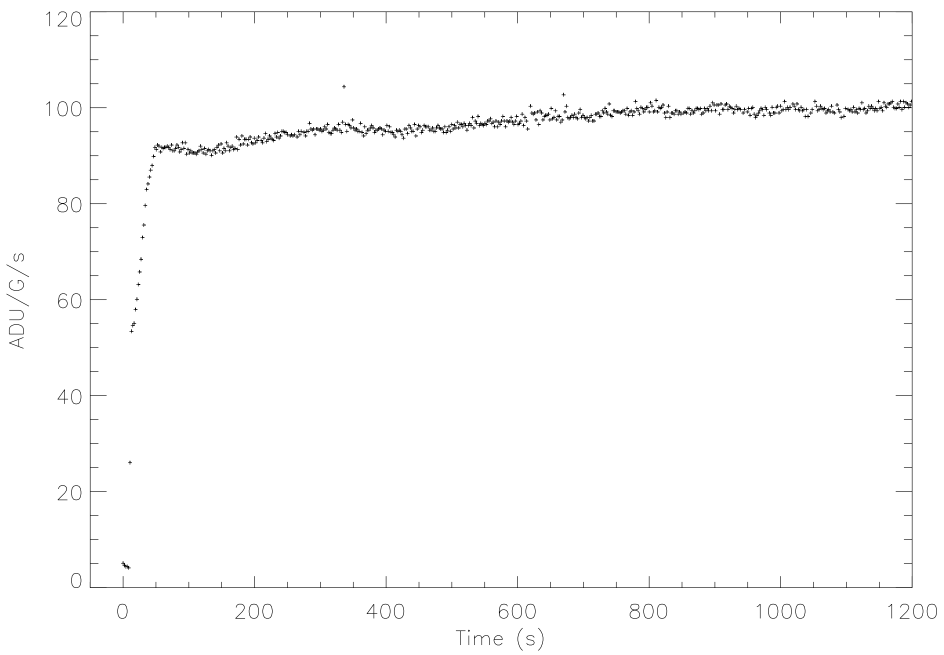

Figure 4.11: *This CAM LW in-flight observation starts just after the switch-on at the begin of a revolution. We clearly see the two components of the transient response: the short term transient from time ∼0 s to ∼50 s, which is the transient response described by the Fouks-Schubert model and, from ∼100 s to the end, the response change due to the long term drift (LTT). In this observation, the LTT amplitude is ∼7% which is especially strong for in-flight data.*

The characterisation of in-flight LTT is even more complicated, and, up to now, no reproducible effects have been found. At the present time, since physical models cannot be used to describe the data affected by LTT, empirical dedicated processing methods have been developed. Two approaches exist for the extraction of reliable information from raster observations affected by LTT. For the case of faint point sources, as in cosmological surveys, source extraction methods are discussed in Starck et al. 1999b, [59] and Désert et al. 1999, [29]. For raster maps with low contrast large-scale structure (as in the case of diffuse interstellar clouds) an LTT correction method is now available in CIA. This method was developed by Miville-Deschênes et al. 2000, [41] and is based on the use of the spatial redundancy of raster observations to estimate and to correct for the LTT (see Figure 4.12). A further description of this method can be found in Appendix F.

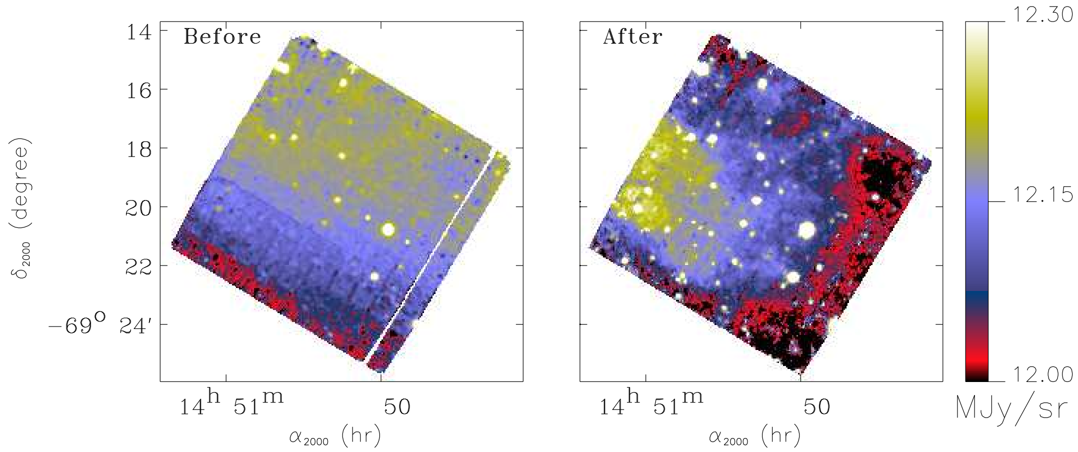

Figure 4.12: *When the contrast of the observed object is very low, and when the observations suffer from the Long Term Transient effect, it is important to use a correction method based on the spatial redundancy of raster observations. In the present case, the structure of a low contrast diffuse interstellar cloud is recovered (see Miville-Deschênes et al. 2000, [41] for more details).*

4.5 Flat-Fields

The flat-field can be defined as the relative response of different pixels of the detector to a source with uniform brightness distribution within the field of view.

For ISOCAM it is useful to distinguish between the *detector flat-field* and the *optical flat-field*.

The detector flat-field can be defined as the relative response of different pixels to a uniform illumination of the detector, while the optical flat-field can be defined as the relative flux falling onto different pixels when a source of uniform brightness distribution occupies the field of view.

The *observed flat-field* results from the product of the detector flat-field and the optical flat-field. The need to separate the two arises because the position jitter of the ISOCAM wheels (described in Section 4.11) means that the optical flat-field can move slightly over the detector.

While the detector flat-field is strictly related to the relative sensitivity of the detector pixels to incoming flux, the optical flat-field measures the vignetting due to the optical components of the camera, in particular the aperture stops near the filters. The vignetting profile is a function of the angular distance from the optical axis, and with different lens magnifications the detector sees different parts of the vignetting profile. Even with the same lens, different optical flat-fields may arise, as mentioned above, because of the wheel jitter (see Section 4.11).

In practice, the detector flat-field is not directly observable. So, by convention, the flat-field at $1.5''$ is defined to be the detector flat-field for any given filter, because it suffers less than other pfov flat-fields from vignetting effects. The optical flat-fields at any pfov are obtained by dividing the observed flat-fields by the appropriate filter detector flat-field. As a consequence, the optical flat-field at $1.5''$ is a matrix with 1's everywhere.

Flat-fielding is a crucial step in the data processing, in particular in the infrared, where the brightness of the background is very often comparable to (or higher than) the brightness of the target source. Therefore, the generation of flat-fields is a very important step in the overall calibration strategy of ISOCAM.

It must be noted, however, that many observations in raster and beam-switch mode allow the observer to directly build a flat-field from his data, depending on the brightness of the background, and the relative extension of the target source(s) with respect to the raster (or beam-switch) steps. In all staring mode observations, as well as in a few cases of raster and beam-switch observations, particularly of very extended sources or crowded fields, the use of a flat-field library is nevertheless unavoidable.

There have been two kinds of flat-field observations:

1. observations of the Zodiacal Background, which we will refer to as 'ZB flat-fields' in the following;

2. observations of the Internal Calibration Device, which we will refer to as 'ICD flat-fields'.

The targets for ZB observations were chosen as close as possible to the sun-viewing constraint of ISO in order to maximise their flux. The choice of the raster strategy for observation allows the minimisation of possible non-uniformities in the zodiacal background, since a given pixel of the detector sees different sky pixels during the raster, and a flat-field image can be constructed from the median of all raster-position images. A total of $\sim$100 ZB raster observations were executed in the available ISOCAM calibration time. In Figure 4.13 we show four examples of ZB flat-fields in the LW3 (15μm) filter, with 1.5$''$, 3$''$, 6$''$ and 12$''$ pfov, respectively.

It can be seen that only the central part of the array is illuminated when the 12$''$ pfov is chosen. The pixel dependent stabilisation times generate a pattern across the images which increases the spatial noise. Low frequency noise levels can be observed for several minutes after a flux step. The main problems are for pixels located at the edges of the array, and on a line in the lower left hand quadrant of the array which has a slightly lower responsivity than the average (and it is usually nicknamed: 'the hair'). The flat-fields have been normalised so that the mean of the central 11$\times$11 pixel sub-array is one. This definition has the advantage that vignetted outer pixels do not alter the normalisation factor, causing the flat-field to directly contribute to the photometric calibration factor for the system. (Ideally, the flat- field should only adjust spatial fluctuations, it should not affect the average signal level for the array.)

Even with a careful choice of the brightest zodiacal positions, the zodiacal background does not provide enough illumination for a proper calibration of all ISOCAM configurations. This is the case for the shorter-wavelength, small-pfov, configurations of CAM LW, and for all of the SW configurations. For LW a solution was adopted to replace the flat-field of configurations with low zodiacal background with the ZB flat-field of a corresponding configuration nearest in wavelength. The only solution for CAM SW was to use the ICD as the calibration source. This choice has the drawback that the ICD does not provide a uniform illumination of the field of view of ISOCAM, and considerable vignetting is seen at the edges of the detector. (See Section 2.7).

It is important to stress again that most raster and beam-switch ISOCAM scientific observations can provide independent flat-field estimations. The idea behind these observing modes was indeed to beat the pixel-to-pixel response variation by observing the same sky region with different pixels. Observers using these observing modes do not need to be particularly concerned about the quality of the calibration flat-fields. The calibration flat-fields are however necessary for staring observations (or when the source is very extended with respect to the raster dimensions, or the observed field is very crowded).

Imperfect flat-fielding induces two kind of error:

1. photometric error arising from the uncertainty in the responsivities of the pixels that see each source; and

2. the photometric error arising from the background subtraction.

As the source will be usually located at the centre of the array, the former error will always be relatively low, of the order of a few percent, even when no sky flat-field is available, since one can safely use the ICD flat-field near the array centre. On the other hand, identifying faint sources over a high-brightness background requires a very accurate flat-field.

As an example, the currently achieved median accuracy of 0.5% in the LW10 6$''$ flat-field means that with an average background flux of 50 ADU/G/s in this configuration, the 1-σ limit for the detection of

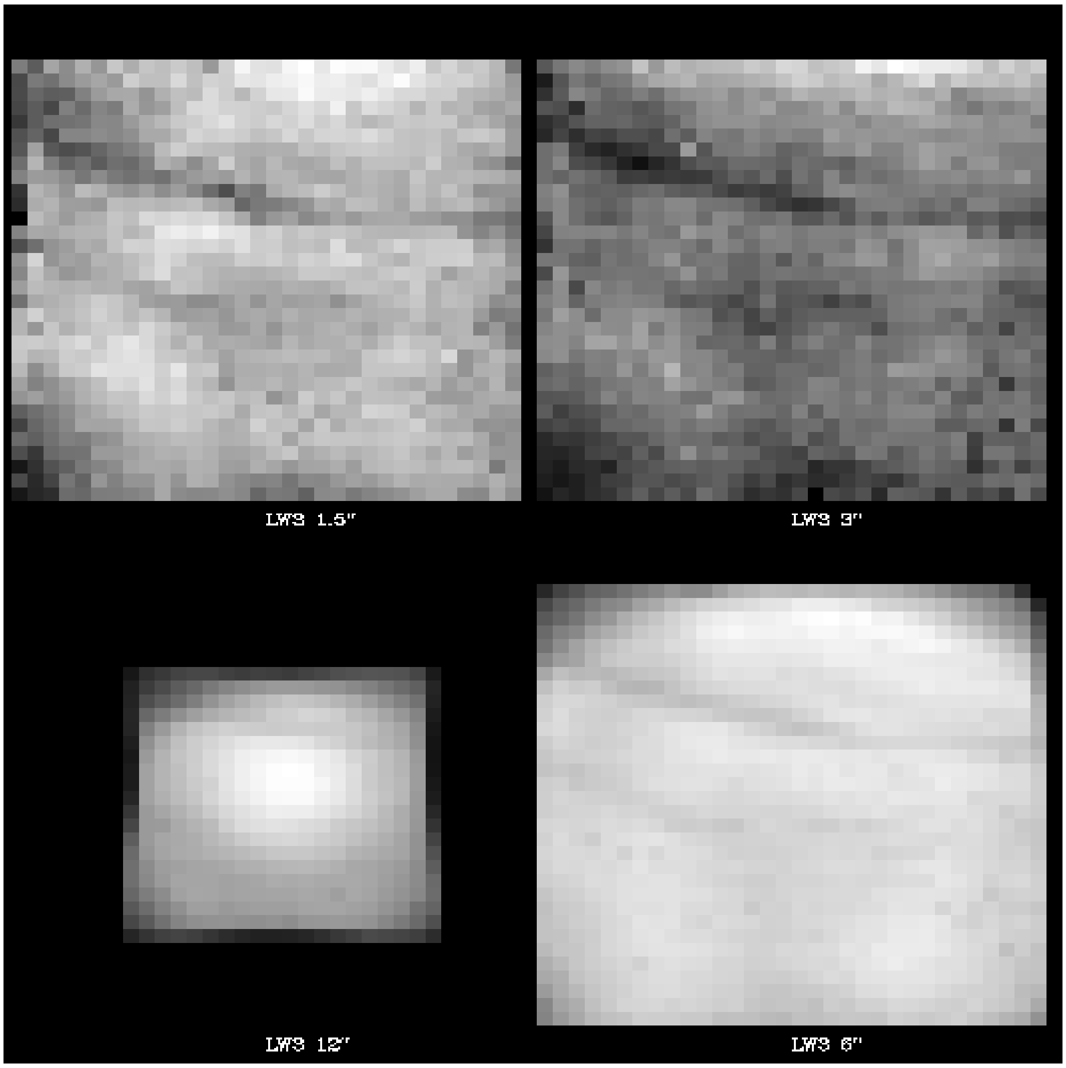

Figure 4.13: *Four examples of zodiacal background flat-fields in the LW3 filter. From top-left in clockwise order: 1.5″, 3″, 6″, 12″ pfov, respectively. Note that in the case of the 12″ pfov, only part of the array is illuminated.*

a faint source per pixel is $\sim$60 μJy (using the ADU/G/s to Jy conversion factors from Blommaert 1998, [10]).

On the other hand, the poor accuracy of only 6% that we have reached for the LW2 1.5″ flat-field gives a 1-σ limit per pixel of $\sim$20 μJy for a typical background flux of 0.8 ADU/G/s in this configuration (note however that in this low background configuration one needs a long measurement to reduce the readout noise). In other words, in the configurations where the background flux is high we need a higher flat-field accuracy, but if the flux is high, a higher ZB flat-field accuracy is easier to achieve. The typical flat-field accuracy is about 1–3%.

4.6 Point Spread Function (PSF)

4.6.1 Observed PSFs

Point source observations were performed with a 4×4 micro-scan raster with a step size of $3''$ for $12''$ pfov, and with a 6×6 micro-scan raster with step size of $2''$ for the other pfov's, in order to obtain a good spatial sampling of the PSFs. However, due to the undersampling of the PSF inherent to some CAM configurations, this did not allow a fine enough sampling of the PSF for every optical configuration. Therefore, users should be aware of this if attempting to use a library PSF for deconvolution purposes.

The micro-scan raster used for the PSF measurements also yields information about photometric variations as a function of the position of the point source within a single generic pixel. The raster spans several pixels, and the point source assumes a range of positions with respect to the various pixels centres. If pixels are assumed to be identical with respect to the variation of response across their surfaces, then the overall raster can be seen as building-up a set of PSFs with families specific to particular relative positions of point source and pixel centre ('sub-pixel positions').

Except for the $12''$ pfov, one raster contains 9 sets of 4 raster points with equivalent sub-pixel positions, within a localised group of pixels. One PSF is constructed by averaging these four point source images. This led, within the detector region covered by each raster, to a set of 9 PSFs expressing the appearance of a point source for each of the 9 particular sub-pixel positions. Therefore, the PSF library contains one set of 9 PSFs for each detector zone rastered for each configuration calibrated. Figures 4.14 and 4.15 show examples of the micro-scans performed for $3''$ and $6''$ pfov PSF measurements. All the rasters for a given optical configuration were done within one observation time block, pointing on the same star.

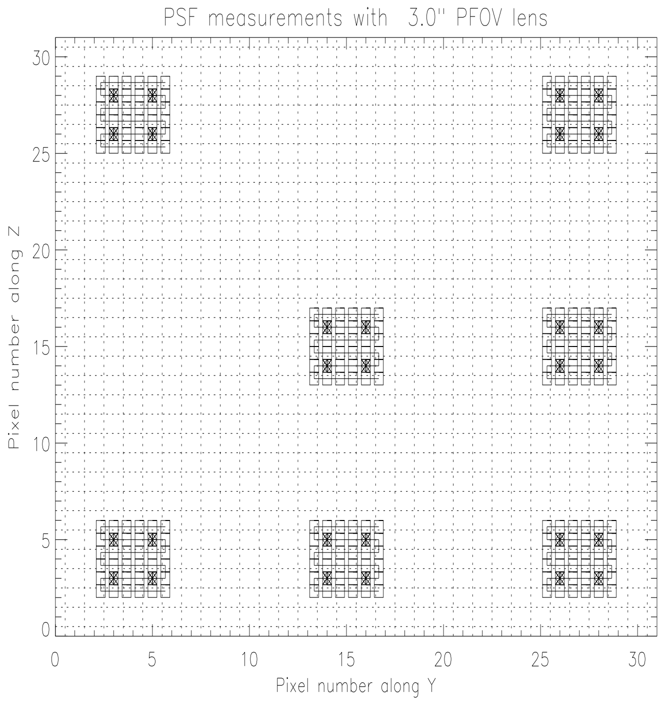

Figure 4.14: *PSF measurements on different regions of the detector for the $3''$ pfov*

All the PSFs of a given configuration are normalised by the flux of the central PSF. This global normalisation factor describes a photometric correction that would need to be applied to point sources as a

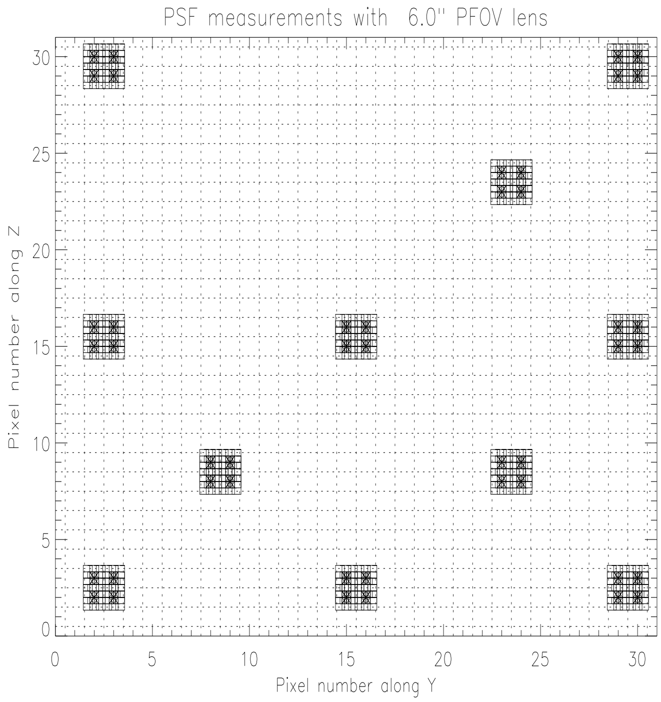

Figure 4.15: *PSF measurements on different regions of the detector for the 6″ pfov*

function of distance from the array centre and/or as a function of source barycentre on the central pixel of the point source. For each configuration, only one PSF is normalised to 1. The normalisation factor is the integrated flux of the reference PSF, excluding the edge pixels.

A detailed description of the observations and analysis made can be found in the *ISOCAM PSF Report* (Okumura 1998, [44]).

4.6.2 Model PSFs

In the optical PSF model computation, the pupil image is created in Fourier space. The pixel size $P_{Fourier}$ in this space is given by:

$$P_{Fourier} = \frac{\lambda}{S \cdot P_{rad}}$$

where λ is the reference wavelength of the filter bandpass, S is the square size of the applied image dimensions expressed by the number of pixels and P_{rad} is the pixel size of the image in the direct space in radians.

The diameter Δ of the circular aperture in Fourier space, in pixel units, is then given by dividing the telescope diameter D by the pixel size $P_{Fourier}$:

$$\Delta = \frac{D}{P_{Fourier}} = \frac{D}{\lambda} S \cdot P_{rad}$$

If λ is expressed in μm, its radius is given by:

$$R = \frac{\Delta}{2} = \frac{0.6 \cdot 10^6}{2\ P_{Fourier}} = \frac{0.3 \cdot 10^6\ S \cdot P_{rad}}{\lambda} \tag{4.2}$$

In order to execute a correctly sampled computation both in Fourier space and in direct space, it is necessary to create a finer sampling and a larger image size than the real image coming from the ISOCAM detectors. If, in addition, one wants to add the detector pixel convolution effect on the optical PSF model, then the sampling in direct space should be better than at least half of the pixel size.

Once the image size is chosen, the central obscuration and the tripod structure (supporting the secondary mirror of the telescope) are added to the main aperture model. The Fourier transform of the aperture then gives the optical PSF which will be convolved by the detector pixel size and resized to the real dimension of the detector array.

For more accurate models, one should integrate over the bandpass profile of each filter multiplied by the spectral energy distribution of the source. However, the theoretical and monochromatic PSF constructed here, can be well compared with the observed PSF as long as the bandpass is not too wide. Thus, the model applied here neglects the impact of the filter bandpass on the shape of the final PSF.

In Figures 4.16, Figure 4.17 and Figure 4.18 the theoretical and the measured PSFs are compared. Details are given in the *ISOCAM PSF Report* (Okumura 1998, [44]).

A comparison of the FWHM of the model (Figure 4.17) and measured PSF (Figure 4.18) to the Airy disk diameter of the ISO telescope demonstrates that a good reproduction of the PSF is obtained for all ISOCAM filters except for LW10 and LW1. The deviation observed in LW10 could be an effect of the very wide bandpass while the anomaly in LW1 is not yet understood.

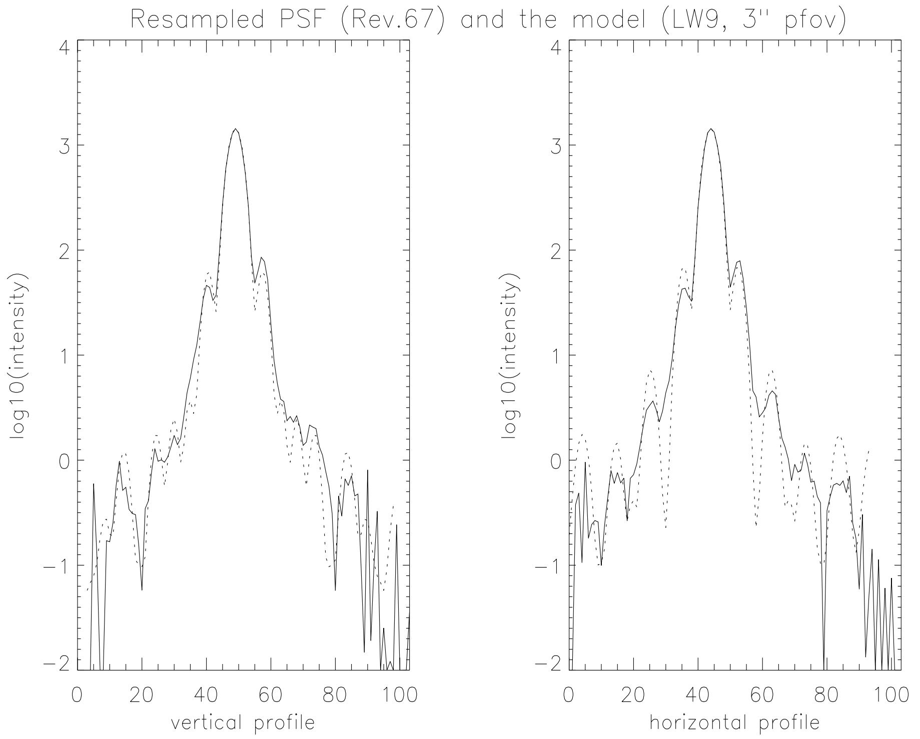

Figure 4.16: *Comparison of the measured and the modelled PSF for the LW9 filter and the 3″ pfov*

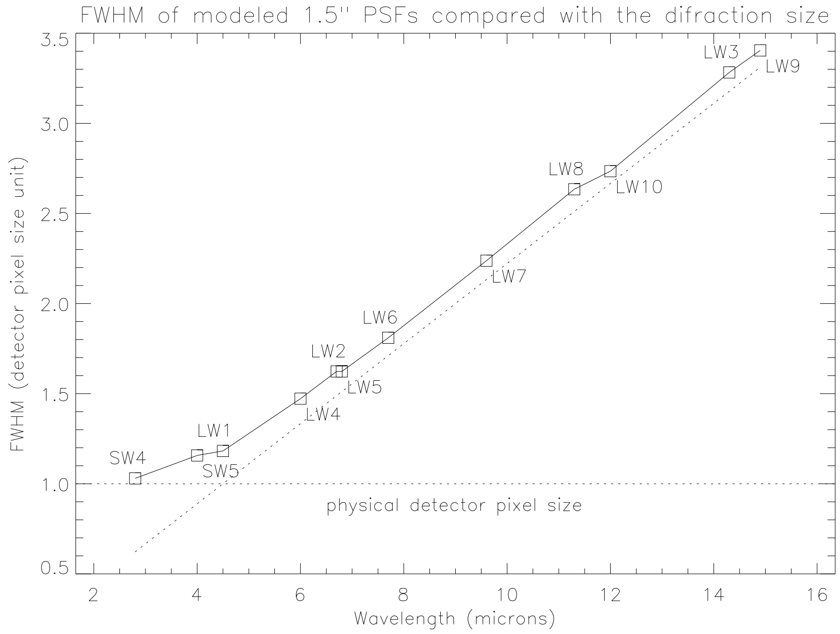

Figure 4.17: *FWHMs of the modelled PSFs. The dashed line is the Airy disk diameter (Section 2.1).*

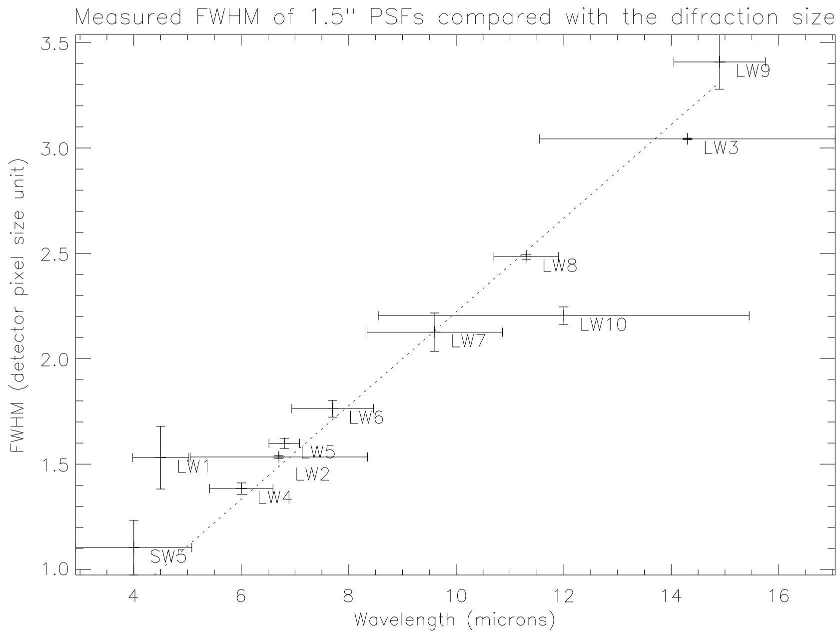

Figure 4.18: *FWHMs of the measured PSFs. The dashed line is the Airy disk diameter (Section 2.1). The horizontal bars indicate the bandwidth of each filter.*

4.7 Spacecraft Pointing Jitter

The ISO pointing system is described in detail in the ISO Handbook Volume I, [40].

It has been shown to yield the following performance:

- random motion of the satellite is 0.5″ (2 σ),
- absolute pointing drift is smaller than 0.1″/hour,
- absolute pointing error (blind pointing accuracy): around 2″ (half cone).

This pointing stability was much better than the pre-launch specifications of the spacecraft.

However, the random spacecraft jitter, although limited to about 0.5″, can cause a slight displacement of a source from image to image, which is most noticeable when a point source is observed.

This pointing jitter has some impact on the data analysis and in principle a correction for this systematic effect would be desirable. So far, despite numerous attempts, none of the proposed algorithms to correct for this effect was very successful. Fortunately, even when using the 1.5″ pfov lens, the influence of the pointing jitter is not dramatic (Figure 4.19).

More details on the jitter correction currently available in CIA can be found in the *ISOCAM Interactive Analysis User's Manual*, [28].

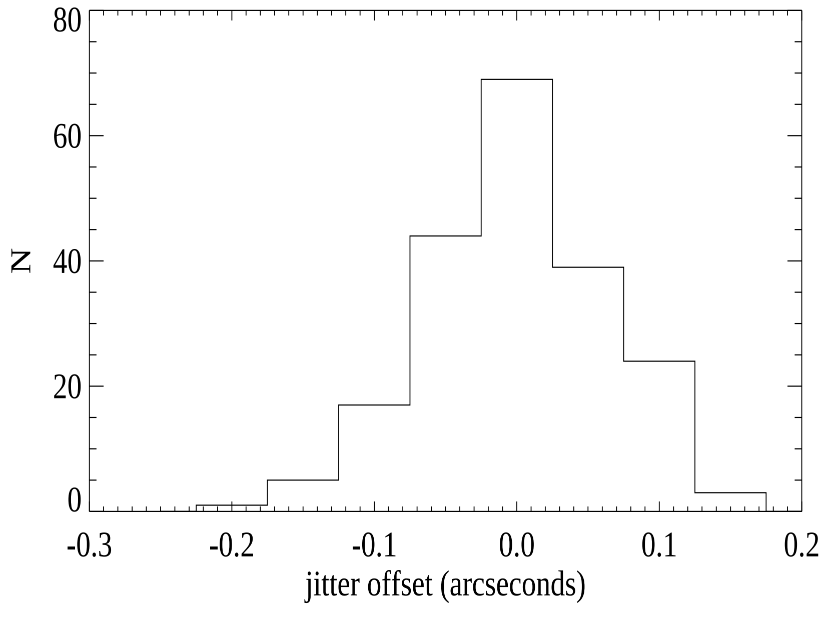

Figure 4.19: *Distribution of pointing jitter offsets as computed with a Gaussian fitting method as available in CIA. Data are taken from observations of the calibration standard star HIC 73005. In this particular case the pointing jitter standard deviation is measured to be 0.065″, a good demonstration of the pointing stability of the ISO telescope.*

4.8 The Spectral Response Function of the CVF

The Spectral Response Function (SRF) has been measured for all CVF segments using photometric calibration stars. The photometry of stars observed in CVF mode was done as described for the filter photometry (Section 4.1.1). For the SW detector, only one star (HIC 96441) was used, for which four individual CVF scan observations were available. For the LW detector, several observations of four stars: Sirius, HIC 96441, δ Draconis and γ Draconis, were used for computing the SRF. The star fluxes were derived using aperture photometry in all cases. Special care was taken to avoid the ghost reflection (see Section 4.9). The integrated ghost flux can be up to a 30% of the star flux and can have a serious impact on the observed spectrum. Thus, for CVF aperture photometry on point sources, it is recommended to use the same apertures used for the calibration standards: radii of 6, 4, 3 pixels for 1.5, 3 and 6″ pfov respectively and a background determination in an annulus 2 pixels wide.

Table 4.3: *Standard stars used for the derivation of the CVF Spectral Response Function.*

Name	HIC	HR	HD	SAO	R.A.	Dec.	Spec. Type
γ Draconis	87833	6705	164058	30653	17:56:36.37	+51:29:20.0	K5III
δ Draconis	94376	7310	180711	18222	19:12:33.30	+67:39:41.5	G9III
-	96441	7469	185395	31815	19:36:26.54	+50:13:16.0	F4V
Sirius	32349	2491	48915	151881	06:45:08.92	−16:42:58.0	A0m

The total signals measured in detector units were divided by the stellar flux densities (in Jy) predicted by stellar models (see also Section 4.1). For this we need to consider that the stars observed for the CVF calibration have quite different stellar types. The spectra of the earlier type stars are dominated by atomic lines whereas molecular bands dominate the spectra of the cool stars. Thus, for the star HIC 96441 (F4V) we used the Kurucz model provided by the Ground Based Preparatory Programme (Hammersley et al. 1998, [36]; Hammersley & Jourdain de Muizon 2001, [37]), while for the other three stars, with later spectral types, we used models provided by Decin et al. 2003b, [27] up to 12 μm and by Cohen et al. 1995, [19] for the longer wavelengths. For more details on the characteristics and limitations of the different models used see Decin 2001, [25]. Their usage for the CVF calibration is discussed in Blommaert et al. 2001a, [12]; 2001b, [13].

A weighted average of all the resulting SRF estimates was computed, after carefully excluding measurements strongly affected by transient effects. The final SRFs were smoothed using a 3-pole digital low-pass filter, with a cut-off at 25%, in order to reduce the noise features (that could be misinterpreted as spectral lines when the SRF is used to derive the spectrum of a given object).

The derived SW CVF SRF is shown in Figure 4.20 together with the associated error bars, which do not include systematic errors, i.e. due to 'ghosts' (see Section 4.9). The average random error of the SW CVF SRF is ∼3%, but for some SW CVF positions the error can be as large as 23%.

Before determining the average LW SRF, all measurements were corrected for the change of responsivity in orbit (a decrease of 6% from start to end, as was shown in Section 4.1.2). This correction reduced the overall rms from 4% to 3%. The observations divided by their input spectra are shown in Figure 4.21. The repeatability of the CVF photometry *on the same star* is excellent, ±3% rms.

The rms of the LW CVF1 SRF is 3% of the measured value, on average, and always less than 5%, except for the CVF step positions of the shortest (4.96 μm, rms = 11%) and the longest wavelength (9.58 μm, rms = 48%). Fortunately, the longest wavelength of LW CVF1 is also covered by the LW CVF2, with a much higher accuracy. The mean rms of the CVF2 SRF is 4% of the measured value. Originally, a wavelength range was offered to the observer from 9.003 to 16.52 μm. The SRF at CVF positions outside the recommended range is also available in the calibration files, but these are affected by larger errors (still below 10% rms up to 17.16 μm but up to more than 100% for the extreme position at 17.34 μm). When

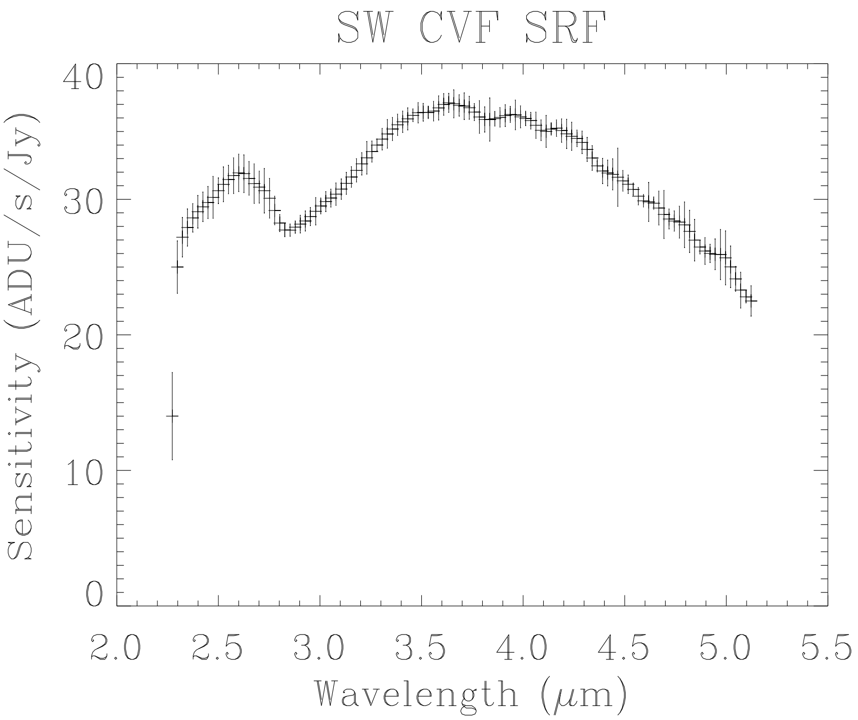

Figure 4.20: *The SW CVF SRF within its* $\pm 1\sigma$ *confidence band, where* σ *is the rms derived from the set of measurements used to obtain the SRF.*

analysing a CVF spectrum of an astronomical target, the largest uncertainties come from the reflected light (Section 4.9) and the long time needed to stabilise the measured signal (Section 4.4) which will affect mostly the beginning of a CVF measurement or when there is a change between CVF segments.

The resulting CVF SRFs and their error bars are given in the calibration files CSWCVF, CLWCVF1 and CLWCVF1 (Sections 6.1.15 and 6.1.16).

The determination of the SRF of the LW CVF is described in detail in Blommaert et al. 2001a, [12] and for the SW SRF in Biviano et al. 1998b, [6].

4.8.1 Spectral purity

From observations of planetary nebulae taken during the PV Phase, the central wavelengths of two lines, [Ne II] $\lambda 12.81$ μm and [S IV] $\lambda 10.51$ μm, were derived (by simple Gaussian fitting over the continuum). They were found to fall at the expected CVF scan positions, within a few hundredths of a CVF step. Transient effects may slightly change the observed position of the line, by less than a tenth of a CVF step.

However, the wavelength purity is reduced when the source is not centred at the middle of the array. An analysis of the [Ne III] λ 15.55 μm line central position in an ISOCAM CVF image of M17 showed that the central observed wavelength position of the [Ne III] line was red-shifted 0.09 μm at the left edge of the ISOCAM array compared to the observed wavelength at the centre. At the position of CVF2 corresponding to the wavelength of the [Ne III] line such a shift corresponds to roughly one CVF step. At the right edge of the ISOCAM array, however, there is no significant wavelength shift.

On the other hand, there is no wavelength-dependence in the top-down direction of the array, as expected

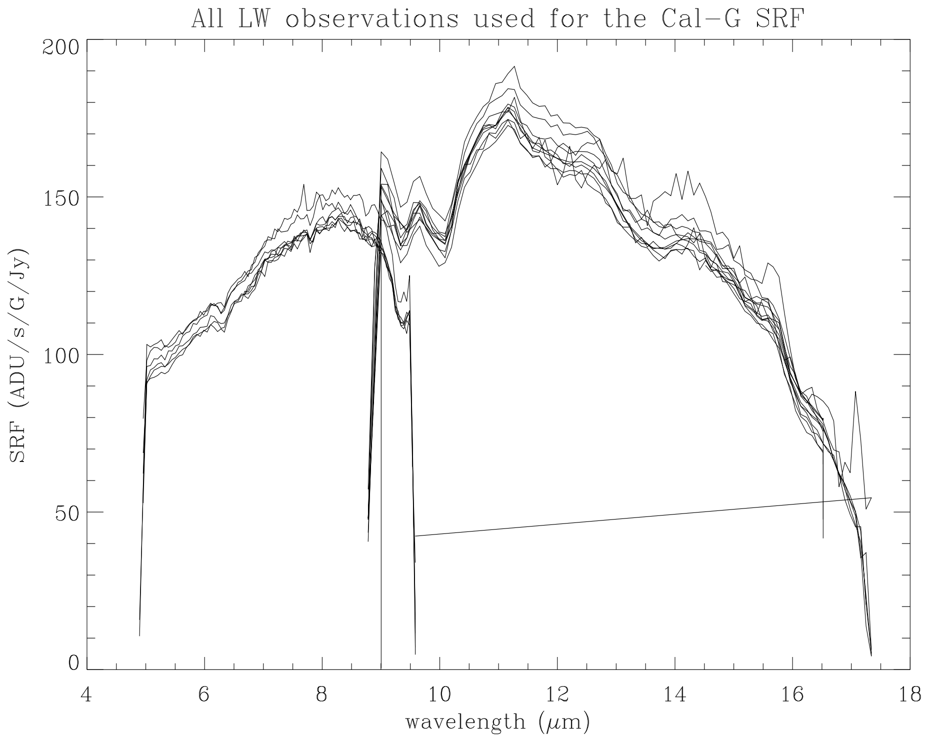

Figure 4.21: *The different LW SRF determinations based on the observations of 4 different calibration stars. It includes different pfov measurements. The rms is 3–4%.*

from the orientation of the CVF with respect to the array. In addition, there is an indication that the wavelength shift is wavelength dependent, being larger at longer wavelengths.

4.9 Ghosts and Straylight

Ghost images and straylight affect any kind of photometry or morphology studies (Okumura et al. 1998, [45]; Blommaert et al. 2001a, [12]). The ISOCAM ghost image is formed after 2 reflections: on the detector and on the filter. For the fixed filters these effects could be minimised by tilting the filters with respect to the beam path. For the CVF making a tilt to avoid ghost and straylight effects was not possible due to the physical structure of the CVF and the constraints on its mounting. Thus both effects were expected to cause some problems in CVF data.

4.9.1 Ghost images from point sources

In Figure 4.22 three independent observations of the same star, δ Draconis, done with the CVF in the 6″ pfov, at a wavelength $\lambda = 7.358$ μm are shown in a logarithmic intensity scale. In one of the observations, the star's image was put at the centre of the detector array, in the other two, the source was placed in the bottom left and right corners of the array.

Two types of ghost images can be seen. One has a ring-like appearance and is comoving with the source image. The other has a point-like shape and moves symmetrically with respect to the ISOCAM array centre, as the source moves. Other images and movies of these ghosts are available in the ISOCAM web

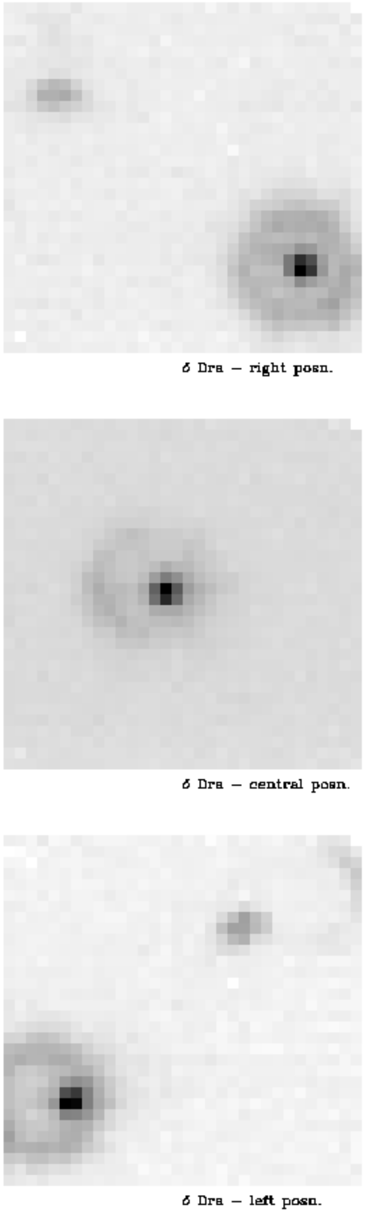

Figure 4.22: *Ghost images in three CVF observations of δ Draconis. Intensity scales are logarithmic.*

pages at:

`http://iso.vilspa.esa.es/` → `ISO Explanatory Library` → `CAM`

The ratio between the integrated ghost signal and the signal from the star can reach up to 30%, for the *comoving* ghost, and 9% for the *symmetric* ghost. Although the latter ghost contains less flux, it is very apparent in an ISOCAM image as the brightest pixel reaches a brightness (about 4% of the point source flux) which is comparable to that of the comoving ghost. The spectral dependency of the ghost contribution can be seen in Figure 4.23, taken from Blommaert et al. 2001a, [12].

In order to avoid systematic errors in the CVF photometry one must be aware of the ghost flux contribution. Since the SRF was derived without including the ghost flux in the estimation of the total flux

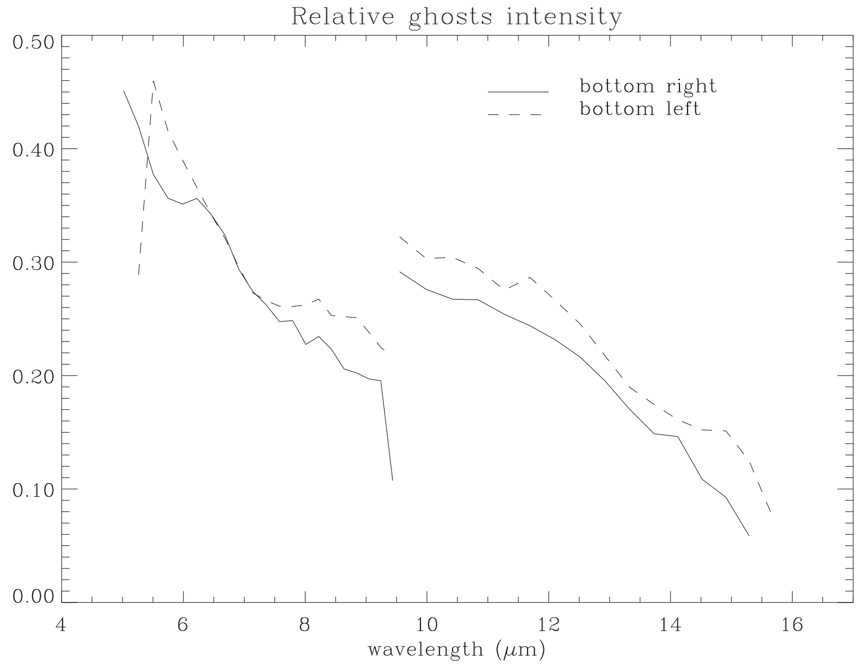

Figure 4.23: *The summed relative intensity of the first and secondary ghosts normalised to the point source flux in the main beam at 2 positions on the detector as a function of wavelength.*

from a star, for consistency observers *should not include the ghost flux* in the estimation of the total flux of a given source. For a discussion on the way this can be done see Blommaert et al. 2001a, [12]; 2001b, [13].

4.9.2 Ghosts and straylight from extended sources

Straylight from extended sources was investigated through observations of the zodiacal light with three CVF step positions (corresponding to the wavelengths of 7.7, 11.4 and 15 μm), and in all pfov's.

In Figure 4.24 we show the image obtained on the zodiacal light emission at 11.4 μm with 12.0$''$ pfov. Standard data reduction without flat-fielding was applied. In this configuration, the field mirror acts as a field stop, and only the central 16×16 pixels of the detector array should be illuminated. However, one can see from the figure that the region of the detector not covered by the field mirror is not completely dark and the field mirror edges are not sharp. This is mainly due to the ghosts of the extended source and to a lesser extent to straylight. The total flux outside the field mirror region sums up to ∼25% of the flux within the region covered by the field mirror.

Ghosts and straylight caused an important limitation to CVF images. In CVF images, real physical structures with an average per-pixel flux ≤10% of the background are hard to detect. Figure 4.25 shows an example of a CVF image of the 'flat' zodiacal emission. Indeed, the ghosts and straylight pattern may lead to *mis-interpretations* of the CVF images, e.g. the ghost pattern could be incorrectly attributed to extended emission around a target star. Of course, the situation gets worse when bright sources outside the field of view also contribute as straylight. In Blommaert et al. 2001a, [12] a method is presented to correct zodiacal CVF spectra for straylight radiation. However, the method has not been tested on CVF observations of extended emission with contrasted sources.

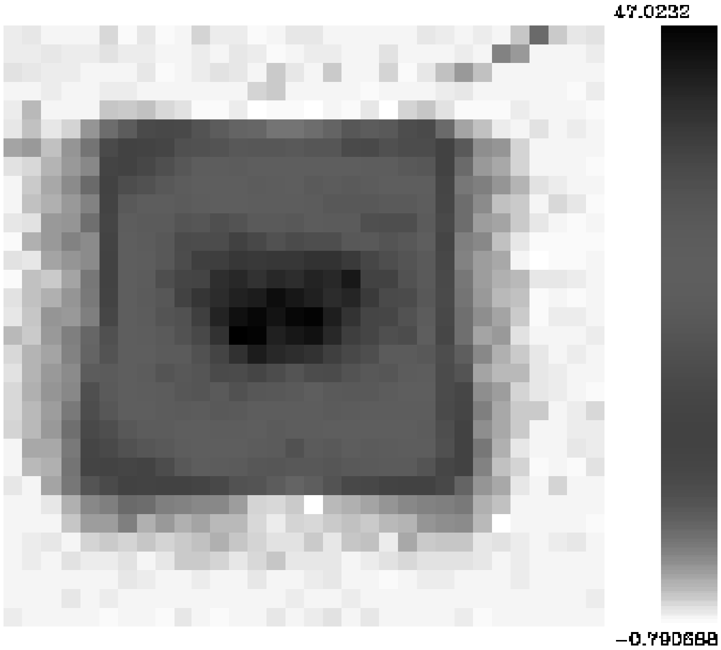

Figure 4.24: *An image of the zodiacal background taken with the CVF at 11.4 µm, with 12.0′′ pfov. Flux units are ADU/G/s. Note that even outside the field stop, outside the central 16×16 pixels, the detector shows illumination*

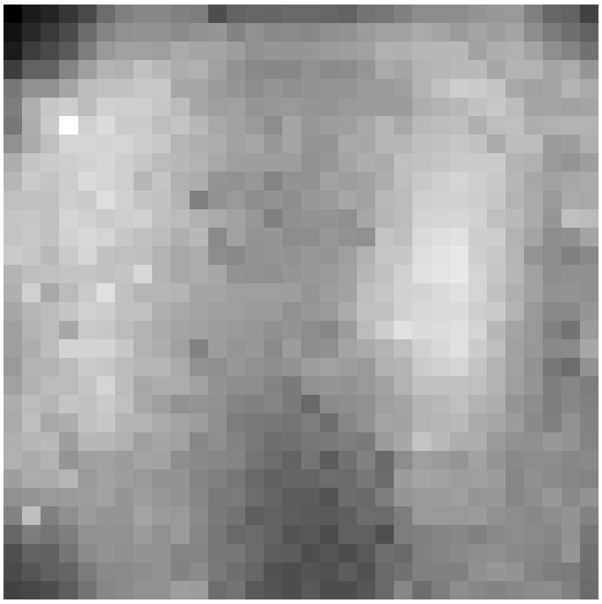

Figure 4.25: *The so-called 'two-lung' shaped ghosts in a flat extended source*

4.10 Field of View Distortion

ISOCAM images suffer from a field distortion caused by optical elements like the field mirror, filter and lens. Each of these elements acts in a different way and to a different extent. The inclination of the Fabry field mirror causes a trapezoidal deformation observed in the distortion pattern. This effect is reproduced in a simple first order optical computation. Pincushion distortion occurs when the beam passes through the lens and is caused by the aspherical aberration of the lens. In this case, first order computation is not sufficient to account for the effect. The width of the filter plates contribute also in a magnification change. As the beam is converging when passing through the filter, the parallel planes of the filter plates (whether inclined or not) have an influence on the field pattern on the detector. An example of a field distortion pattern derived from a raster observation through the 6″ pfov lens with the LW1 filter is shown in Figure4.26.

It is important to correct data for this instrumental effect, especially when making a coadded map from a raster observation and also when improved astrometry is needed. The correction is made by means of a pair of polynomials which relate the distorted two-dimensional space to a distortion-free two-dimensional space.

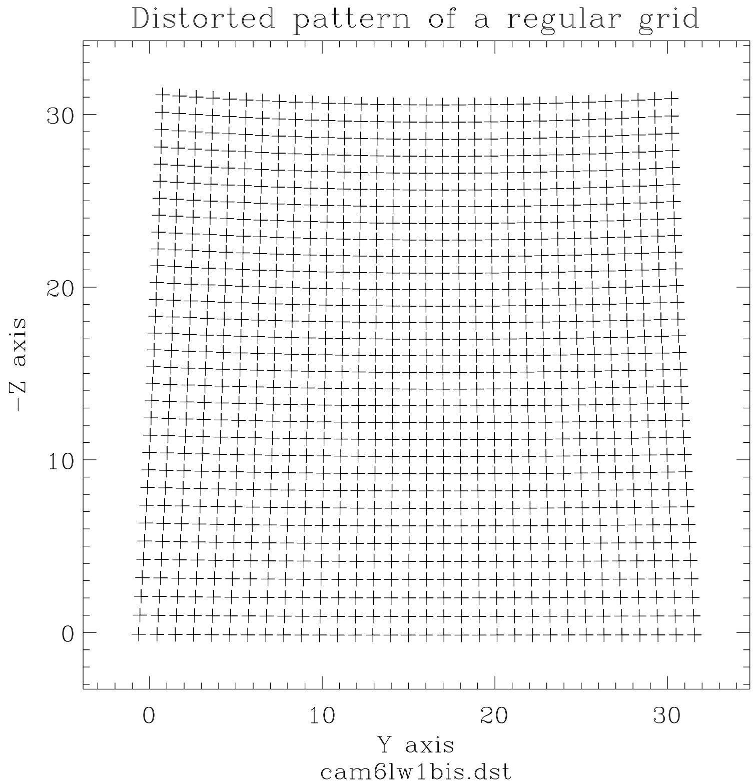

Figure 4.26: *A typical field distortion pattern derived from a raster observation through the 6″ pfov lens with the LW1 filter*

The distortion is weak through the 1.5″ pfov lens and becomes stronger for larger pfov's. The field distortion also depends on the filter. Figure 4.27 shows the wavelength dependency seen in the data by means of the magnification parameter derived from the linear terms of the fit polynomials.

The field distortion correction includes polynomial coefficient sets for the different filters. There are two types of coefficients. One derived from measurements and the other from a ray-tracing optical model which was optimised to fit the observations. Measurements on real data are possible in the case of the 6″ and 12″ pfov lenses. The distortion measurement through the 3″ pfov lens was difficult because the effect which had to be measured was of the order of the accuracy of the point source position determination routine. The distortion amplitude is even smaller through the 1.5″ lens, and is therefore impossible to measure in the real data.

In CIA the distortion polynomial coefficients are available in a CAL-G file called 'clwdisto_*.fits'.

For the ISOCAM configurations for which no accurate measurement was possible or for which no data are available, the coefficients are derived from the optical model. A more detailed discussion on this subject can be found in the *ISOCAM Field Distortion Report* (Okumura 2000, [46]).

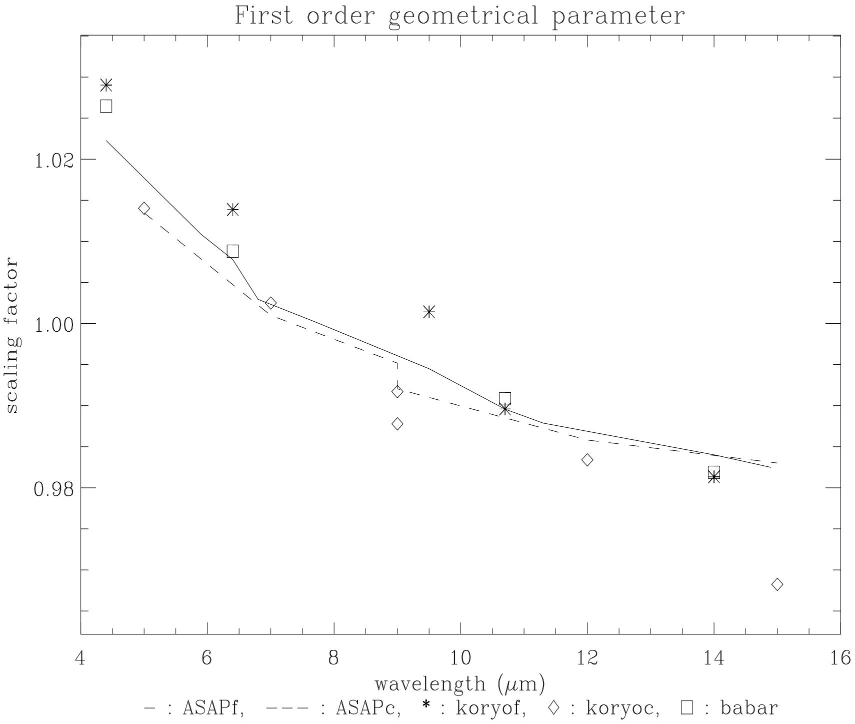

Figure 4.27: *Scaling factor of the distortion correction polynomials with respect to the detector centre. ∗ : filters (from ghost measurements), ⋄ : CVFs (from ghost measurements), □ : new data sets. Solid line: filters model; dashed line: CVFs model (Okumura 2000, [46]).*

4.11 Astrometric Uncertainties

Due to the superb pointing accuracy of the ISO telescope, the astrometric uncertainties should be small, even when considering the pincushion distortion (up to 1 pixel for the 6″ pfov, and 0.5 pixels for the 3″ pfov). However, operating the instrument at liquid helium temperatures, and accommodating severe launch vibrations, required mounting the camera wheels with a small amount of positional 'play'. This translates into some unrepeatability in the position of a wheel at the end of each motion. This 'wheel (positioning) jitter' may cause an apparent shift of the source position by up to 2 pixels from the nominal pointing position (see Figure 4.28). Such a shift may be associated with any change in optical configuration. Mainly, it occurs only by moving the lens wheel and remains unchanged for rotations of the filter wheel. For most observations, the lens wheel was not moved during the measurement (AOT). In this case one has to allow only for a constant shift of the absolute astrometry in the resulting map or image.

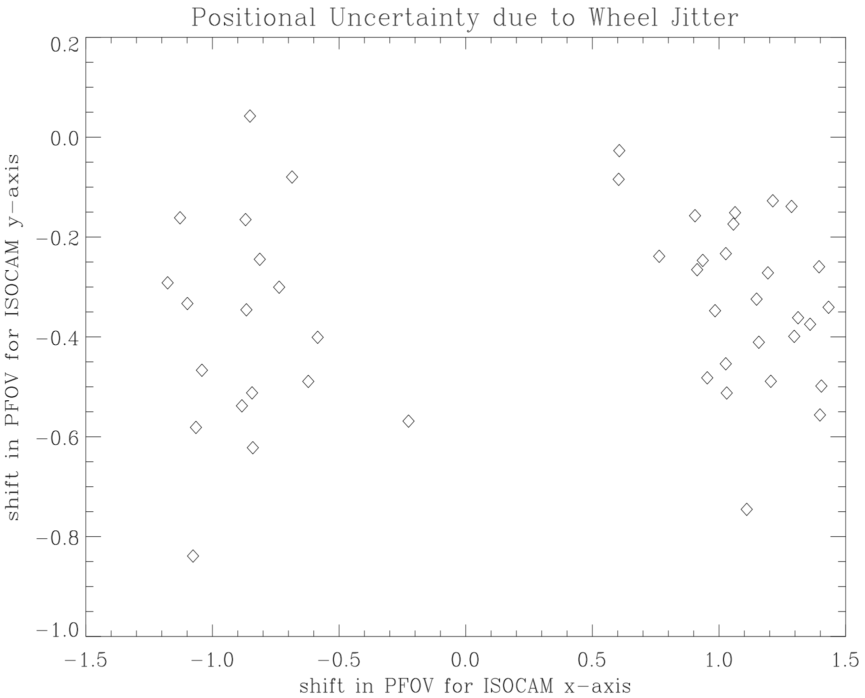

Figure 4.28: *Positional uncertainty due to the lens wheel jitter*

4.12 Instrumental Polarisation

The Stokes parameters measured on astronomical targets may be contaminated by unplanned polarisation within the instrument and polarisation of the sky background. The instrumental polarisation must be derived. However, this requires knowledge of calibration parameters such as the polariser throughputs and their polarisation efficiencies. Both of these parameters could not be derived from laboratory measurements at the required accuracy.

We here introduce polarisation weight factors (w_i) applied to the measured polariser intensities S_i. The polarisation weight factors serve as calibration parameters to correct for the instrumental polarisation.

They are given by:

$$w_i = 2 \cdot \frac{S_i}{I} \tag{4.3}$$

and its standard deviation can be estimated according to:

$$\Delta w_i = \sqrt{(2 \cdot \frac{\Delta S_i}{I})^2 + (2 \cdot \frac{S_i \cdot \Delta I}{I^2})^2} \tag{4.4}$$

where I is the total intensity as measured through ISOCAM's entrance hole, ΔI is its standard deviation and ΔS_i is the standard deviation of the three polariser intensities.

We define the corrected intensities as:

$$s_i = \frac{S_i}{w_i} \tag{4.5}$$

The best measure of the instrumental polarisation is given by CAM05 raster observations on the zodiacal background. Assuming that the zodiacal background is flat and unpolarised, it is natural that any measured degree of polarisation should reflect the instrumental polarisation of ISOCAM. For the zodiacal light, we therefore write the Stokes parameters as:

$$S(zodi) = (I, 0, 0). \tag{4.6}$$

The weight factors (w_i) for all observed configurations are given in Table 4.4. If one sets the polarisation weight factors to unity, one derives from the zodiacal light images a polarisation vector. Those vectors are given in Table 4.5. They do not suggest a dependency on wavelength nor on lens (pfov). Already for the 3″ pfov the signal of the zodiacal light tends to be weak and yields poor precision. For the 6″ lens the mean instrumental polarisation is around $p = 1.0 \pm 0.3\%$.

Table 4.4: *Polarisation weight factors w_1, w_2 normalised to w_3 = 1.*

Filter	λ_{ref} [μm]	lens [″]	w_1	Δw_1 [%]	w_2	Δw_2 [%]
LW2	6.7	6	0.9862	<0.1	0.9937	<0.1
LW10	12.0	6	0.9763	<0.1	0.9926	<0.1
LW8	11.3	6	0.9829	<0.1	0.9886	<0.1
LW3	14.3	6	0.9845	<0.1	0.9937	<0.1
LW9	14.9	6	0.9873	<0.1	0.9957	<0.1
LW7	9.6	3	0.9824	2.1	0.9845	1.9
LW8	11.3	3	0.9638	3.0	0.9740	3.0
LW3	14.3	3	0.9614	0.4	0.9987	0.2
LW9	14.9	3	0.9749	2.0	0.9865	2.2
LW3	14.3	1.5	0.9737	4.4	1.0022	4.2

Table 4.5: *Instrumental polarisation.*

Filter	λ_{ref} [μm]	lens [″]	p [%]	Θ [°]
LW2	6.7	6	0.80 ± 0.1	24 ± 4
LW10	12.0	6	1.41 ± 0.1	29 ± 3
LW8	11.3	6	1.02 ± 0.1	18 ± 3
LW3	14.3	6	0.91 ± 0.1	26 ± 3
LW9	14.9	6	0.75 ± 0.1	28 ± 4
LW7	9.6	3	1.12 ± 1.28	11 ± 37
LW8	11.3	3	2.20 ± 2.05	16 ± 27
LW3	14.3	3	2.56 ± 0.90	37 ± 18
LW9	14.9	3	1.47 ± 1.47	22 ± 27
LW3	14.3	1.5	1.85 ± 3.3	40 ± 38

The zodiacal light calibration observations give a good measure of the LW flat-fields (Biviano et al. 1998c, [7]). By combining the flat-fields through the polarisers to calculate, for each detector element, a Stokes vector, residual polarisation patterns can be noticed. There is no strong dependency of the polarisation pattern on the filter. It is quite similar for the 1.5″ and 3″ lens but shows a more aligned structure using the 6″ lens. One corrects for this instrumental pattern in the data by using the polarisation flat-fields. If such flat-fields cannot be derived from one's own observation one may use those stored in the calibration flat-field library. For a detailed description of CAM's polarisation capabilities and how the instrumental polarisation was determined see Siebenmorgen 1999, [55].

4.13 Global Error Budget

The uncertainties in the ISOCAM measurements depend on a variety of factors. Actually, there should be a specific error budget for each observing mode, depending on a number of parameters such as exposure time or optical configuration. The specific error budget will of course depend on the version of calibration libraries and on the signal processing algorithms used. In Table 4.6, a global list of instrumental effects contributing to the uncertainty budget is compiled. The estimated magnitudes of the various effects are given for typical circumstances. Column 2 refers to the relative error before data are corrected. In column 3 typical magnitudes are given of residuals still present after using available calibration methods.

Table 4.6: *Summary of the error budget for ISOCAM calibration, from Biviano et al. 1998d, [8]*

Noise origin	Magnitude	Residual After Correction
Stabilisation (systematic)	40% source flux	15% source flux (point sources) 1% source flux (extended emission)
Saturation	≥30% decrease in responsivity	
Read-out noise	LW: 0.7 ADU/G SW: 2 ADU/G	
Gain	0.15% output signal	
Dark current	LW: 0.5 ADU/G SW: 0.5 ADU/G	0.25 ADU/G
Flat-field	LW: 0.5% (high background) SW: ≤1%	
Sensitiv	5%	
PSF (photometric correction)	20%	few %
PSF (pixel position)	≤3%	
CVF SRF	3%	
CVF spectral purity	≤1 CVF step	
Ghost	≤25%	
Straylight	10% sky flux	
Astrometry (pointing)	3″	
Astrometry (jitter)	±2 columns	
Astrometry (field distortion)	1 pixel	1/3 pixel

Non-ideal behaviours of the instrument include:

- the long stabilisation times after flux changes

- the memory effect of the detectors
- the response variations after glitches
- the astrometric uncertainties
- the straylight induced by CVF filters
- the field distortion.

One may crudely estimate basic uncertainties of ISOCAM observations by using numbers as specified in Table 4.6. This table should make it obvious that any ISOCAM observer should try to correct for these various effects to the best of their knowledge. For a detailed review of the error budget see the *'ISOCAM Calibration Error Budget Report* (Biviano et al. 1998d, [8]).

Chapter 5

The Data Products

5.1 Pipeline Processing

In common with the other instruments, every ISOCAM observation was subject to an automatic processing, known as the *pipeline* or OLP (Off-Line Processing). What was anticipated to be the final OLP v10 software was released in 2001 July. The pipeline ends with the ingestion in the ISO Data Archive (IDA) of products designed both for further analysis and to afford an initial assessment of the scientific value of the observational data. There are many different products involved. While the most immediately useful ones are probably those few that report images and point source measurements in physical units that are available for instant inspection in IDA (see Section 7.4), there is a variety of supporting material whose primary purpose is to provide a complete set of raw ingredients to enable the user's own analysis of whatever complexity. While most of the products are unique to ISOCAM, some hold auxiliary data, such as schedule, pointing and orbital information. This chapter describes the ISOCAM specific data products available in IDA and reviews the methods used in their derivation. Any caveats of which the user should be aware when interpreting these products can be found in Chapter 8.

ISOCAM data products result from one of the following tasks:

- automatic off-line data analysis of all observations;
- in-orbit calibration of dark currents, flat-fields, point spread functions, etc;
- ground calibrations;
- `Quick_Look_Assessment` of near real-time data from the satellite.

The products are written in standard FITS format following the definition of NOST standard 100-1.0,[43] and so offer the advantages of a high degree of self-description and the ability to use a great deal of public domain custom software such as `fv` , [34]. All files conform to a relatively simple FITS implementation of either a single PRIMARY image (usually empty) and associated header containing card-image header records of the form KEYWORD=VALUE, labelled HDU=0 according to the `fv` convention, or a single BINARY-TABLE extension of rows and columns and associated header, labelled HDU=1. Below, the header in HDU=n is called CPRO[n].HEADER; individual header records CPRO[n].KEYWORD; the BINARY-TABLE CPRO[1].TABLE with individual columns CPRO[1].COLUMN(*). While a set of keywords used across all products describes the relevant software and calibration data releases, the complete set of input files used and other common data, most HEADER keywords and TABLE columns are product specific. The layouts of all FITS products are collected in the *ISO Data Product Document* (Saxton 2000, [52]) which is a useful document to use with `fv` for examining and understanding the products available. Record alignment often required the use of one or more fillers in TABLE records that are of no practical interest with names such as CCSH[1].CSGPFILL(*), CIER[1].FILLER6(*) or CPSL[1].SPARE(*).

Product filenames are made up of a descriptive alphanumeric root and, if necessary as is usually the case, a numerical suffix reflecting the file's applicability of 8 digits for an individual observation or 3 digits for a revolution. For example, CMOS44900303 contains one observation's mosaic and APPH449 contains summary pointing data for one revolution. The descriptive root alone, without any applicable suffix, such as APPH or CMOS, is often used in the discussion below.

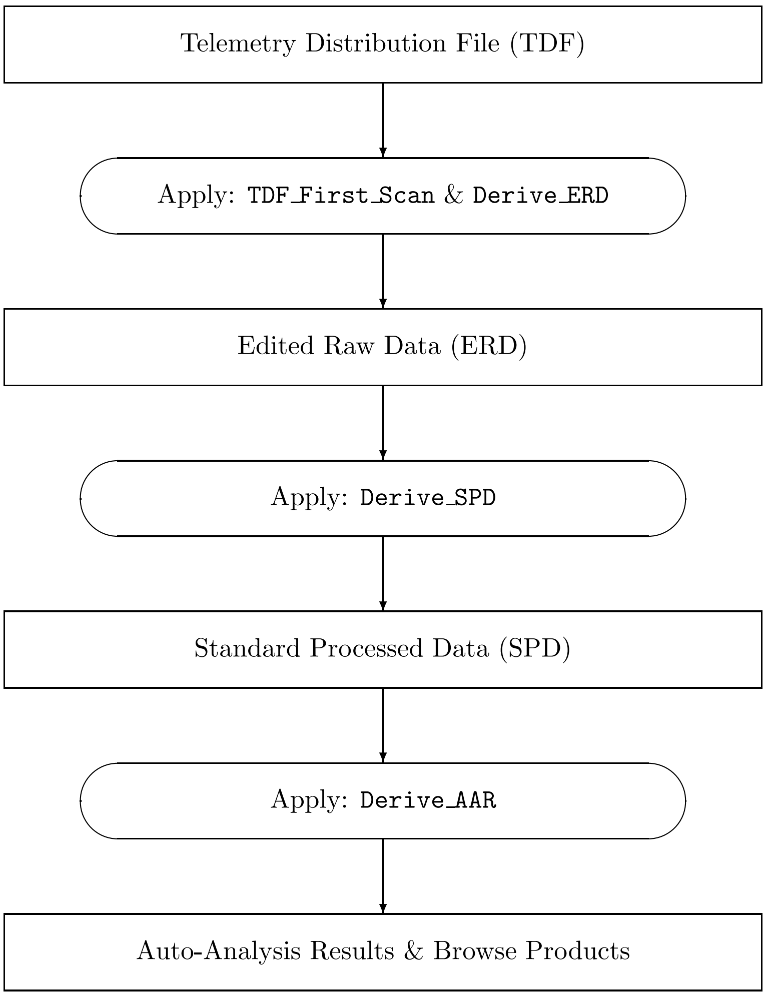

Figure 5.1: *Overview of the ISO data processing pipeline.*

The overall processing scheme is represented in Figure 5.1. Satellite data received at the ground station were assembled into Telemetry Distribution Files (TDFs), making available complete information about

Table 5.1: *Overview of the different categories of ISO products.*

Product name	General category	Processing stage	OLP v10 application
TDF	Raw Telemetry	`TDF_First_Scan`	`TDF` v2.2.2
ERD	Edited Raw Data	`Derive_ERD`	`ERD` v4.0.3
SPD	Standard Processed Data	`Derive_SPD`	`SPC` v4.1.2
AAR	Auto-Analysis Results	`Derive_AAR`	`AAC` v10.3

the satellite and its subsystems for one revolution. TDFs are not in FITS format and, thus, are not suitable for use by the general observer. Instead, they were the starting point of the processing system that ended with the ingestion in IDA of a set of quality-checked data products. Products fall into different general categories which are shown in Table 5.1 along with the applications used in the latest OLP release.

As discussed in more detail below, both `TDF_First_Scan` and `Derive_ERD` are common applications for all ISO instruments. They combine general purpose and instrument specific procedures. Both operate at TDF level. Selected data are extracted by `TDF_First_Scan` into low level files that are mainly for internal use by OLP later in the pipeline while scientific data are extracted, decoded and recast into ERD by `Derive_ERD`. ERD are the first FITS-format products available for general use and contain a complete set of raw ISOCAM data for an individual observation without calibration or conversion. Two other important tasks are performed at these early stages of the pipeline: `TDF_First_Scan` calculates the synchronisation between the different ISOCAM time keys that hold good for a whole revolution; and `Derive_ERD` calculates all the relevant pointing files. General purpose products are described elsewhere, in the ISO Handbook Volume I, [40]. Although ERD can serve, for example, as a starting point for interactive analysis with CIA, the following stage of `Derive_SPD` performs some useful initial data selection and reduction. It extracts status and housekeeping information; logs statistics on detector data; does the first stages of image construction; and writes the SPD. Apart from supplying data for `AAC`, the next stage of the pipeline described in Chapter 7, SPD is also the normal starting point for interactive analysis with CIA.

5.1.1 ISOCAM use of time keys

While the various time keys used in ISO products are discussed fully in the ISO Handbook Volume I, [40] a few ISOCAM-specific points are worth bearing in mind in the context of their main purpose of enabling synchronisation of different types of data. The ISOCAM instrument has its own clock giving the Instrument Time Key, or ITK, which is reported in the General Science Prefix, or GSCP, that forms part of every row of raw data as in CIER[1].GSCPTKEY(*), for example. One of `TDF_First_Scan`'s jobs is to calculate a clock calibration that holds for the entire revolution that is made available in the header of the CCSH file in CCSH[0].CAMITK0 and CCSH[0].CAMUTK0. These are the values of ITK and UTK, respectively, when an internal counter is reset to zero near the beginning of a revolution. They are used to calculate the ITK of each individual CIER record

```
CIER[1].GSCPTKEY(*) = ITK = CCSH[0].CAMITK0+CIER[1].F2BOOTTI(*)    ! CAM prime only
```

A similar formula applies to CAM parallel using CCSH[0].CAMUTK0. ITK is related to UTK by a set of keywords calculated for every observation and inserted in the primary header of raw data files. In CISP12900907, for example, the following values apply:

```
TREFUTC1=            228128772 / UTC (whole seconds since 01-01-1989)
TREFUTC2=              5112273 / UTC (remaining fraction of second)
TREFUTK =            301458521 / ISO Uniform Time Key (UTK)
```

```
TREFITK =             89720116 / ISO INSTRUMENT Time Key (ITK)
TREFITKU=     0.13999950000000 / ITK unit length in seconds
```

Work done during the course of the mission enabled an accurate estimate of the unit of ITK. Users of data retrieved from early archive releases may find a slightly different value.

5.2 Operation of the ISOCAM Instrument

For a better understanding of the products we describe here some of the aspects of how the detectors were operated (see Chapter 2 for a more general description.). Either the LW or the SW channel, was in use at any one time. At the beginning of the selected integration time, the pixels were reset to a constant charge and read out, after which the detector was exposed to incoming radiation for the integration time and read again. The quantum of measurement consists, therefore, of a pair of RESET and end-of-integration (EOI) frames and both are usually present in the TDFs. The physically significant quantity proportional to flux is (EOI−RESET) which is stored along with RESET values in SPD. The exceptions are for the shortest integration time, T_{int}=0.28 s, and when ISOCAM was operating in parallel mode, when telemetry limitations made the use of on-board integration in the accumulated readout mode necessary (Section 2.4.1) for which RESET values are not available. CAM usually operated continuously from switch-on during activation at the beginning of a revolution until de-activation at the end. When CAM was designated prime instrument, data were downloaded via the 24 prime frames of the 32-frame 2 s telemetry block; otherwise a single frame was reserved for parallel mode.

An individual (EOI−RESET) EXPOSURE is the lowest in a hierarchy of structures that reflect the instrument's operation and move up through STATE, OP-MODE, CONFIGURATION and AOT.

STATEs are series of one or more EXPOSUREs at fixed instrumental settings.

OP-MODEs are series of STATEs of at most one of the following types:

- **OBS** : sky exposure
- **DRK** : dark current measurement
- **CAL** : internal flux calibration
- **CLN** : detector reset flash
- **IDLE** : ISOCAM off

CONFIGURATIONs are series of OP-MODEs at fixed instrumental settings.

AOTs are series of one or more CONFIGURATIONs performed on a given target.

The Astronomical Observation Template, or AOT, is identified with an observation as a whole and is of one of the types discussed in detail in Chapter 3. A CONFIGURATION has between one and five OP-MODEs of different types, in the order defined by the original observer, including one OBS OP-MODE only. According to the AOT, a CONFIGURATION's central OBS OP-MODE will encompass one of the following:

- an entire staring mode observation;
- one observation of each point in a raster;
- one observation of each position in a beam-switch;
- one observation of each wavelength in a CVF scan;
- one observation of each polariser in a polarisation measurement.

The fixed instrumental settings that apply during a CONFIGURATION and particularly during its OBS OP-MODE are as defined by the following parameters, shown with their usual FITS binary table column names as they are widely used to label images, spectra and other data:

- detector, DEID or CHANNEL (0=SW‖1=LW)
- entrance wheel position, EWHL (or ENTW)
- Fabry-mirror beam selection wheel position, SWHL (or SELW)
- pixel size lens wheel position, PFOV (or LNSW)
- wavelength and bandwidth defined by the filter wheel position (if applicable), FCVF (or FLTW)
- wavelength interval and scanning step for a CVF scan (if applicable), ‖FCVF‖
- integration time, TINT
- gain, GAIN

where ‖FCVF‖ means a constant set of multiple FCVF values. The parameters EWHL, SWHL, PFOV and FCVF refer to the position of the selection wheel in question and may be translated into quantities of physical significance, such as wavelength or angular resolution, using the CWHEELS calibration file. It is mostly on the basis of these values that data should be divided up and combined for the production of images. There are other especially important real-time quantities which the user should take into account:

ITK : each record of raw data is labelled with an 'Instrument Time Key' in CIER[1].GPSCTKEY(*) or CISP[1].GPSCTKEY(*), for example, to allow synchronisation with the UTK and UTC keys that apply to other types of data.

RPID : the 'Raster-Point ID' is the index of the instrument's pointing direction and is the other quantity in the General Science Prefix in CIER[1].GPSCRPID(*,2), CISP[1].GPSCRPID(*,2). It identifies the relevant parts of the prime or parallel pointing files by comparison with IRPH[1].RPID(*,2) or CIPH[1].RPID(*,2), for example. For pointing operations which did not involve rasters of several different directions, RPID=(1,1). Occasionally, RPID=(0,0) shows that there were pointing problems.

OTF : the 'On-Target Flag' is ON=1 or OFF=0 to show if the instrument is pointing to the target in a direction closer than the angular threshold, usually $10''$, given in CIER[0].ATTOTFTH, IRPH[1].OTFT(*) or CRPH[1].OTFT(*). It serves to show when the manoeuvre to the target is almost complete or the move away has begun, as well as warning observers of rare failures when, for example, it proved impossible to acquire the target at all. Although more detailed pointing information is available if required, the OTF provides a convenient mechanism for rejecting data. The flag is maintained by the on-board pointing system and is available at its fully sampled rate of 2 Hz in IIPH[1].OTF(*) or CIPH[1].OTF(*). The latest value when an F2 block was assembled is given in CIER[1].F2OTFLAG(*) while CIER[1].F2OTFSUM(*) contains the logical AND of all the OTFs sampled during the F2 accumulation time.

QLF : the 'Quick-Look Flag' CIER[1].F2QLA switches from OFF=0 to ON=1 to show that the preselected number of stabilisation EXPOSUREs, N_{stab}, has been completed. This is supposed to ensure that the instrument had settled down after the move to the observation's target. Despite these good intentions, the instrument's transient behaviour proved to be one of its more challenging aspects of which N_{stab} provides only a zeroth-order approximation. A much better stabilisation model, which takes into account the evolution of individual pixel signals, has been implemented in the pipeline as described in Section 4.4.2.1.

5.3 ISOCAM Data Products

The set of ISOCAM data products associated with an observation can be categorised, depending on how they are derived or used, as one of the following:

– **low level**: raw ISOCAM data;

– **calibration files**: containing the instrument model;

– **intermediate level**: complementary data used during the pipeline;

– **high level**: measurements in physical units of images or point sources.

They contain information about the status of the instrument; the status of the telescope; the pointing history; and, last but not least, the scientific data. Their root names begin with the letter 'C' for CAM while the rest of the name serves as a mnemonic of the contents. A complete list of ISOCAM data products is shown in Table 5.2. In addition to the discussion of the early stages of the pipeline below, details of the instrument model and of the high and intermediate level products can be found in the dedicated Chapters 6 and 7, respectively.

5.3.1 Considerations on ISOCAM's use of FITS files

ISOCAM's raw data files are simply binary tables of chronologically ordered rows of records in which each column contains some piece of imaging or housekeeping data. It is usually the job of the analysis software to read in such data sequentially and incorporate them into more coherent astronomical structures with other data in memory or files. For higher level files, wherever possible, products have been designed to conform to the conventions described in the FITS User's Guide, particularly where images are concerned. This also applies to calibration files. The OLP system worked under the constraint of producing only one file of a given type per observation, no matter how many different images were taken. The standard FITS mechanism for delivering single images uses the PRIMARY array and a conventional set of keywords to define the coordinate system, wavelength and other associated data. In order to put several images into one CMAP or CMOS file these PRIMARY array data structures were reproduced in the columns of the binary table in a series of three consecutive records labelled FLUX, FLUX_ERROR and EXPOSURE for an individual image. Despite these efforts, it has been brought to attention that some FITS readers are not able to deal with a standard image format in this modified context although any deficiencies have an easy workaround. In other products containing physical units, such as lists of detected point sources or their spectra, for which there were no common standards when the design was taking place, we adopted as many standard column names as possible to make the structures easily intelligible. Occasionally, NULL values were needed in some binary tables and their appearance in ISOCAM products does not always conform to FITS standards because of platform dependencies that it was not possible to avoid. The most important NULL values, those that appear regularly in images such as the LW channels dead column 24, do conform via the standard use of scaled integers to represent pixel flux and other values. Any NULL integers could similarly be handled through their associated TNULL keywords. The platform-dependent problems arose due to a lack of support for IEEE NaN (not-a-number) conventions. Instead, the user will encounter the value $-1.2\text{E}{-34}$ to show NULLs in, for example, the columns CCIM[1].RA(*), CCIM[1].DEC(*) and CCIM[1].ROLL(*) for those detector images and instrument modes in which the sky was not observed.

5.3.2 Common keywords

In addition to mandatory FITS keywords, all ISOCAM products contain a small number of common PRIMARY keywords describing the production system, most of them self-explanatory. The VERSn keywords show the files used to derive the product.

High level products in physical units and ISO-centric celestial coordinates	
CMAP	CAM images
CMOS	CAM MOSaic
CPSL	CAM Point Source List
CSSP	CAM Source SPectra
CUFF	CAM User-Friendly log File
Intermediate level products in detector units	
CCIM	CAM Calibration IMages
CGLL	CAM GLitch List
CJAM	CAM Jitter, Memory and Stabilisation information
Low level raw data	
CSTA	CAM Compact Status
CIER	CAM Edited Raw Data
CDER	CAM Diagnostic Raw Data
CISP	CAM Standard Processed Data
CPER	CAM Parallel Edited Raw Data
CPSP	CAM Parallel Standard Processed Data
Calibration files	
CCGLWDEAD	CAM LW Dead Pixel Map
CCGLWDARK	CAM LW Dark Current Exposures
CCGLWDFLT	CAM LW Detector Flat-Field Library
CCGLWOFLT	CAM LW Optical Flat-Field Library
CCGLWDMOD	CAM LW Time dependent dark current model parameters
CCGLWSPEC	CAM LW Filter & CVF spectral data
CCGLWPSF	CAM LW Point Spread Function Library
CCGLWTRANS	CAM LW Fouks-Schubert transient model coeffients
CCGLWRESET	CAM LW RESET value statistics
CCGLWSAT	CAM LW Saturation thresholds
CCGLWLOSS	CAM LW Sensitivity loss parameters
CLWCVF1	CAM LW CVF1 description
CLWCVF2	CAM LW CVF2 description
CCGSWDEAD	CAM SW Dead Pixel Map
CCGSWDARK	CAM SW Dark Current Exposures
CCGSWDFLT	CAM SW Detector Flat-Field Library
CCGSWOFLT	CAM SW Optical Flat-Field Library
CCGSWSPEC	CAM SW Filter & CVF spectral data
CCGSWPSF	CAM SW Point Spread Function Library
CCGSWSAT	CAM SW Saturation thresholds
CSWCVF	CAM SW CVF description
CSCGCROSS	CAM SW Cross-talk correlation matrices
CHCGCONV	CAM Housekeeping conversion factors
CWHEELS	CAM Wheel Information Table

Table 5.2: The ISOCAM data products.

For example:

```
ORIGIN  = 'ESA     '           / Not from central ESA archive
TELESCOP= 'ISO     '           / Infrared Space Observatory
INSTRUME= 'CAM     '           / Instrument used
COMMENT   CAM Image Edited Raw Data
FILENAME= 'CIER12900907'       / File name
DATE    = '2001-07-02'         / Creation date 2001/183
FILEVERS= '2523    '           / Version ID (derived from creation date)
OLPVERS = 'OLP_95  '           / SOC OLP system version
CALGVERS= 'CALG_65 '           / SOC OLP CAL-G files version
USERNAME= 'APOLLOCK'           / Product not catalogued
VERS1   = '2155/EOHA129'       / Version ID of each input file
VERS2   = '2155/EOHI129'       / Version ID of each input file
VERS3   = '2318/APPH129'       / Version ID of each input file
```

5.4 TDF_First_Scan and Derive_ERD Products

ISOCAM collected data on a continuous basis and passed it to the OBDH for insertion into the 8192-byte telemetry buffers that were downloaded every 2 s and assembled into one TDF per revolution. When ISOCAM was designated prime instrument, its data were downloaded through 24 of the 32 frames; otherwise, when parallel, through only 1 frame. Pointing data occupied 4 frames and housekeeping data the rest.

`TDF_First_Scan` scans an entire TDF to divide the revolution into individual observations and deliver their scheduling information via the Executed Observation History (EOH) files. Of relevance to ISOCAM are the EOHA and EOHC files from which data are extracted later in the pipeline and inserted into raw-data product header records so that the files themselves do not always need to be used. The EOHC file was a relatively late addition to the pipeline with the main purpose to ensure continuous data coverage. The EOHA observation schedule contains gaps between the nominal end of one observation and the start of the next. ISOCAM's continuous operation meant that potentially useful data sometimes fell in those gaps. Such data did not form part of an observer's TDT but were of help in reconstructing the history of the illumination of individual detector pixels when modelling instrument transients. The EOHC file, where the 'C' stands for *continuous*, was devised to plug those gaps and make all ISOCAM data available and was used in later stages of the ISOCAM pipeline to define observation boundaries.

`Derive_ERD` is run once per observation using, in ISOCAM's case, the EOHC file to define the relevant parts of the TDF from which to extract, expand and record prime CIER or parallel CPER edited raw data and CDER diagnostic raw data. The on-board system interleaves two types of ISOCAM data into telemetry, namely housekeeping F1 blocks and imaging F2 blocks. Whenever the OBDH recognised that an F2 block was ready at the end or beginning of an integration time, it was inserted into telemetry which otherwise contains a continuous series of F1 blocks. Other instrument-independent parts of telemetry are processed simultaneously to transfer raw pointing data from the 4 relevant frames into the AOCS file and general housekeeping data into the GEHK file. At the end of the TDF, the AOCS file is used during derivation of pointing files.

5.4.1 Compact Status products: CCSH & CSTA

For ISOCAM, it is the function of `TDF_First_Scan` to enumerate the instrument changes that took place over the course of a revolution in the CCSH file. As mentioned above, the CCSH primary header contains ISOCAM clock calibration keywords. The 20 or so parameters that define the operational status of ISOCAM are known collectively as the *compact status* and are given in chronological order in the CCSH file along with the start and end UTC, UTK and UTC time keys of the periods in which they apply. Individual observation's compact status values appear later in the CSTA file. For the CVF scans which are used for the spectrophotometric CAM04 AOT, only a single, nominal filter wheel position is stored in CCSH[1].CCSHFLTW(*) and CSTA[1].CSTAFLTW(*), instead of the full set employed.

5.4.2 Raw data primary header keywords

The PRIMARY headers of CIER, CPER, CDER, CISP and CPSP files contain a common set of keywords derived from various sources to give important descriptive data, as in the following example:

```
OBJECT   = 'CB195/L701'         / Target ID as given by proposer
OBSERVER= 'DCLEMENS'            / Proposer ID in ISO Mission DB
EQUINOX =               2000.0 / Equinox
TMRATE  =                   32 / Telemetry rate in Kbps (Kbits/sec)
EOHAUTCS= '96085090612'        / Approx. UTC of start of observation
EOHAUTCE= '96085092918'        / Approx. UTC of end of observation
EOHAAOTN= 'C01     '           / AOT name
EOHAPLID= 'STARLESS'           / Proposal ID
EOHAOSN = '07      '           / Observation sequence number
EOHAPSN = '00      '           / Pointing sequence number
EOHAPCAT= '4       '           / Proposal category
EOHACIND= '        '           / Calibration indicator
EOHATTYP= '002     '           / Target type
AOTVERS = '03.01   '           / AOT-to-OCT logic version
ATTUTCSL= '96085090534'        / UTC of start time of slew to intended target
ATTUTCS = '96085090550'        / UTC of time of first arrival at intended target
ATTOTFTH=                 10.0 / On-target flag threshold (arcsecs)
ATTRA   =            293.69733 / Intended Right Ascension of instrument viewing
ATTDEC  =             12.34669 / Intended DEClination (with ATTRA)
ATTTYPE = 'R       '           / Type of attitude operation (P/R/T)
ATTRNPTS=                    5 / Number of points per line of the raster
ATTRNLNS=                    5 / Number of lines in whole raster pointing
ATTRDPTS=                   32 / Distance (arcsecs) between adjacent points
ATTRDLNS=                   32 / Distance (arcsecs) between adjacent lines
ATTRORIE=                    1 / ORIENTation flag (0 or 1)
ATTRROTA=                  0.0 / ROTATE of raster pattern (degrees)
ATTGUIDE=               109046 / Guide star reference number
ATTSAANG=                 71.0 / Solar aspect angle (degrees)
ATTERROR=                    2 / CONTINGEncy flag(0=success; 1=target not acq'd)
TREFCOR1=            228128772 / UTC of 1st reference time
TREFPHA1=            129.47567 / Orbital phase at TREFCOR1
TREFCOR2=            228129465 / UTC of 2nd reference time
TREFPHA2=            129.48371 / Orbital phase at TREFCOR2
TREFCOR3=            228130158 / UTC of 3rd reference time
TREFPHA3=            129.49175 / Orbital phase at TREFCOR3
TREFUTC1=            228128772 / UTC (whole seconds since 01-01-1989)
TREFUTC2=              5112273 / UTC (remaining fraction of second)
TREFUTK =            301458521 / ISO Uniform Time Key (UTK)
TREFITK =             89720116 / ISO INSTRUMENT Time Key (ITK)
TREFITKU=     0.13999950000000 / ITK unit length in seconds
```

Of those keywords that are not obviously self-explanatory, the EOHA data are from the EOHA record that applies to the observation; the ATT data are pointing-related quantities from the first relevant APPH record; and the TREF data give the clock calibration or are calculated at times near the beginning, middle and end of the observation to show progress through the spacecraft's orbit.

5.4.3 Edited Raw Data products: CIER or CPER & CDER

`Derive_ERD` makes one CIER or CPER row for every F2 block found in telemetry, expanding the compacted format into bytes, words or longwords and adding supplementary housekeeping data from an adjacent F1 block. Similarly, each of the larger number of F1 blocks is used to make one CDER row, without imaging data, thus providing a complete history of the instrument's housekeeping. The F1 contents of the CDER record are identical to the F1 part of CIER or CPER records and comprise data for 244 different housekeeping parameters, including those in vector columns related to a wide variety of quantities such as settings of the internal calibrator source or the cryo motor; temperature measurements at different detector locations; on-board processor status and error codes; and voltage settings. Most of these data are of limited general interest. The rest of the CIER or CPER records are occupied by raw imaging data in CIER[1].F2IMAG(1122,*), for example, and 33 other associated F2 block items. The dimensions of F2IMAG are greater than $32 \times 32 = 1024$ in order to accommodate extra data required by the SW readout scheme. Unless on-board integration was in operation, records alternate between RESET and EOI data with identical CAM on-board times CIER[1].F2TIME(*) and CIER[1].F2BOOTTI(*) that are used to calculate the CAM ITK in CIER[1].GPSCTKEY(*).

5.4.4 Pointing History products: IRPH or CRPH & IIPH or CIPH

Pointing data are obviously vital for data analysis and these are calculated at the end of `Derive_ERD` using the AOCS file derived earlier at the same time as other raw data. Two files are produced, namely a Reference Pointing History file and an Instantaneous Pointing History file. When ISOCAM was prime, the IRPH and IIPH files contained CAM pointing data. Otherwise, CAM parallel pointing data are found in the CRPH and CIPH files. The pointing system operated independently of any other instrument, so these files are of a general design described in the ISO Handbook Volume I, [40]. Because parallel pointing files were only made for CAM parallel's benefit, it is worth pointing out here, though, the extra CRPH[1].PRIME(*) and CIPH[1].PRIME(*) columns that show the aperture of the prime instrument in use. A change in the PRIME aperture implies a change in the spacecraft's and ISOCAM's pointing direction requiring a new data boundary. The other significant pointing event for both prime and parallel data is a change of RPID. The expected time of changes of IRPH[1].RPID(2,*) are given in IRPH[1].UTC(2,*) and IRPH[1].UTK(*), for example, which may be compared with the actual times by inspection of IIPH.RPID(2,*), IIPH.UTC(2,*) and IIPH.UTK(*).

5.5 `Derive_SPD` Products

`Derive_SPD` performs a number of intermediate tasks on ERD in order to prepare an observation's data for the scientific analysis performed by `AAC` in the pipeline. In conjunction with the pointing files, SPD is also the recommended starting point for other analysis systems, including CIA, as it contains all the ISOCAM information necessary for most astronomical requirements.

5.5.1 Standard Processed Data: CISP or CPSP

`Derive_SPD` makes one CISP or CPSP row for every pair of EOI and RESET CIER or CPER records, unless subtraction was already performed on board. The imaging data are accompanied by RESET data, where available; 15 columns of image-description data, such as the various wheel settings; 3 types of image statistics; and the most important temperature, bias-voltage and blackbody housekeeping data. Given the importance of the CAM SPD, the contents of the CISP[1].TABLE are shown in Table 5.5.1.

Table 5.3: Columns of the CISP[1].TABLE

column	type	description
GPSCTKEY	1J	Instrument time key
GPSCRPID	2B	Raster point ID
CISPBOOT	1J	Time since processor's boot [CAMTU]
CISPDEID	1B	Detector ID (SW:0, LW:1)
CISPCNFG	1B	Configuration number within AOT
CISPQFLG	1B	CAM's QLA flag: F2_QLA + 2× OTFLAG + 4× OTFSUM
CISPPROC	1B	PROCessing mode 0:Normal, 1:Accumulated, 2:Sampled
CISPDISC	1I	CSH/ERD 'Discrepancy Flags'
CISPPFOV	1I	Lens wheel step number
CISPITIM	1I	Elementary integration time (CAMTU)
CISPFCVF	1I	Filter wheel step number
CISPWAVE	1E	Filter or CVF central wavelength
CISPEWHL	1I	Entrance wheel step number
CISPSWHL	1I	Selection wheel step number
CISPWDTH	1I	Filter/CVF width in millimicrons
CISPOBST	1B	Current op-mode 1:OBS, 2:DRK, 3:CAL, 4:CLN, 0:IDLE
CISPCVFS	1B	CVF scan on/off (1/0)
CISPTEMP	10E	CAM temperatures [K]
CISPBLKB	2E	Black body current & voltage
CISPGAIN	1B	Electronics gain (0, 1, 2)
CISPOFFS	1B	Electronics offset (0...3)
CISPBSFG	1I	Beams flag: 256×C+R; C:cycle, R:ref#, Add 16 on Ref#
CISPMEAN	1E	Frame mean of CISPDATA (this - last)
CISPMEDI	1E	Frame median of CISPDATA (this)
CISPSRMS	1E	Frame rms of CISPDATA (this - last)
CISPICNT	1I	Current internal image counter
CISPACSA	1B	ACcumulated/SAmpled image register
CISPAOBS	1B	F2_AOT_AOT + 16× F2_AOT_OBS
CISPBIAS	10E	Bias voltages
CISPDATA	1024I	Detector data (EOI−RESET)
CISPRESE	1122I	RESET level for NORMAL processing
CISP3334	64I	Columns 33 & 34 of SW readout

The CISPDISC discrepancy flags have bits set to show any differences between the record's optical configuration as defined by its instrument settings and the commanded values from the Compact Status that sometimes occur because of the time it takes for the wheels to move. While it is possible to interrogate individual bits, the recommendation to use only data with CISPDISC=0 is followed by the pipeline. Similarly, CISPQFLG=7 shows a record with QLA, OTF and OTFSUM flags all set although the user may choose to ignore the zeroth order QLA stabilisation flag during transient modelling.

It is, of course, necessary to use appropriate calibration data during analysis dependent on the instrument configuration which often changes during the course of an observation. These instrument changes are reflected in a set of CISP[1].HEADER keywords including some that were originally designed to give recommendations of which calibration data should be used. However, the proper calibration selection scheme is more complicated than allowed by the CISP[1].HEADER scheme and users should ignore them and follow instead the advices provided in Chapter 6.

Chapter 6

ISOCAM Calibration Files

6.1 The ISOCAM Instrument Model

Both ground-based and in-flight measurements contributed to the encapsulation of the instrument model in a set of calibration files (CAL-G) required for analysis of ISOCAM data. The *CAM Calibration Explanatory Document* (Altieri et al. 1998, [2]) describes the limited time available for calibration measurements during the mission and how this was used. The data here presented form part of the general CAL-G releases for all instruments that were made from time to time, usually coincident with OLP software releases. CAL-G files were used by the pipeline to produce archive material including, in particular, the highest-level products, which include measurements in physical units of images or point sources.

ISOCAM CAL-G filenames usually start with 'CCGLW' or 'CCGSW' and the appropriate detector except the few that have kept historical names designated long ago. The set of operational files is shown in Table 6.1 along with a list of obsolete files. The early design of the ISOCAM pipeline made room for files that ultimately were never implemented. Users may come across dummy versions which should be ignored.

Files conform to the same simple FITS scheme used for all products, as described in Chapter 5, of either a single HDU=0 PRIMARY image (empty except for the dead-pixel maps) and associated header or a single HDU=1 BINARY-TABLE extension. Within the overall CAL-G release, as given by the HEADER[0] CALGVERS keyword in pipeline data products, ISOCAM maintained its own calibration version, known as CCD for CAM Calibration Data. CCGLWSPEC[0].CALIBRAT, for example, shows in which CCD release the file appeared. Extensive use is made of the standard FITS multidimensional array-coding mechanisms up to NAXIS=3 often within rows of TABLE[1] when many different calibration components are contained within a single file. For example, the CAL-G Version 7.0 release of CCGLWPSF[1].TABLE contained 121 different normalised point source images.

Most calibration components, such as dark images, flat-field corrections and point spread functions, depend on instrumental configuration as specified by accompanying TABLE[1] parameters of which usually a small subset are significant for selecting the correct component to use — provision was made in the files to accommodate variations with temperature and voltage settings although these proved redundant and the corresponding columns are filled with zero values which are also to be ignored. Dark exposures, for example, are labelled with several parameters showing how they were derived, although the only significant one for selection purposes is the integration time, although scaling for the instrumental gain is also required. It was not possible to give all calibration components for all possible configurations, though straightforward procedures are available for how to choose the most suitable data in the absence of a perfect match as described below. Each of the calibration files is described in the following subsections showing the parameters on which the selection depends in the form 'component=ccg_component(p1,p2,...)' where the parameter order p1,p2,... is significant in the absence of a perfect match.

Operational Calibration Files	
CCGLWDEAD	CAM LW Dead Pixel Map
CCGLWDARK	CAM LW Dark Current Exposures
CCGLWDFLT	CAM LW Detector Flat-Field Library
CCGLWOFLT	CAM LW Optical Flat-Field Library
CCGLWDMOD	CAM LW Time dependent dark current model parameters
CCGLWSPEC	CAM LW Filter & CVF spectral data
CCGLWPSF	CAM LW Point Spread Function Library
CCGLWTRANS	CAM LW Fouks-Schubert transient model coeffients
CCGLWRESET	CAM LW RESET value statistics
CCGLWSAT	CAM LW Saturation thresholds
CCGLWLOSS	CAM LW Sensitivity loss parameters
CLWCVF1	CAM LW CVF1 description
CLWCVF2	CAM LW CVF2 description
CCGSWDEAD	CAM SW Dead Pixel Map
CCGSWDARK	CAM SW Dark Current Exposures
CCGSWDFLT	CAM SW Detector Flat-Field Library
CCGSWOFLT	CAM SW Optical Flat-Field Library
CCGSWSPEC	CAM SW Filter & CVF spectral data
CCGSWPSF	CAM SW Point Spread Function Library
CCGSWSAT	CAM SW Saturation thresholds
CSWCVF	CAM SW CVF description
CSCGCROSS	CAM SW Cross-talk correlation matrices
CHCGCONV	CAM Housekeeping conversion factors
CWHEELS	CAM Wheel Information Table
Obsolete Calibration Files	
CCGLWSLP	CAM LW CVF spectral line profile
CCGLWLINEAR	CAM LW linearity correction
CCGLWFRAME	CAM LW detector astrometric corrections
CCGLWGLITCH	CAM LW glitch model
CCGLWSTRAY	CAM LW straylight model
CCGSWSLP	CAM SW CVF spectral line profile
CCGSWLINEAR	CAM SW linearity correction
CCGSWFRAME	CAM SW detector astrometric corrections
CCGSWGLITCH	CAM SW glitch model
CCGSWSTRAY	CAM SW straylight model
CCGSWTRANS	CAM SW transient model

6.1.1 CCGLWDEAD & CCGSWDEAD – ISOCAM dead pixel maps

dead=ccg_dead(deid)

There are PRIMARY 32×32 images for each detector showing LIVE=0 or DEAD=1 pixels. No new pixels died during the mission so that these files remained unchanged. The LW detector's column 24 was dead. The SW detector had 4 dead pixels.

6.1.2 CCGLWDARK & CCGSWDARK – ISOCAM dark current exposures

dark=ccg_dark(deid,tint,gain)

One of the most important calibration components is the signal detected in the absence of any illumination called the 'dark current'. The files contain libraries of dark-current exposures (AXIS3=1) and errors (AXIS3=2) in units of ADU/G/s for GAIN=1 dependent on TINT only, accurate to about 0.3 and 0.5 ADU/G/s for the LW and SW detectors, respectively. Conversion to units of ADU/s for the detector GAIN is necessary using the correction factor g = 2^{GAIN}.

6.1.3 CCGLWDMOD – ISOCAM LW dark current model

dmod=ccg_dmod(deid,tint,gain,rev,tsa)

Analysis of the evolution of the LW dark current (Section 4.2.2) showed there were systematic drifts both over the course of the mission and during individual revolutions (Biviano et al. 1998a , [5]; 2000, [9]; Román & Ott 1999, [50]). The drift is linear over the mission and quadratic over the revolution. For revolution number R, and time since activation in seconds T (since the instrument was switched on at the beginning of the revolution), the dark current in pixel (y, z) is given by:

$$dmod_{yz} = (ir_{yz} + sr_{yz}R) + (io_{yz} + so_{yz}T + po_{yz}T^2)\ \text{[ADU/s]}$$

The coefficients $ir_{yz}, sr_{yz}, io_{yz}, so_{yz}, po_{yz}$ are given in CCGLWDMOD for the 5 values of TINT at GAIN=0 rather than at GAIN=1, used in CCGLWDARK. These models give the best knowledge of the dark current and should be used in preference to the static data of CCGLWDARK.

6.1.4 CCGLWDFLT & CCGSWDFLT – ISOCAM detector flat-field library

dflt=ccg_dflt(deid,ewhl,fcvf,swhl,tint)

For practical reasons, the overall flat-field correction was decomposed into the product of detector and optical flat-fields (see Section 4.5). Both flat-field components were estimated by exploiting the uniform illumination of the detector provided by the zodiacal light except for those optical configurations, including the SW channel in particular, where it was not bright enough. In such cases the Internal Calibration Device (ICD) was used instead despite the presence of significant residual spatial structure. For details of these procedures, see the *ISOCAM Flat-field Calibration Report* (Biviano et al. 1998c, [7]).

Under the further assumption that the optical flat-field at the highest $1.5''$ resolution is identically unity, the detector flat-field was determined from these highest resolution observations. After deglitching, dark correction and stabilisation, exposures were scaled to a median of unity in the central 12×12 pixel area to generate the detector flat-fields available in CCGLWDFLT and CCGSWDFLT, which have an accuracy of better than 1% as discussed in the *ISOCAM Calibration Error Budget Report* (Biviano et al. 1998d, [8]). The DFLT data are probably the CAL-G files in which the optical configuration parameter space was least satisfactorily explored.

6.1.5 CCGLWOFLT & CCGSWOFLT – ISOCAM optical flat-field library

oflt=ccg_oflt(deid,pfov,ewhl,fcvf,swhl,tint)

Uniform illuminated observations at resolutions other than 1.5″ in conjunction with the detector flat-fields discussed above were used to derive the optical flat-fields reported in CCGLWOFLT and CCGSWOFLT, which include those identically unity at 1.5″.

6.1.6 CCGLWSPEC & CCGSWSPEC – ISOCAM filter and CVF spectral data

spec=ccg_spec(deid,fcvf,ewhl)

After dark and flat-field corrections have been performed in detector units, it is necessary to convert to physical units in order to draw physical conclusions. Observations of calibration standard stars whose fluxes were already known or which had reliable models were made in a variety of optical configurations to derive the information stored in CCGLWSPEC and CCGSWSPEC, where the photometric relationship between detector units (ADU/G/s) and astronomical flux units (Jy) is most clearly encapsulated in the SENSITIV parameter in units of (ADU/G/s) / Jy. Values of SENSITIV are also given for polarisation measurements, as distinguished from normal open aperture measurements by the appropriate values of EWHL, in a number of relevant filters.

Although a detailed report on the approach and methods of the ISOCAM photometric programme is available elsewhere (Blommaert 1998, [10]; Blommaert et al. 2000, [11]) it is worth describing here briefly how these important data were derived. After the normal glitch, dark and flat-field corrections, well-stabilised data of the calibration image were background subtracted and the strength of the source in detector units of ADU/G/s was derived using a circular aperture before the application of a further correction factor calculated from the relevant point spread function to compensate for flux loss outside the aperture. The corresponding flux density for the broad-band filters was integrated over the relevant transmission curve assuming a $\lambda F_\lambda(\lambda) = constant$ spectral shape while for the relatively narrow band-width CVF scans, no integration was performed and the known spectrum was used directly. The ratio of these two quantities gives the SENSITIV parameter. For details concerning the CVF spectral response function see the *ISOCAM CVF Calibration Report* (Biviano et al. 1998b, [6]) and the *ISOCAM CVF Photometry Report* (Blommaert et al. 2001a, [12]). The spectral transmission curve, $R(\lambda) = T(\lambda) \times Q(\lambda)$, was also derived from ground-based measurements, where $T(\lambda)$ is the filter transmission and $Q(\lambda)$ is the detector quantum efficiency (see Appendix A). Comparison of observed flux and model spectrum requires application of Equation A.1.

6.1.7 CCGLWSAT & CCGSWSAT – ISOCAM saturation thresholds

sat=ccg_sat(deid,gain,proc)

Very bright sources occasionally exceeded the dynamic range of the ISOCAM detectors, saturating one or more pixels and rendering physical flux estimates highly unreliable. CCGLWSAT and CCGSWSAT report the GAIN- and PROC-dependent saturation thresholds against which EOI pixel values in individual exposures should always be checked, as they are as a matter of course in `AAC`.

6.1.8 CCGLWRESET – ISOCAM LW detector RESET value statistics

reset=ccg_reset(deid,rev)

In order to be able to check for pixel saturation those on-board processing modes for which only (EOI−RESET) values are available in telemetry rather than individual EOI and RESET values, it is useful to be able to interrogate the RESET statistics tabulated in CCGLWRESET against revolution number for all the spacecraft orbits in which any CAM data were taken.

6.1.9 CCGLWPSF & CCGSWPSF – ISOCAM point spread functions

psf=ccg_psf(deid,pfov,fcvf,ewhl,swhl,tint)

CCGLWPSF and CCGSWPSF contain sets of normalised point source images that serve as point spread functions (PSFs) as measured at different optical configurations and detector locations specified in (y,z)=(TABLE[1].CRPIX1, TABLE[1].CRPIX2) (see Section 4.6.1 or Okumura 1998, [44]). The PSFs are intended for the usual purposes of source detection, as in `AAC`, and aperture photometry corrections.

6.1.10 CCGLWTRANS – ISOCAM LW FS transient model coefficients

trans=ccg_trans(deid)

CCGLWTRANS contains 32×32 tables of λ and β coefficients (See Section 4.4.2.1 or Coulais & Abergel 2000, [21]) for each pixel used in the Fouks-Schubert transient correction model applied during `AAC` on LW data.

6.1.11 CCGLWPOL – ISOCAM polarisation weight factors

pol=ccg_pol(deid,ewhl)

CCGLWPOL reports the orientation angles of the 3 polarisers in the entrance wheel.

6.1.12 CSCGCROSS – ISOCAM SW cross-talk correlation matrices

SW detector data require noise and capactive cross-talk corrections using coefficients held in CSCGCROSS in conjuction with the auxiliary SW columns 33 and 34. In the ISOCAM pipeline, these corrections are made during `Derive_SPD`, so that users who follow the recommendation to use SPD as the starting point for their analysis should make no use of this file. Otherwise, advice and code are available from the ISO Data Centre.

6.1.13 CHCGCONV – ISOCAM housekeeping conversion factors

CHCGCONV contains tabulations of physical units against coded digital reference values of 31 named housekeeping parameters for the interpolation of the values found in telemetry. Linear schemes defined by two points apply to 22 parameters; 2 parameters have 6-point schemes; 1 parameter has an 8-point scheme; and 6 parameters have 16-point schemes. In the ISOCAM pipeline, the conversion from digital to physical units is performed during `Derive_SPD`, so that users who follow the recommendation to use SPD as the starting point for their analysis should make no use of these data.

6.1.14 CWHEELS – ISOCAM wheel information table

ISOCAM's optical path is defined by the settings of 4 of 6 wheels. CWHEELS uses the WHLNB index to relate the motor step number used almost exclusively to label imaging data of the:

EWHL WHNLB=1 entrance wheel

SWHL WHNLB=2 selection wheel

PFOV WHNLB=3 LW lens wheel

FCVF WHNLB=4 LW filter wheel

PFOV WHNLB=5 SW lens wheel

FCVF WHNLB=6 SW filter wheel

with descriptive names widely used among observers of the optical element in the path such as 'HOLE', 'LW10', etc. For the filter wheels, values of central wavelength and filter bandwidth are specified which may have become obsolete. Instead, it is recommended to use the rigorously maintained data in CCGLWSPEC and CCGSWSPEC.

6.1.15 CLWCVF1 & CLWCVF2 – ISOCAM LW CVF descriptions

CLWCVF1 and CLWCVF2 give wavelength in microns and sensitivity and error in (ADU/G/s) / Jy for the LW detector as a function of wheel position, known here as MOTOSTEP instead of the more common FCVF, of the two CVF segments of the LW filter wheel. These data among others have also been incorporated into CCGLWSPEC.

6.1.16 CSWCVF – ISOCAM SW CVF description

CSWCVF gives wavelength in microns and sensitivity and error in (ADU/G/s) / Jy for the SW detector as a function of the CVF wheel position, also known here as MOTOSTEP instead of the more common FCVF. These data among others have also been incorporated into CCGSWSPEC.

6.2 Notes on the Use of the Calibration Files

It should be clear from the discussions above how, in principle, the different types of calibration data should be used in the analysis of ISOCAM data. The ubiquitous dark current and flat-field corrections are governed by a simple equation for the cosmic flux in detector units:

$$sky(y,z) = (obs(y,z) - dark(y,z))/flat(y,z) \tag{6.1}$$

where $flat(y,z) = dflt(y,z) \times oflt(y,z)$. While it is often possible to extract calibration components that match exactly the optical configuration of an observation, even in these ideal circumstances the so-called lens wheel jitter can compromise to some extent the accuracy of the data by causing edge effects.

When the CAL-G files do not contain components that match exactly the configuration of an observer's data, the question arises of the best alternative that should be chosen. In the discussion above the references of type 'component=ccg_component(p1,p2,...)' show the significant parameters for each calibration component. `AAC` has implemented a scheme in which alternatives are assessed on the basis of their distance in selection parameter space from the exact match. An OLP FORTRAN code fragment is given in Appendix D which shows the applied selection rules.

Chapter 7

ISOCAM Auto-Analysis

7.1 AAC's General Approach

AAC is the stage of the pipeline in which most of the work is done to generate products in physical units. As expected with an automatic procedure with no intervention possible on behalf of the observer, the final results may not be as good as those possible with an interactive system like CIA, for example. Experience has shown, however, that the pipeline products archived in IDA are of consistently high enough quality to offer a good overall assessment of the scientific merit of the data and enable the observer to make an initial astronomical interpretation using the set of up to 8 different data products provided. The tasks performed by AAC may be summarised as follows, showing the data products ($\Longrightarrow$) in which the results appear:

- AAC operates on a single prime or parallel observation;
- data are assembled into coherent units in memory;
- static pointing and ideal calibration references are added;
- cosmic-ray glitches are detected and flagged $\Longrightarrow$CGLL;
- the amplitude of spacecraft pointing jitter is assessed $\Longrightarrow$CJAM;
- Fouks-Schubert transient model correction is applied;
- detectors are checked for incomplete illumination;
- attention is drawn to any saturation problems;
- images are calculated in detector coordinates for all data $\Longrightarrow$CCIM;
- sky images are calculated in celestial coordinates $\Longrightarrow$CMAP;
- sky mosaics are calculated in celestial coordinates $\Longrightarrow$CMOS;
- point sources are detected $\Longrightarrow$CPSL;
- source spectra are calculated $\Longrightarrow$CSSP;
- archive summary data are generated;
- comments are made on each stage of the analysis $\Longrightarrow$CUFF.

AAC's raw ingredients are the revolution's EOHA and EOHC; and CISP SPD and IRPH & IIPH pointing files for prime data or CPSP SPD and CRPH & CIPH pointing files for parallel data; and the set of CAL-G files. The pipeline was designed to offer images and point source measurements in formats as close to standard FITS as possible. Individual calibrated images are reported, for example, in the CMAP file in which, as explained above, FITS PRIMARY image conventions are reproduced in the columns of TABLE[1] over 3 consecutive rows for FLUX, FLUX_ERROR and EXPOSURE. These occur often and are referred to below as CCIM or CMAP or CMOS 3-row images. If more than one part of the sky was observed, such as in a raster or in the beam-switch observing mode, individual CMAP images are combined in the CMOS. Similarly, if a detected point source was observed but not necessarily detected at more than one wavelength, individual CPSL fluxes are combined for the spectra in the CSSP.

AAC's work from beginning to end is reported in the CUFF, or CAM User-Friendly log File, which prints details of the procedures executed and summaries of the results obtained. One of its useful jobs is to show which calibration components were used in the analysis, especially when the exact instrumental configuration was unavailable. The following example CUFF extract shows that, while an optical flat-field of the same optical configuration was available, the nearest detector flat-field in selection parameter space had to be used.

```
Extraction of components from CAL-G files
LW Dflt       EWHL    FCVF    SWHL    PFOV    TINT
Tried:         308     140      88     360      15
Got:           308     125     220     192      36
LW Oflt       PFOV    EWHL    FCVF    SWHL    TINT
Tried:         360     308     140      88      15
Got:           360     308     140      88      15
```

7.1.1 The use of SCDs within AAC

Data are divided into the longest coherent units during which the configurations of satellite and instrument were constant, incorporating pointing and calibration data. These units are known as Standard Calibrated Data, or 'SCDs', and the user will find frequent references to them in the CUFF and other data products. The SCD boundaries are decided empirically, by a process that has become known as 'slicing', on the basis of a change in any of the following 14 parameters:

OBST	operating mode
CNFG	configuration counter
DEID	LW or SW detector
EWHL	aperture entrance wheel setting
SWHL	mirror selection wheel setting
PFOV	pixel size lens wheel setting
FCVF	waveband filter wheel setting
GAIN	detector gain
PROC	on-board processing mode
ACSA	number of accumulated or sampled images
BSFG	beam-switch flag
ITIM	integration time
RPID	raster-point ID
IID	prime instrument aperture

all but the last two of which are from the SPD record. The RPID and IID are taken from the pointing files. As the instrument operated continuously, passing an uninterrupted stream of EOI and RESET frames into telemetry, SCDs are of types OBS, DRK, CAL, CLN or IDLE depending on the operating mode.

A number of SCDs form the configurations, or 'CNFs', which in turn form the AOT that encapsulates the entire observation. Each of `AAC`'s tasks of calibration or data reduction takes place by manipulation of SCDs either individually or in the groups forming the CNFs or the AOT as appropriate. SCDs are designated 16-character names `CSCDnnnnnnnnccii`, where `nnnnnnnn` is the 8-digit observation number, `cc` the 2-digit configuration number and `ii` is a 2-character alphanumerical index. These SCD names are to be found, for example, in CCIM[1].DATAREF(*) and are regularly mentioned in the CUFF.

The assembly of SCD structures marks the end of the frame-by-frame character of ERD and SPD that reflects their operational function with the recognition of the astronomical context and scientific coherence of the data. For example, each SCD has a pointing direction - that remains undefined for DRK, CAL, CLN or IDLE SCDs; images that are stored in explicit 2-D 32×32 structures; and a set of references showing which calibration components should ideally be used in analysis. Every pixel readout has associated an observed value, a mask and a model value, reflecting the non-destructive approach to data analysis adopted by `AAC`. The mask is used to signal various conditions that might be detected during the course of analysis, such as that the pixel was dead or had been affected by a cosmic-ray glitch, and serves as the basis for the inclusion of individual pixels in calculations or data products. The model value is used to store the reconstructed value from the application of Fouks-Schubert transient modelling.

7.2 Instrumental Procedures and Data Products ⟹CCIM

Once the SCD data structures have been established a series of instrumental procedures is applied to ensure the reliability and integrity of the imaging data. Each step is discussed below. Many of them have the effect of causing a bit to set in the SCD pixel mask that ensures exclusion of the datum from photometric calculations of any type of which the CMAP is the most important. More generally within SCDs, data are also excluded while the instrument is under adjustment as shown by non-zero values of the CISP[1].CISPDISC flags that show a configuration other than that commanded. Occasional SCDs have all their data excluded as reported in the CUFF:

```
No useful data in CSCD3610030101AX
No useful data in CSCD3610030101AY
```

Inspection of the raw images reported in the CCIM file gives some idea of the importance of these steps. There are 3-row RATE, RATE_ERR and EXPOSURE images in CCIM.TABLE[1] for every SCD of whatever type, accompanied by a full set of auxiliary data describing the circumstances in which the data were taken. The CCIM images are raw in the sense that they include all the SCD's data irrespective of imperfections of any type, like glitches, dead pixels, badly illumination or defects of any other type. For each CCIM 3-row image, the CUFF reports a short summary such as:

```
LW(OBS)  1996-11-11(14:20:43) to 1996-11-11(14:21:40) CSCD361003010107
RA(J2000)=20 21 48.007 : DEC(J2000)=+39 57 00.67 : ROLL(J2000)=249.20
14.0-15.8 micron @ 6" per pixel
CCIM(22:24) 27 planes
<RATE>=9.6ADU/s  <RATE_ERR>=0.1ADU/s  <EXPOSURE>=56.7s
CGLL 192 glitches
CJAM maximum jitter [-21.5:+0.1,-8.2:+0.2] pixels
```

including details of entries made in some of the products discussed below.

7.2.1 Deglitching ⟹CGLL

It is clear from the most cursory glance at CCIM images that glitches are an unwelcome but common feature of many image readouts as discussed above in Section 4.3. The 'Multi-resolution Median Transform' method (see Appendix E) is applied to detect and flag these events on the entire observation's history of each pixel. A few thousand glitches are regularly detected in observations and reported in the CGLL, whose main purpose is to provide a cross-check against any unusual features that might be discovered in the data. Besides the time, detector coordinates and strength of the glitches, CGLL[1].INDEX(*) refers to the CCIM images in which they were detected. For those glitches detected during regular observations of the sky, the corresponding pixel celestial coordinates are reported in CGLL[1].(RA(*),DEC(*)). Zero rather than proper NULL values fill these columns for glitches detected in operational modes other than OBS. The CGLL was also originally designed to accommodate glitch model parameters but no such modelling was ever performed and the COUNTG(*), YG(*), ZG(*) and UTKG(*) columns contain only nominal or null values.

7.2.2 Use of pointing data $\Longrightarrow$CJAM

Detailed use is made of the IRPH and IIPH pointing files for prime data or the CRPH and CIPH for parallel data. First, the CUFF reports any pointing condition that applies to the observation as a whole, such as:

```
No up-to-date QSS/STR misalignment measurement: IRPH12900907
```

after which the RPH file is used to provide the reference celestial coordinates for each SCD using a combination of RPID and time-key. These data are later used to define the reference coordinates attached to the images and thus determine ISOCAM's astrometry.

It is obviously important to take account of data taken only when the instrument was looking in the right direction. A crude assessment is provided by the OTF which shows that the pointing was within a threshold distance, usually $10''$, of the target position and data are indeed excluded if the OTF is low. However, the OTF threshold is usually equivalent to several pixels and more detailed information is available in the Pointing History files which are in any case, the ultimate source of the SPD OTF. The instantaneous pointing data reported in the IIPH or CIPH, including the RPID and OTF, have a time resolution of 0.5 s that is finer than SPD and thus enable more complete checks. Experience has shown that during a raster the OTF sometimes briefly remains high immediately after a change in the RPID has signalled a move to a new position. If `AAC` detects a condition of this type in an SCD the high OTF is overruled as reported in the CUFF:

```
Overruling the first high QLA(OTF) at RPID=[2,1]
```

Similarly, if a move has apparently started during a single ISOCAM integration but the CAM OTF is still high, it is also overruled with the report:

```
Overruling OTF when final RPID <> [3,1]
```

The mean instantaneous direction during each integration is used to calculate the offset from the current reference direction otherwise known as the *pointing jitter*. The jitter could have been used to realign the individual exposures contributing to an image but because of some confusion early in the mission about the reliability of the pointing data the corrections were disabled and never reinstated. The jitter components in pixel units parallel to the detector axes are reported in CJAM[1].DY and CJAM[1].DZ for each integration. Inspection shows that the satellite's pointing system was evidently very stable with the jitter amplitude usually only a fraction of a pixel. These are the most useful CJAM data. The CJAM[1] MEMORY, UNSTABLE and GLITCHED columns are obsolete.

7.2.3 Illumination masking ⟹CUFF

For some optical configurations, the field mirror did not entirely cover the detector causing the appearance of prominent linear features roughly parallel to the edges of the detector, whose positions can vary. Badly illuminated rows and columns of this type are masked out and reported in the CUFF with messages such as:

```
780902864<UTK<781068887 Badly illuminated columns [1] [2]
```

7.2.4 Saturation masking ⟹CUFF

Observers should also be aware that very bright sources can saturate the detector, rendering the photometry dangerously unreliable. In this unfortunate event, prominent messages in the CUFF should draw the observer's attention as in these disjointed fragments which both show the extra CCIM information and anticipate the CMAP and CPSL discussion below:

```
+--------+---------+---------+--------+--------+---------+---------+--------+
CWRN                Saturation problems detected
 ******** ********* ********* ******** ******** ********* ********* ********
 Of the data collected during this observation 193 pixel readout values
 were marked as saturated, so that flux measurements should be treated
  with caution. Shown below are
    - the saturated pixel count for those CCIM images affected;
    - the label 'saturated [LW] image' for those CMAP images affected;
    - the label 'saturated' for those CPSL point sources affected.
 ******** ********* ********* ******** ******** ********* ********* ********
+--------+---------+---------+--------+--------+---------+---------+--------+

LW(OBS)  1997-06-14(11:12:16) to 1997-06-14(11:14:14) CSCD576007010150
RA(J2000)=17 53 36.572 : DEC(J2000)=+56 51 56.89 : ROLL(J2000)=5.18
11.6-17.0 micron @ 6" per pixel
CCIM(154:156) 105 planes
<RATE>=-2.2ADU/s  <RATE_ERR>=0.1ADU/s  <EXPOSURE>=117.6s
CGLL 532 glitches
88 saturated pixels
CJAM maximum jitter [-0.1:+3.5,-0.1:+0.1] pixels

CMAP(142:144) 1997-06-14(11:12:16) to 1997-06-14(11:14:14)
RA(J2000)=17 53 36.572 : DEC(J2000)=+56 51 56.89 : ROLL(J2000)=5.18
11.6-17.0 micron saturated LW RPID=[7,6] image of [32*32] [6"] pixels
<FLUX>=0.53mJy/arcsec^2  <FLUX_ERR>=0.12mJy/arcsec^2  <EXPOSURE>=113.7s
CCIM(OBS:DRK:FLT)=(154:0:0)

CPSL(58) 1997-06-14(11:12:16) to 1997-06-14(11:14:14)
11.6-17.0 micron
ISOC175332.0+565219 17 53 32.043 +56 52 19.3   8413.2 +/- 42.1  mJy saturated
```

7.2.5 Transient modelling

One of the significant improvements introduced towards the end of OLP software development was the ability to account for the transient behaviour of the LW detector following a change in the illumination as discussed in Section 4.4. It takes a long time for the detector to settle down after a large change in incident flux. In earlier versions a very rough check on the stabilisation was provided by the QLA flag which was raised after a pre-programmed fixed number of exposures had elapsed. Now, by application of the Fouks-Schubert model, individual pixel data are calculated according to the model and stored in SCDs, providing estimates of what those pixel data would have measured in the absence of such non-linearities. The CUFF reports a few details of the calculations.

```
FS:Using transient corrector Fouks-Shubert v2.0
FS:++ Depth data cube :      3310 planes
FS:++ Pixels corrected:   3389440
FS:-- Using Taylor    :   3170187
FS:-- Using Mueller   :    218229
FS:$$ Mueller failed  :         0
```

These models provide, therefore, a much better stabilised alternative to the raw pixel values and the pipeline makes use of them in calculating all of its highest-level scientific data products.

7.3 High-Level Scientific Data Products

Once data have been assembled, poor quality parts traced, transient models calculated and ideal calibration components identified, it is possible to calculate and analyse fluxes in photometric units. The most important data products are the images calculated for every OBS-mode SCD that are given in the CMAP file. The other products are based on further analysis of CMAP images. The products contain cross references to be able to trace the path of the analysis, CMAP[1].OBSINDEX(*) to CCIM ; CMOS[1].MAPINDEX(*) to CMAP; CPSL[1].MAPINDEX(*) to CMAP; and CSSP[1].PSLINDEX(*,*) to CPSL.

7.3.1 ISOCAM basic imaging $\Longrightarrow$CMAP

The flux maps in physical units given in CMAP 3-row FLUX, FLUX_ERR, EXPOSURE images for each OBS-mode SCD are calculated from all good-quality transient-corrected data available with the reference (J2000) celestial coordinates of the SCD, which were taken from the IRPH for prime or CRPH for parallel data, with no corrections made for pointing jitter. After dark-current and detector and optical flat-field corrections have been applied in detector units using the best calibration components available as reported in the CUFF:

```
LW Drkm       TINT
Tried:          15
Got:            15
LW Dflt       EWHL    FCVF    SWHL    PFOV    TINT
Tried:         308     140      88     360      15
Got:           308     125     220     192      36
LW Oflt       PFOV    EWHL    FCVF    SWHL    TINT
Tried:         360     308     140      88      15
Got:           360     308     140      88      15
```

conversion to Jansky units is made using the appropriate sensitivity factor from CCGLWSPEC or CCGSWSPEC:

```
LW Spec       FCVF    EWHL
Tried:         140     308
Got:           140     308
```

The FLUX_ERR errors are calculated by a quadratic combination of the variance of the data within the SCD with errors in the calibration data. The usual non-uniformity of the EXPOSURE images is mainly because of the randomness of the impact of glitches. Each image is labelled with several auxiliary data, many of which conform to FITS conventions such as CMAP[1].MJD-OBS(*) and CMAP[1].MJD-END(*). Others specify wavelength and bandwidth, for example. Finally, a summary of each CMAP 3-row image is reported in the CUFF:

```
CMAP(181:183) 1996-11-11(15:13:01) to 1996-11-11(15:13:56)
RA(J2000)=20 22 24.033 : DEC(J2000)=+40 31 31.08 : ROLL(J2000)=249.30
14.0-15.8 micron LW RPID=[20,4] image of [32*32] [6"] pixels
<FLUX>=0.58mJy/arcsec^2  <FLUX_ERR>=0.31mJy/arcsec^2  <EXPOSURE>=45.5s
CCIM(OBS:DRK:FLT)=(190:0:0)
```

7.3.2 ISOCAM combination imaging $\Longrightarrow$CMOS

There were 3 ways in which CMAP images could be combined to give the more complex 3-row images in the CMOS, which is produced if, and only if, more than one direction was observed in a fixed optical configuration, namely raster pointing mode observations; beam-switch observations; and solar system tracking observations.

7.3.2.1 Raster pointing mode observations

The most usual was the compensation for the restricted ISOCAM field of view offered by the pointing system's raster capability in which a rectangular array of celestial coordinates were surveyed at a fixed instrumental configuration allowing the component images to be combined into a single mosaic of larger extent. The raster orientation and 2-D step sizes were at the observer's discretion with no guarantee that the component maps were conveniently aligned. In some cases, observers chose raster step sizes that were small enough for there to be a good deal of redundancy in overlapping areas of sky with the intention of minimising any systematic errors due to transient effects or calibration uncertainties. Rasters with very small step sizes less than a few pixels were often known as microscans although their treatment did not differ from other rasters in `AAC`, ignoring the ambitions of some users who may have have had super-resolution in mind. The reference coordinate frame of the 3-row CMOS images is arbitrary and `AAC`'s choice was to use a direction as near as possible to the centre of the raster that optimised the alignment between the component maps, whose pixel size was preserved. Finally, the pixels of the resultant mosaic were calculated from a weighted average of contributing component pixels, taking any misaligment into account using the area of overlap. In some CAM parallel rasters performed therefore for the benefit of observers using other instrument, the raster steps size were bigger than the component CMAP images which did not overlap at all, causing only partial coverage of the resultant CMOS that is criss-crossed with stripes of undefined flux. Not unexpectedly, rasters of this type were the largest of all, reaching 1500×1500 pixels. A summary of each raster's CMOS 3-row image is reported in the CUFF:

```
CMOS(1:3)     1996-11-11(14:13:39) to 1996-11-11(16:08:57)
RA(J2000)=20 22 18.000 : DEC(J2000)=+40 09 40.01 : ROLL(J2000)=249.28
```

```
14.0-15.8 micron LW image of [480*296] [6"] pixels
<FLUX>=0.82mJy/arcsec^2  <FLUX_ERR>=0.15mJy/arcsec^2  <EXPOSURE>=72.8s
```

7.3.2.2 Beam-switch observations

In a simulation of traditional IR observational methods, there was a special CAM03 AOT designed for beam-switch in which component images of a fixed designated source field were interleaved with images of one or more reference offset fields which were supposed to provide a reliable background estimate. The combination image written to the CMOS in this case is the difference between the source and a background estimate. During the mission it was soon discovered that it would make sense to swap the order of source and reference images although it did not prove possible to alter some of the on-board software accordingly, so that the attached beam-switch labels are the wrong way round. AAC makes an effort to identify this condition by trapping negative fluxes in the combination image, in which case suitable action is taken and reported thus in the CUFF:

```
Reversing source and reference positions
```

The beam-switch configuration, the component CMAPs and the resultant CMOS 3-row images are reported in the CUFF as in the following example extracts which shows an observation with 4 sequences with <4> background fields at two wavelengths. The first CMOS has the badly illuminated column [1] trimmed from the final image.

```
T=5315s C03 4*<4> beam-switch observation of N4038_BS_4REF
RA(J2000)=12 01 53.781 : DEC(J2000)=-18 52 42.51 : ROLL(J2000)=118.03

146370023<UTK<146426926 Badly illuminated column [1]

CMAP(1:3)   5.1-8.3 micron LW On<1> image of [32*32] [6"] pixels
CMAP(4:6)   5.1-8.3 micron LW Off<1> image of [32*32] [6"] pixels
CMAP(7:9)   5.1-8.3 micron LW On<2> image of [32*32] [6"] pixels
CMAP(10:12) 5.1-8.3 micron LW Off<2> image of [32*32] [6"] pixels
CMAP(13:15) 5.1-8.3 micron LW On<3> image of [32*32] [6"] pixels
CMAP(16:18) 5.1-8.3 micron LW Off<3> image of [32*32] [6"] pixels
CMAP(19:21) 5.1-8.3 micron LW On<4> image of [32*32] [6"] pixels
CMAP(22:24) 5.1-8.3 micron LW Off<4> image of [32*32] [6"] pixels
CMAP(25:27) 5.1-8.3 micron LW On<1> image of [32*32] [6"] pixels
CMAP(28:30) 5.1-8.3 micron LW Off<1> image of [32*32] [6"] pixels
CMAP(31:33) 5.1-8.3 micron LW On<2> image of [32*32] [6"] pixels
CMAP(34:36) 5.1-8.3 micron LW Off<2> image of [32*32] [6"] pixels
CMAP(37:39) 5.1-8.3 micron LW On<3> image of [32*32] [6"] pixels
CMAP(40:42) 5.1-8.3 micron LW Off<3> image of [32*32] [6"] pixels
CMAP(43:45) 5.1-8.3 micron LW On<4> image of [32*32] [6"] pixels
CMAP(46:48) 5.1-8.3 micron LW Off<4> image of [32*32] [6"] pixels

CMAP(49:51) 5.1-8.3 micron LW On<1> image of [32*32] [6"] pixels
CMAP(52:54) 5.1-8.3 micron LW Off<1> image of [32*32] [6"] pixels
CMAP(55:57) 5.1-8.3 micron LW On<2> image of [32*32] [6"] pixels
CMAP(58:60) 5.1-8.3 micron LW Off<2> image of [32*32] [6"] pixels
CMAP(61:63) 5.1-8.3 micron LW On<3> image of [32*32] [6"] pixels
CMAP(64:66) 5.1-8.3 micron LW Off<3> image of [32*32] [6"] pixels
```

```
CMAP(67:69) 5.1-8.3 micron LW On<4> image of [32*32] [6"] pixels
CMAP(70:72) 5.1-8.3 micron LW Off<4> image of [32*32] [6"] pixels
CMAP(73:75) 5.1-8.3 micron LW On<1> image of [32*32] [6"] pixels
CMAP(76:78) 5.1-8.3 micron LW Off<1> image of [32*32] [6"] pixels
CMAP(79:81) 5.1-8.3 micron LW On<2> image of [32*32] [6"] pixels
CMAP(82:84) 5.1-8.3 micron LW Off<2> image of [32*32] [6"] pixels
CMAP(85:87) 5.1-8.3 micron LW On<3> image of [32*32] [6"] pixels
CMAP(88:90) 5.1-8.3 micron LW Off<3> image of [32*32] [6"] pixels
CMAP(91:93) 5.1-8.3 micron LW On<4> image of [32*32] [6"] pixels
CMAP(94:96) 5.1-8.3 micron LW Off<4> image of [32*32] [6"] pixels

CMAP(97:99)   11.6-17.0 micron LW On<1> image of [32*32] [6"] pixels
CMAP(100:102) 11.6-17.0 micron LW Off<1> image of [32*32] [6"] pixels
CMAP(103:105) 11.6-17.0 micron LW On<2> image of [32*32] [6"] pixels
CMAP(106:108) 11.6-17.0 micron LW Off<2> image of [32*32] [6"] pixels
CMAP(109:111) 11.6-17.0 micron LW On<3> image of [32*32] [6"] pixels
CMAP(112:114) 11.6-17.0 micron LW Off<3> image of [32*32] [6"] pixels
CMAP(115:117) 11.6-17.0 micron LW On<4> image of [32*32] [6"] pixels
CMAP(118:120) 11.6-17.0 micron LW Off<4> image of [32*32] [6"] pixels
CMAP(121:123) 11.6-17.0 micron LW On<1> image of [32*32] [6"] pixels
CMAP(124:126) 11.6-17.0 micron LW Off<1> image of [32*32] [6"] pixels
CMAP(127:129) 11.6-17.0 micron LW On<2> image of [32*32] [6"] pixels
CMAP(130:132) 11.6-17.0 micron LW Off<2> image of [32*32] [6"] pixels
CMAP(133:135) 11.6-17.0 micron LW On<3> image of [32*32] [6"] pixels
CMAP(136:138) 11.6-17.0 micron LW Off<3> image of [32*32] [6"] pixels
CMAP(139:141) 11.6-17.0 micron LW On<4> image of [32*32] [6"] pixels
CMAP(142:144) 11.6-17.0 micron LW Off<4> image of [32*32] [6"] pixels

CMAP(145:147) 11.6-17.0 micron LW On<1> image of [32*32] [6"] pixels
CMAP(148:150) 11.6-17.0 micron LW Off<1> image of [32*32] [6"] pixels
CMAP(151:153) 11.6-17.0 micron LW On<2> image of [32*32] [6"] pixels
CMAP(154:156) 11.6-17.0 micron LW Off<2> image of [32*32] [6"] pixels
CMAP(157:159) 11.6-17.0 micron LW On<3> image of [32*32] [6"] pixels
CMAP(160:162) 11.6-17.0 micron LW Off<3> image of [32*32] [6"] pixels
CMAP(163:165) 11.6-17.0 micron LW On<4> image of [32*32] [6"] pixels
CMAP(166:168) 11.6-17.0 micron LW Off<4> image of [32*32] [6"] pixels
CMAP(169:171) 11.6-17.0 micron LW On<1> image of [32*32] [6"] pixels
CMAP(172:174) 11.6-17.0 micron LW Off<1> image of [32*32] [6"] pixels
CMAP(175:177) 11.6-17.0 micron LW On<2> image of [32*32] [6"] pixels
CMAP(178:180) 11.6-17.0 micron LW Off<2> image of [32*32] [6"] pixels
CMAP(181:183) 11.6-17.0 micron LW On<3> image of [32*32] [6"] pixels
CMAP(184:186) 11.6-17.0 micron LW Off<3> image of [32*32] [6"] pixels
CMAP(187:189) 11.6-17.0 micron LW On<4> image of [32*32] [6"] pixels
CMAP(190:192) 11.6-17.0 micron LW Off<4> image of [32*32] [6"] pixels

+---------+---------+---------+--------+--------+---------+---------+--------+

CMOS(1:3)     1996-01-10(14:05:49) to 1996-01-10(14:45:20)
RA(J2000)=12 01 53.781 : DEC(J2000)=-18 52 42.52 : ROLL(J2000)=118.04
5.1-8.3 micron LW image of [31*32] [6"] pixels
<FLUX>=0.05mJy/arcsec^2  <FLUX_ERR>=0.02mJy/arcsec^2  <EXPOSURE>=365.0s
```

```
CMOS(4:6)     1996-01-10(14:47:35) to 1996-01-10(15:27:06)
RA(J2000)=12 01 53.782 : DEC(J2000)=-18 52 42.52 : ROLL(J2000)=118.05
11.6-17.0 micron LW image of [32*32] [6"] pixels
<FLUX>=0.07mJy/arcsec^2  <FLUX_ERR>=0.11mJy/arcsec^2  <EXPOSURE>=361.2s
```

7.3.2.3 Solar system tracking observations

A modified pointing system raster mode allowed the tracking of fast-moving objects such as comets and asteroids. Using a known ephemeris, the object's path across the sky was simulated in a series of short duration 1-D raster steps designed to keep the object at fixed detector coordinates. AAC calculates the series of CMAPs as usual, labelled with changing celestial coordinates and then combines them into a single resultant CMOS 3-row image in detector coordinates. In the following example, 4 component CMAP 3-row images starting at RPID=[6,1] make the final 32×43 CMOS which is labelled with nominal celestial coordinates as opposed to a more rigorous object-centred system.

```
T=456s C01 tracking observation of 214015 WILSON-HA
RA(J2000)=00 46 47.583 : DEC(J2000)=+06 31 16.19 : ROLL(J2000)=246.40

CMAP(1:3) 1997-01-28(14:51:08) to 1997-01-28(14:51:58)
RA(J2000)=00 46 47.651 : DEC(J2000)=+06 31 16.59 : ROLL(J2000)=246.40
8.6-15.4 micron LW RPID=[6,1] image of [32*32] [1.5"] pixels
<FLUX>=1.67mJy/arcsec^2  <FLUX_ERR>=0.12mJy/arcsec^2  <EXPOSURE>=29.3s

CMAP(4:6) 1997-01-28(14:51:58) to 1997-01-28(14:52:38)
RA(J2000)=00 46 47.787 : DEC(J2000)=+06 31 17.38 : ROLL(J2000)=246.40
8.6-15.4 micron LW RPID=[7,1] image of [32*32] [1.5"] pixels
<FLUX>=1.66mJy/arcsec^2  <FLUX_ERR>=0.11mJy/arcsec^2  <EXPOSURE>=29.8s

CMAP(7:9) 1997-01-28(14:52:38) to 1997-01-28(14:53:29)
RA(J2000)=00 46 47.922 : DEC(J2000)=+06 31 18.17 : ROLL(J2000)=246.40
8.6-15.4 micron LW RPID=[8,1] image of [32*32] [1.5"] pixels
<FLUX>=1.66mJy/arcsec^2  <FLUX_ERR>=0.11mJy/arcsec^2  <EXPOSURE>=39.5s


CMAP(10:12) 1997-01-28(14:53:29) to 1997-01-28(14:54:09)
RA(J2000)=00 46 48.058 : DEC(J2000)=+06 31 18.95 : ROLL(J2000)=246.40
8.6-15.4 micron LW RPID=[9,1] image of [32*32] [1.5"] pixels
<FLUX>=1.67mJy/arcsec^2  <FLUX_ERR>=0.12mJy/arcsec^2  <EXPOSURE>=29.1s

+--------+---------+---------+--------+--------+---------+---------+--------+

CMOS(1:3)     1997-01-28(14:51:08) to 1997-01-28(14:54:09)
RA(J2000)=00 46 47.583 : DEC(J2000)=+06 31 16.19 : ROLL(J2000)=246.40
8.6-15.4 micron LW image of [32*32] [1.5"] pixels
<FLUX>=1.66mJy/arcsec^2  <FLUX_ERR>=0.06mJy/arcsec^2  <EXPOSURE>=127.6s
```

7.3.3 The CMAP point source survey $\Longrightarrow$CPSL

A search is made through all the CMAP images for point sources. The simple method employed detects sources by modelling the observed spatial flux distribution in appropriately sized detection cells using maximum likelihood statistics. The models combine the best-available source PSFs, as reported in the CUFF, and a flat background. The shape of the PSF generally also depends on source position as well as on the instrumental configuration. Knowledge of the noise is vital because an underestimate would lead to the detection of many spurious sources while an overestimate causes weak sources to be missed. `AAC` adopts an empirical approach by creating an equivalent counts map in which the amplitude of the Poisson noise matches the observed variance of the data. Candidates are first identified assuming a single point source at the centre of pixels after which the models become more sophisticated. As many sources as required are included for a successful fit with all the parameters adjusted simultaneously. The best-fit source positions are chosen by considering the sub-pixel PSF resolution available in the CCGLWPSF and CCGSWPSF files. After final consistency checks, parameters of the detected sources are exported to the CPSL and summarized in the CUFF.

7.3.4 Point source spectra $\Longrightarrow$CSSP

If, and only if, observations were made at more than one wavelength, the CPSL point sources are rearranged in order to create the CSSP, which contains the flux spectra of the various objects detected which are cross-identified by their celestial coordinates. If an object was not detected at a particular wavelength the corresponding flux is assigned the conventional NULL value while a mean value is calculated for multiple detections.

7.4 Browse Products

From the standard pipeline a number of files are also generated to provide users with:

- Survey Products:
  These products are the equivalent of the automatic analysis system, giving the image from the CMOS file when it exists and CMAP otherwise. In IDA they can be viewed directly with the Survey Product Display Tool (SPDT). Although these products contain fully reduced data, it must be emphasized that the processing is done in a standard and automatic way which does not involve any scientific judgement.

- Icons and Postcards
  Icons and postcards facilitate a quick-look to scan the data for particular purposes and identify which data need to be retrieved. For ISOCAM, the postcard is the image in GIF format of the survey product projected in (RA, DEC) coordinates. It contains a grey-scale coded wedge to indicate flux levels. The icon is a small version of the CMAP/CMOS image shown in detector coordinates. For the CAM spectral observations (CAM04) the mean image of all wavelengths is displayed; the spectrum shown is that of the innermost 10×10 pixels. Up to four multi-filter or multi-pfov measurements (for a given observation) are shown inside the corresponding icon.

Chapter 8

Caveats

As described in previous chapters, the ISO OLP pipeline produced a variety of files that are available through the ISO Data Archive. While the use of FITS format implies a high-level of self-documentation regarding the quality of the data reduction and problems encountered during the automated processing performed, the user should be aware that there are some remaining caveats that should be considered for a proper data analysis. Some of them may require a detailed interactive analysis with the help of the available software (CIA, see the *ISOCAM Interactive Analysis User's Manual*, [28]). These caveats have been collected together in this chapter, and are presented in roughly the same product order in which they appear during the analysis scheme illustrated in Figure 5.1. Following some general considerations which apply in common to all ISOCAM data products, caveats affecting only some individual products are also discussed.

8.1 ISOCAM Astrometry

Under the worst circumstances, ISOCAM's coordinate accuracy is given by $3\times pfov+3''$, although typical measurements are much better than that, as reported in Section 4.11, for example. The overall error is decomposed as follows:

- Repositioning accuracy of the lens and filter wheels. The penalty is flat-fielding and minor coordinate errors typically less than 2 pixels.
- There is a small displacement of the ISOCAM optical axis in some filters and CVF positions, leading to coordinate errors of up to one pixel.
- Optical distortion, leading to celestial position and flux errors at off-axis positions.
- Very infrequent ISO pointing-system errors.

No corrections are made for any of these effects in the OLP.

8.2 General Considerations

- Auto-Analysis uses only time-independent flat-field corrections as available in the CAL-G libraries, leading to the possibility of less accurate fluxes compared with those calculated using optimised flat-field corrections as currently done within CIA. The likely outcome is poor flux calibration at the edges of the field of view.

- Auto-Analysis uses the Fouks-Schubert method to correct for transient effects. The method is applied only to LW data, excluding CAM parallel observations. The algorithm is necessarily applied automatically, and adopts as reference the quiescent level at the beginning of the observations when individual inspection could have identified some more appropriate value. In some extreme cases this can lead to completely wrong predictions of the corrected data. Note also that the current algorithm breaks down for point-like sources and is thus regularly disabled in small areas nearby, although in some circumstances contaminated fluxes or spurious hot spots have appeared.
- A changing CVF effective wavelength away from the optical centre leads to wavelength errors as big as the equivalent of one CVF step.
- Observations performed near the extremes of the CVF ranges, namely outside the range recommended in the ISOCAM Observer's Manual, are less accurately calibrated.
- Auto-Analysis makes no straylight or ghost corrections leading to the possibility of flux errors and the detection of spurious sources.
- Flux errors reported, for example, in the CPSL are only statistical and take no account of any systematic effects.
- Non-linearity of the detectors is not taken into account. This affects in particular the SW detector when a very bright point source was observed.

8.3 CSTA Files

The keyword CSTAREAD indicates *the number of readouts* and is not to be confused with *the number of frames.* The number of frames is identical to the number of readouts only for on-board processing mode. Otherwise, there are twice as many readouts as frames as both EOI and RESET readouts are needed to compute a single frame.

8.4 IIPH Files

Beware of occasional bumps in the IIPH during stable pointing that have been traced to the effects of cosmic-ray glitches in the star tracker's CCD. Recognition of events of this type may be helped by the fact that large apparent excursions in the pointing direction are not accompanied by the OTF going down.

8.5 CMAP Files

- CMAPs are constructed using the reference celestial coordinates from the IRPH files with no correction for the IIPH pointing jitter which, though small, causes image blur of about $1''$.
- As indicated in Chapter 4, straylight generated ghosts can lead to spurious extended features in images. Ghosts seem mainly to affect CVF data with pixels larger than $1.5''$ (Biviano et al. 1998b, [6]; Okumura et al. 1998, [45]).
- Lens and filter-wheel jitter can lead to imperfect flat-fielding at the edges of CMAPs, where errors up to a factor of 5 may occur.
- In SW observations of a strong source the dark current may be overestimated, which leads to an apparently negative background.

8.6 CMOS Files

Since CMOS are created from CMAPs, the caveats above apply as well as the following:

- In some mosaic images, especially with low backgrounds, a pattern resembling a wire mesh can be seen. This is caused by the bad illumination of the edge column and which is then repeated throughout the mosaic.
- When constructing mosaics from CMAP images, no optical distorsion is taken into account. This may lead to blurred point sources.

8.7 CPSL Files

The flux uncertainties reported in CPSL are statistical only and amount to about $\pm 20\%$ for fixed filters and $\pm 30\%$ for CVFs. Point source analysis is only performed on CMAP images, before any mosaic reconstruction. Hence some faint sources, that become detectable after the mosaic reconstruction, will have escaped detection by the Auto-Analysis routines. Other things to bear in mind:

- Wheel jitter can introduce spurious point sources.
- The point source detection algorithm is prone to find some spurious sources for the SW detector or near complex extended sources.
- Unrecognized glitches may be mistaken as sources.

8.8 CSSP Files

The CSSP gives spectral information for sources in the CPSL, so the caveats there also apply here. Sometimes, due to the astrometry problems discussed above, a single object can be detected at apparently different positions in different filters or CVF positions and give rise to two or more disjoint spectra which, with the benefit of the hindsight missing from the pipeline, could easily be combined into one.

Chapter 9

Getting Started with ISOCAM Data

ISOCAM data can be obtained via `ftp`[1] from the ISO Data Archive (IDA) located at:

`http://www.iso.vilspa.esa.es/` → `Access the Archive`

Detailed information about IDA, its contents and query capabilities can be found in the ISO Handbook Volume I, [40].

A dedicated astronomical software package jointly developed by the ESA Astrophysics Division and the ISOCAM Consortium, and called CIA [CAM Interactive Analysis (see the *ISOCAM Interactive Analysis User's Manual*, [28]], is offered to facilitate data analysis. CIA supports anything from a simple visualisation and quick-look analysis (photometry, spectrometry) of the archive products, to a much more sophisticated manipulation and interactive reduction, starting from the raw data, in order to improve the quality of individual products. CIA is distributed by the ISO Data Centre, and by the ISOCAM Data Centre at Saclay, France, upon request. A form is available for this purpose at:

`http://www.iso.vilspa.esa.es/` → `ISO Data Analysis Software`

9.1 How to Retrieve ISOCAM Data Products

ISOCAM data, as any other ISO data, can be retrieved from the ISO Data Archive (IDA) by establishing an internet connection with the Java-based user interface found at:

`http://www.iso.vilspa.esa.es/` → `Access the Archive`

which allows the user to pursue enquiries in a very flexible and intuitive way. Note, however, that to be able to *retrieve* ISO data, the user has to register first as an IDA user by sending an e-mail to the ISO Helpdesk (`helpdesk@iso.vilspa.esa.es`), or by filling in the form available in IDA, which can be found by clicking first on the button *'Login/Register'* and then on *'Register As New User'*.

All users (even those not registered) can perform queries during an IDA session by filling in the *'Query Specification'* panel, and can submit them by clicking the *'Execute Query'* button. The list of individual observations (TDTs) matching a query will then be displayed together with their associated *'Browse Products'* (see Section 7.4) in the *'Latest Results'* screen.

At this stage, only authorised registered users will be able to proceed further with data retrieval. Once logged-in, the authorised user can move all, or a sub-sample, of the selected observations to the *'Shopping Basket'*. Then, by clicking on the *'Shopping Basket'* button the list of observations selected for data retrieval will be displayed.

[1] Archive products can also be downloaded directly from the *'Latest Results'* screen by clicking on the *'Retrieve'* button after IDA Version 5.2, released in July 2002

Different categories of data products are offered for retrieval, ranging from *'Raw Data'* to *'Fully Processed Data'*, and including some *'Quick Look'* data products derived from the fully processed data.

Users can also customize their requests by selecting the option 'CUSTOM' under the *'Products Desired'* menu in the *'Shopping Basket'* screen and then clicking on the *'Define Custom'* button. The whole variety of data products available will then be displayed in the *'Custom Dataset Definition'* screen, including the option to retrieve the calibration files used in the Off-line Processing Pipeline (OLP).

For a detailed description of the available ISOCAM data products and calibration files the user is referred to Chapters 5, 6 and 7. The selection of the specific files to retrieve will essentially depend on whether the user wants the data in the form of final products, fully processed with the standard pipeline and ready for scientific use (CMAP, CMOS, CPSL, CSSP, CUFF, CCIM, CGLL and CJAM), or as lower level data products (CSTA, CIER, CDER, CISP and the calibration files), which are suitable as the starting point for interactive analysis with CIA.

Once the desired data products are selected and the request submitted, an e-mail is received by the user explaining how to download the products via anonymous `ftp`.

9.2 First Look at ISOCAM Data

As explained in Section 5.3.1, ISOCAM data products were designed to conform as much as possible to FITS standards. They are made up of a primary header plus a binary table extension containing the data. Despite that, some standard software tools for viewing and editing FITS format images, like `fv` (see: `http://heasarc.gsfc.nasa.gov/` → `Software` → `fv` for information on this interactive FITS file editor) or SAOImage DS9 (an astronomical data visualisation application available at `http://tdc-www.harvard.edu/` → `SAOimage`) are not able to read ISOCAM images produced by the OLP. On the other hand, IDL can easily read the OLP product files (with the `mrdfits` command), but an extra modification is needed in order to convert the files from 1024-element arrays to 32×32-element images (using the `reform` command).

As an example, to read a CMAP file:

```
IDL> structure = mrdfits('cmap########.fits',1,header)
IDL> map = reform(structure.array,32,32,n)}
```

where `n` is the third dimension of the cube image (found when executing the `mrdfits` command).

For CMOS:

```
IDL> structure = mrdfits('cmos########.fits',1,header)
IDL> mosaic =
reform(structure.array(*,*,0),structure.naxis1,structure.naxis2)
```

where `structure.naxis1` and `structure.naxis2` are the dimensions (in #pixels) of the mosaic image.

For a user who wants to work directly with fully reduced data, the recommended files to start with are:

- **CMAP**: the ARRAY entry contains the images at different wavelengths or raster positions, calibrated in astronomical flux units and referred to celestial coordinates. Following FITS standards, the images have been recorded using the BZERO and BSCALE keywords, so that: IMAGE=BSCALE*ARRAY+BZERO. The BLANK entry indicates the NaN value for each row (i.e. the pixels with these values have to be ignored when analysing the images). Information about the coordinates, wavelengths, projection parameters, units, etc is also available under different entries. As explained in 7.3.1, the ARRAY entry is composed of 3-row images containing: data (FLUX), errors (FLUX_ERR) and exposure times (EXPOSURE) for each slice.

- **CMOS**: contains a combination of CMAP calibrated images, if observations are composed of several individual pointings (raster or beam-switch observing modes). As in CMAP, the ARRAY tag has to be scaled: MOSAIC=BSCALE*ARRAY+BZERO.
- **CPSL**: if the user is only interested in the photometry of a particular source, the file CPSL lists all the point sources detected in the image, and their associated flux (FLUX tag). Note that the sources are detected at map level (not in the mosaic), so that the same sky source can appear in the table as many times as it is detected in different maps making up the mosaic (e.g. images recorded at different raster positions). The tag MAPINDEX identifies the individual map where the sources are found, and the Y, Z, RA and DEC tags identify their coordinates on the detector and in the sky, respectively.
- **CSSP**: If the image contains data corresponding to more than one wavelength (CVF mode), then the file CSSP groups all the detections stored in CPSL at all wavelengths for each sky target and builds the spectra (FLUX versus WAVELENG tags) of all the point sources detected. The tag PSLINDEX relates each CSSP value (flux of a source at a particular wavelength) with its identification in CPSL (NSRC).

Of course, tools to visualise and analyse scientifically these files are also available in CIA.

Users retrieving the so-called 'browse products' (CPS files) should bear in mind that these products are essentially similar to the CMAP or CMOS (where relevant) files, with the difference that they only store the images in their extensions. The information about the image (coordinates, pfov, etc) is available in the header. However, errors are not stored. In CAM CVF observations a second CPS file contains the wavelengths for each of the planes of the cube image. The main advantage of the browse products is that they can be directly read by FTOOLS (`http://heasarc.gsfc.nasa.gov/` → `Software` → `FTOOLS`), but the recommendation is not to use them for science purposes.

9.3 Interactive Data Processing with CIA

The ESA Astrophysics Division and the ISOCAM consortium developed jointly the CAM Interactive Analysis (CIA) software package. CIA runs under IDL and many routines are available for the processing and scientific analysis of ISOCAM data.

A quick look at what can be done with the help of CIA can be found in the *CIA Quick Reference Card*, available at:

`http://www.iso.vilspa.esa.es/` → `ISO Explanatory Library` → `CAM`

For users interested in interactive processing of ISOCAM data, starting from the raw data products, we recommend the use of CIA after retrieval of the CISP (raw exposure information, no calibration applied) and IIPH (coordinate information) files, from IDA. The CISP is the recommended starting point for CIA based work. If the user is not planning to use CIA then the calibration files (contained in CIA) must also be retrieved. The content of the above-listed files (also conforming to FITS standard) is extensively explained in Chapters 5 and 6 of this volume.

Appendix A

Colour Corrections

The transmission of optics and filters, as well as the quantum efficiencies of the detectors exhibit non-flat spectral dependencies. As a consequence, two sources radiating the same power within a given wavelength range but with different spectral shapes, produce two different signals. The flux density derived from measurements of a source in a given filter has to be corrected for this effect. Therefore the flux density at the reference wavelength of a certain filter of the broad-band photometry of ISOCAM has been computed for an a priori assumed spectral shape, a $F_\lambda(\lambda) \sim \lambda^{-1}$ law. This is the spectral density distribution which has the same shape for $F_\lambda(\lambda)$ and $F_\nu(\nu)$, namely $F_\lambda(\lambda) \sim \lambda^{-1}$ and $F_\nu(\nu) \sim \nu^{-1}$. The same convention was adopted for the flux densities quoted in the IRAS catalogues. Although this is an arbitrary choice, this does not imply any loss of generality, because the 'real' flux density can be recovered by the colour correction described hereafter. In the CCG*WSPEC CAL-G files the spectral transmission curve for each filter is given. The spectral transmission $R(\lambda)$ as defined for ISOCAM is the product of the filter transmission $T(\lambda)$ and the detector quantum efficiency $Q(\lambda)$:

$$R(\lambda) = T(\lambda) \times Q(\lambda)$$

No transmission curve for the lenses has been included. To determine the *actual* flux density one has to divide the flux density (derived after dividing the measured ADU/G/s by the SENSITIV parameter of the CCG*WSPEC CAL-G files) by the colour correction factor $K(\lambda_{\rm ref})$.

$$F_{\rm actual}(\lambda_{\rm ref}) = F_{\rm derived}/K(\lambda_{\rm ref})$$

where $K(\lambda_{\rm ref})$ is given by:

$$K(\lambda_{\rm ref}) = \frac{\int \frac{F_\lambda(\lambda)}{F_\lambda(\lambda_{\rm ref})} \frac{\lambda}{\lambda_{\rm ref}} R(\lambda)\, d\lambda}{\int R(\lambda)\, d\lambda} = \frac{\int \frac{F_\nu(c/\lambda)}{F_\nu(c/\lambda_{\rm ref})} \frac{\lambda_{\rm ref}}{\lambda} R(\lambda)\, d\lambda}{\int R(\lambda)\, d\lambda} \tag{A.1}$$

The spectral transmission $R(\lambda)$ of the SW and LW channels of ISOCAM are shown in Figure A.1 and Figure A.2, respectively. Colour corrections calculated for different blackbody temperatures and for different power-laws ($F_\nu \sim \lambda^{-\alpha}$) are shown in Tables A.1 - A.4.

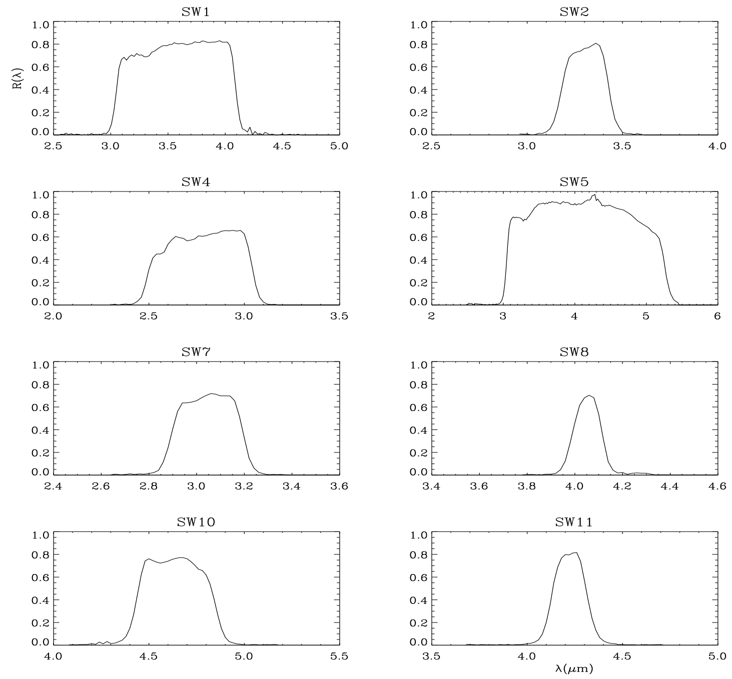

Figure A.1: *Spectral transmission $R(\lambda)$ of the SW channel of ISOCAM.*

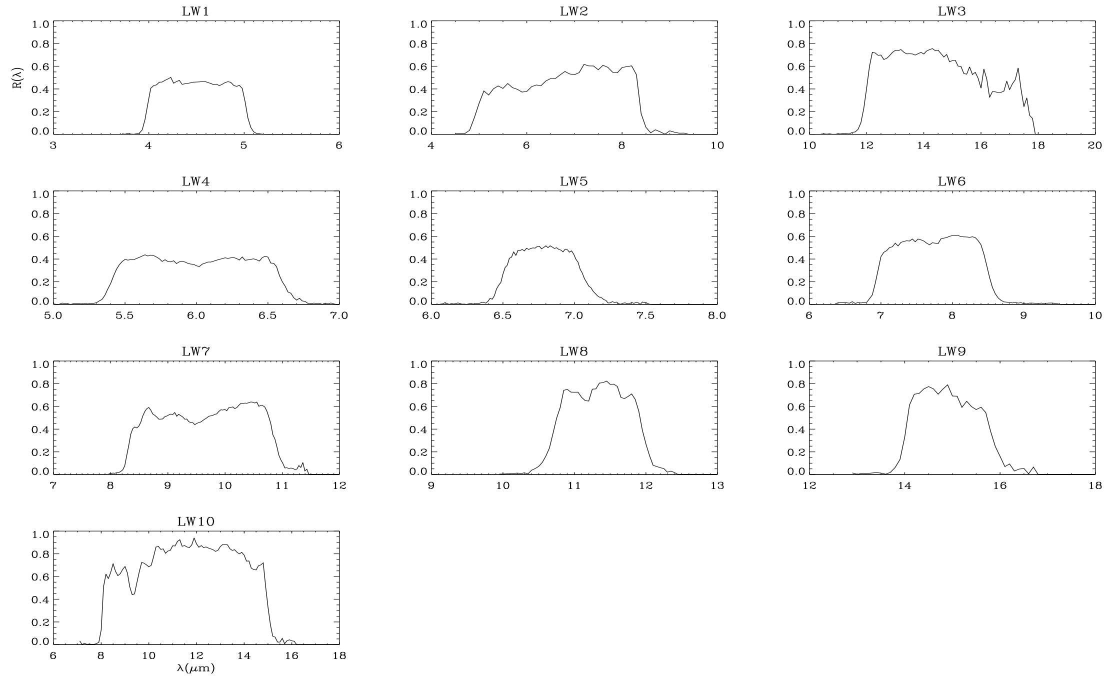

Figure A.2: *Spectral transmission $R(\lambda)$ of the LW channel of ISOCAM.*

Table A.1: *Colour correction values for LW filters for different blackbody temperatures.*

Temp	LW1	LW2	LW3	LW4	LW5	LW6	LW7	LW8	LW9	LW10
10000	1.03	1.08	1.03	1.02	1.01	1.02	1.01	1.00	1.01	1.29
5000	1.02	1.07	1.03	1.02	1.01	1.00	1.01	1.00	1.01	1.27
4000	1.02	1.06	1.02	1.01	1.01	1.00	1.01	1.00	1.01	1.27
3000	1.02	1.05	1.03	1.01	1.01	1.00	1.01	1.00	1.01	1.26
2000	1.01	1.04	1.02	1.01	1.01	1.00	1.01	1.00	1.00	1.23
1000	1.00	0.99	1.01	1.00	1.00	0.99	1.00	1.00	1.00	1.17
800	0.99	0.98	1.01	1.00	1.00	0.99	1.00	1.00	1.00	1.13
600	0.99	0.96	1.00	0.99	1.00	0.99	0.99	1.00	1.00	1.08
400	1.01	0.98	0.99	1.00	1.00	1.00	0.99	1.00	1.00	1.00
300	1.06	1.06	0.98	1.01	1.00	1.01	0.99	1.00	1.00	0.94
250	1.12	1.17	0.98	1.04	1.00	1.03	1.00	1.00	1.00	0.91
200	1.26	1.43	0.99	1.09	1.00	1.06	1.03	1.00	1.00	0.91
150	1.65	2.18	1.02	1.24	1.02	1.16	1.11	1.02	1.00	0.96
100	3.30	6.23	1.20	1.78	1.09	1.51	1.42	1.06	1.02	1.30

Table A.2: *Colour correction values for LW filters for different power laws ($F_\nu \sim \lambda^{-\alpha}$). Note that the spectral index $\alpha = -1$ gives the 'a priori' assumed spectrum ($F_\nu(\nu) \sim \nu^{-1}$) and the colour correction is thus unity at all wavelengths.*

α	LW1	LW2	LW3	LW4	LW5	LW6	LW7	LW8	LW9	LW10
3.0	1.05	1.17	1.07	1.03	1.01	1.01	1.03	1.00	1.01	1.50
2.5	1.04	1.12	1.05	1.03	1.01	1.01	1.02	1.00	1.01	1.39
2.0	1.03	1.09	1.03	1.02	1.01	1.00	1.01	1.00	1.01	1.30
1.5	1.02	1.05	1.02	1.01	1.01	1.00	1.01	1.00	1.00	1.22
1.0	1.01	1.03	1.01	1.01	1.01	1.00	1.00	1.00	1.00	1.15
0.5	1.01	1.01	1.00	1.01	1.00	1.00	1.00	1.00	1.00	1.10
0.0	1.01	1.00	1.00	1.00	1.00	1.00	1.00	1.00	1.00	1.06
−0.5	1.00	1.00	1.00	1.00	1.00	1.00	1.00	1.00	1.00	1.02
−1.0	1.00	1.00	1.00	1.00	1.00	1.00	1.00	1.00	1.00	1.00
−1.5	1.00	1.01	1.01	1.00	1.00	1.00	1.00	1.00	1.00	0.98
−2.0	1.00	1.02	1.01	1.00	1.00	1.01	1.01	1.00	1.00	0.97
−2.5	1.00	1.04	1.02	1.00	1.00	1.01	1.01	1.00	1.00	0.97
−3.0	1.00	1.06	1.04	1.01	1.00	1.02	1.02	1.01	1.00	0.97

Table A.3: *Colour correction values for SW filters for different blackbody temperatures.*

Temp	SW1	SW2	SW3	SW4	SW5	SW6	SW7	SW8	SW9	SW10	SW11
10000	1.05	1.00	1.07	1.03	1.04	1.01	0.96	1.00	1.02	0.98	1.03
5000	1.04	1.00	1.06	1.03	1.02	1.01	0.97	1.00	1.02	0.99	1.03
4000	1.04	1.00	1.06	1.03	1.02	1.01	0.97	1.00	1.02	0.99	1.02
3000	1.03	1.00	1.05	1.02	1.01	1.00	0.97	1.00	1.02	0.99	1.02
2000	1.02	1.00	1.04	1.01	0.99	1.00	0.98	1.00	1.01	0.99	1.02
1000	0.99	1.00	1.00	0.98	0.96	1.00	1.01	1.00	1.00	0.99	1.00
800	0.98	1.00	0.99	0.98	0.97	1.00	1.03	1.00	0.99	1.00	1.00
600	0.99	1.01	0.97	0.98	1.01	1.00	1.06	1.00	0.99	1.01	0.99
400	1.06	1.02	0.96	1.04	1.27	1.02	1.15	1.01	0.97	1.03	0.96
300	1.21	1.05	0.97	1.14	1.80	1.06	1.26	1.01	0.97	1.06	0.94
250	1.40	1.07	1.01	1.27	2.53	1.11	1.38	1.02	0.97	1.08	0.93
200	1.84	1.12	1.11	1.56	4.53	1.22	1.59	1.03	0.98	1.14	0.92
150	3.23	1.25	1.39	2.36	13.54	1.50	2.10	1.06	1.03	1.24	0.91
100	13.52	1.66	2.68	6.54	–	2.78	4.17	1.16	1.39	1.59	0.91

Table A.4: *Colour correction values for SW filters for different power laws ($F_\nu \sim \lambda^{-\alpha}$). Note that the spectral index $\alpha = -1$ gives the 'a priori' assumed spectrum ($F_\nu(\nu) \sim \nu^{-1}$) and the colour correction is thus unity at all wavelengths.*

α	SW1	SW2	SW3	SW4	SW5	SW6	SW7	SW8	SW9	SW10	SW11
3.0	1.09	1.00	1.11	1.06	1.12	1.02	0.95	1.00	1.03	0.98	1.04
2.5	1.07	1.00	1.09	1.05	1.08	1.01	0.96	1.00	1.03	0.98	1.03
2.0	1.06	1.00	1.08	1.04	1.05	1.01	0.96	1.00	1.02	0.98	1.03
1.5	1.04	1.00	1.06	1.03	1.03	1.01	0.97	1.00	1.02	0.99	1.02
1.0	1.03	1.00	1.04	1.02	1.01	1.00	0.97	1.00	1.01	0.99	1.02
0.5	1.02	1.00	1.03	1.02	1.00	1.00	0.98	1.00	1.01	0.99	1.01
0.0	1.01	1.00	1.02	1.01	0.99	1.00	0.99	1.00	1.01	0.99	1.01
−0.5	1.00	1.00	1.01	1.00	0.99	1.00	0.99	1.00	1.00	1.00	1.00
−1.0	1.00	1.00	1.00	1.00	1.00	1.00	1.00	1.00	1.00	1.00	1.00
−1.5	1.00	1.00	0.99	1.00	1.01	1.00	1.01	1.00	1.00	1.00	1.00
−2.0	1.00	1.00	0.99	0.99	1.03	1.00	1.01	1.00	0.99	1.01	0.99
−2.5	1.00	1.00	0.98	0.99	1.06	1.00	1.02	1.00	0.99	1.01	0.99
−3.0	1.00	1.00	0.98	0.99	1.09	1.00	1.03	1.00	0.99	1.02	0.98

Appendix B

Magnitude System in ISOCAM

The zero magnitude of a given ISOCAM filter is defined as the signal of the 'ideal' (i.e. model) Vega which would have been measured in that filter with an infinitely large aperture.

The ideal spectrum of Vega was derived from a Kurucz model with $T_{eff} = 9400$ K , log $g = 3.9$, metal poor, $V_{turb} = 0.0 \ \mathrm{km\,s^{-1}}$ and no infrared excess due to circumstellar dust, extended to 300 μm and absolutely calibrated as described by Cohen et al. 1992, [18] and Walker & Cohen 1992, [64].

The magnitude m_{filter} can then be obtained from the CAM auto-analysis data product by applying the relation:

$$m_{filter} = -2.5\log\ [\frac{F_\nu(measured)}{F_{\nu,0}}]\ , \tag{B.1}$$

where $F_\nu(measured)$ is the flux density obtained from the ISOCAM data product (without colour correction). The values of $F_{\nu,0}$ for the different filter identifiers and reference wavelengths λ_{ref} are listed in Table B.1.

For completeness, we have included in Table B.1 the ideal Vega flux density at the reference wavelength $F_\nu(\lambda_{ref})$, and the colour correction K.

The values of K are very close to the ones which have been derived for a 10000 K blackbody (see Appendix A).

Table B.1: *Zero magnitude flux densities of the different ISOCAM filter bands.*

filter ID	λ_{ref} [μm]	$F_{\nu,0}(\lambda_{ref})$ [Jy]	$F_{\nu}(\lambda_{ref})$ [Jy]	K [ ]
SW1	3.6	280.5	267.7	1.05
SW2	3.3	313.2	301.5	1.04
SW3	4.5	189.6	178.9	1.06
SW4	2.8	434.4	426.9	1.02
SW5	4.0	229.1	219.9	1.04
SW6	3.7	256.0	253.9	1.01
SW7	3.0	360.2	376.3	0.96
SW8	4.05	213.4	209.1	1.02
SW9	3.9	235.4	227.9	1.03
SW10	4.6	167.6	171.4	0.98
SW11	4.26	201.8	197.6	1.02
LW1	4.5	181.9	178.9	1.02
LW2	6.7	90.2	83.7	1.08
LW3	14.3	19.7	19.1	1.03
LW4	6.0	105.1	103.6	1.02
LW5	6.8	82.1	81.4	1.01
LW6	7.7	64.0	64.0	1.00
LW7	9.6	42.2	41.7	1.01
LW8	11.3	30.3	30.3	1.00
LW9	14.9	17.7	17.6	1.01
LW10	12.0	34.7	26.9	1.29

Appendix C

ISOCAM Data Products per AOT

The list of CAM-specific data products is shown in the Table C.1 below as a function of the AOT in operation. Note that some CAM05 observations were uplinked using the CUS which always set the AOT name to 'CAM99'. The symbol ‖ refers to CAM Parallel observations.

Table C.1: *ISOCAM data products per AOT*

	AOT1	AOT3	AOT4	AOT5	‖	
CCSH	Yes	Yes	Yes	Yes	Yes	CAM Continuous Compact Status
CDER	Yes	Yes	Yes	Yes	Yes	CAM Diagnostic Edited Raw Data
CIER	Yes	Yes	Yes	Yes	No	CAM Image ERD
CPER	No	No	No	No	Yes	CAM Parallel Image ERD
CSTA	Yes	Yes	Yes	Yes	Yes	CAM Compact Status
CISP	Yes	Yes	Yes	Yes	No	CAM Standard Processed Data
CPSP	No	No	No	No	Yes	CAM Parallel Standard Processed Data
CCIM	Yes	Yes	Yes	Yes	Yes	CAM Images in detector coordinates
CGLL	Yes	Yes	Yes	Yes	Yes	CAM Glitch List
CJAM	Yes	Yes	Yes	Yes	Yes	CAM Jitter, Memory and Stabilisation information
CMAP	Yes	Yes	Yes	Yes	Yes	CAM Celestial IR image
CMOS	Yes	Yes	Yes	Yes	Yes	CAM Celestial IR mosaic
CPSL	Yes	Yes	Yes	Yes	Yes	CAM Point Source List
CSSP	Yes	Yes	Yes	Yes	Yes	CAM Source Spectra
CUFF	Yes	Yes	Yes	Yes	Yes	CAM User-Friendly log File
CISR	Yes	Yes	Yes	Yes	Yes	CAM Instrument Station Report
COLR	Yes	Yes	Yes	Yes	Yes	CAM CAM Off-Line Processing Report
C*	Yes	Yes	Yes	Yes	Yes	All the calibration files in Table 5.2

Appendix D

AAC FORTRAN Code Showing CAL-G Selection Rules

When an exact match to an observer's data is absent from the set of CAL-G files, AAC choses an alternative based on minimising a penalty function calculated by the fragment of code listed below. The penalty function is made up of distances in selection parameter space weighted by factors which include parameter priority order.

```
C+++++++++++++++++++++++++++++++++++++++++++++++++++++++++++++++++++++++
C.IDENTIFIER  CCD_PENALTY
C.PURPOSE     Returns value of best-fit penalty function.
C.VERSION 1  Steve 03-05-1995 Original
C.VERSION 2   Andy 24-07-1996 cam$penalty report
C.VERSION 3   Andy 30-07-1996 cfo_ccd_names & cfo_ccd_values
C.VERSION 4   Andy 02-02-2000 cfo_ccd_values key_id
C.CALLS       CCD_GET_MULTS
C             CCD_DIFF
C             CAM_REPORT
C             CAM_INFO
C-----------------------------------------------------------------------
      subroutine ccd_penalty (new_keys, deid, n_key, key_id, val1, val2,
     &                        penalty, status)
* Global constants:
      include 'aac_inc:aac_ccd_constants.inc'
      include 'aac_inc:aac_cam_codes.inc'
* Import:
      logical new_keys           !  in: new set of keys?
      integer deid               !  in: detector id
      integer n_key              !  in: number of keys
      character*(*) key_id(*)    !  in: names of keys
      real val1(*)               !  in: set of values, each key
      real val2(*)               !  in: set of values, each key
      real penalty               ! out: calculated penalty value
* Status:
      integer status
* Locals variables:
      real*4 pen_mult(ccd$maxkeys)
```

```
      integer*4 i_key
      real*4 diff
* External references:
      real*4 ccd_diff
      character*(cam$lo) cfo_ccd_names
      character*(cam$lo) cfo_ccd_values
      character*(cam$lc) cam_channel
*-
      if(status.ne.cam$normal)return

* Derive the penalty multipliers.
      if (new_keys) call ccd_get_mults (n_key, key_id, pen_mult, status)

* Initialise.
      penalty = 0.0

* Use these to sum the penalty function.
      do i_key = 1, n_key
          ! find absolute 'distance' between the values
          diff = ccd_diff (deid, key_id(i_key),
     &                     val1(i_key), val2(i_key))

          if (diff.ge.0.0) then
              penalty = penalty + diff*pen_mult(i_key)
          else
              status=cam$penalty
              call cam_report(' ',key_id(i_key),status)
          endif
      end do

* Report more details of any failure
      if(status.ne.cam$normal)then
         call cam_info(cfo_ccd_names(cam_channel(deid),n_key,key_id))
         call cam_info(cfo_ccd_values('Tried: ',n_key,key_id,val1))
         call cam_info(cfo_ccd_values('Failed:',n_key,key_id,val2))
      endif

      return

      end

C+++++++++++++++++++++++++++++++++++++++++++++++++++++++++++++++++++++++++
C.IDENTIFIER  CCD_GET_MULTS
C.PURPOSE     Returns penalty multipliers for each key.
C.VERSION 1  Steve 03-05-1995 Original
C.VERSION 2   Andy 24-07-1996 cam$multiplier report
C.CALLS       CCD_MAXKEY
C             CAM_REPORT
C-------------------------------------------------------------------------
      subroutine ccd_get_mults (n_key, key_id, pen_mult, status)
      implicit none
```

```
* Arguments:
      integer n_key               !  in: number of keys
      character*(*) key_id(*)     !  in: names of keys
      real pen_mult(*)            ! out: penalty multiplier, each key
      integer status              ! i/o: status value

* Include files.
      include 'aac_inc:aac_cam_codes.inc'

* Locals.
      real maxval                 ! returned by ccd_maxkey
      integer i_key               ! key index

* Functions.
      real ccd_maxkey             ! returns maximum value of key

* Inherited status.
      if (status.ne.cam$normal) return

* Muliplier for the last key is one by definition.
      pen_mult(n_key) = 1.0

* Construct the other multipliers as the product of the maximum values of the
* ones that follow it ie pen_mult(i) = product(pen_mult(i+1)...pen_mult(n))
      do i_key = n_key-1, 1, -1
          maxval = ccd_maxkey(key_id(i_key+1))

          if (maxval.ge.0.0) then
              pen_mult(i_key) = pen_mult(i_key+1) * maxval
          else
              status=cam$multiplier
              call cam_report(' ',key_id(i_key+1),status)
          endif
      end do

      return

      end

C+++++++++++++++++++++++++++++++++++++++++++++++++++++++++++++++++++++++++
C.IDENTIFIER  CCD_MAXKEY
C.PURPOSE     Returns maximum value of a key; -1 if none.
C.VERSION 1  Steve 03-05-1995 Original
C.VERSION 2  Steve 09-05-1996 Use pixel fraction in PSF selection
C.VERSION 3   Andy 16-02-2000 ccd$proc & ccd$rev
C-------------------------------------------------------------------------
      real function ccd_maxkey (key_id)
      implicit none

* Arguments:
      character*(*) key_id             ! in: name of the key
```

```
* Include files:
      include 'aac_inc:aac_ccd_constants.inc'

* Local constants.
      real bad_val
      parameter (bad_val = -1.0)

      if (key_id.eq.ccd$ewhl) then
          ccd_maxkey = 8.0

      else if (key_id.eq.ccd$swhl) then
          ccd_maxkey = 5.0

      else if (key_id.eq.ccd$tint) then
          ccd_maxkey = 431.0

      else if (key_id.eq.ccd$gain) then
          ccd_maxkey = 5.0

      else if (key_id.eq.ccd$pfov) then
          ccd_maxkey = 8.0

      else if (key_id.eq.ccd$proc) then
          ccd_maxkey = 2.0

      else if (key_id.eq.ccd$signal) then
          ccd_maxkey = 5001.0

      ! do nothing for y - treat as null key and wait for z
      else if (key_id.eq.ccd$ys) then
          ccd_maxkey = 1.0

      ! maximum is corner-to-corner distance + an allowance of 3 times
      ! that for the fractional pixel weighting
      else if (key_id.eq.ccd$zs) then
          ccd_maxkey =  4.0 * sqrt(2.0) * cam$ny

      ! maximum is in wavelength
      else if (key_id.eq.ccd$fcvf) then
          ccd_maxkey = 18.0

      else if (key_id.eq.ccd$rev) then
          ccd_maxkey = 907.0

      else
          ccd_maxkey = bad_val
      endif

      return

      end
```

```
C+++++++++++++++++++++++++++++++++++++++++++++++++++++++++++++++++++++++++
C.IDENTIFIER  CCD_DIFF
C.PURPOSE     Returns 'difference' between values; -1 if undefined.
C.VERSION 1   Steve 03-05-1995 Original
C.VERSION 2   Steve 08-01-1996 don't allow diff=0 unless val1=val2;
C                              penalise CVF/non-CVF pairs
C-------------------------------------------------------------------------
      real*4 function ccd_diff(deid, key_id, val1, val2)
* Global constants:
      include 'aac_inc:aac_ccd_constants.inc'
* Import:
      integer*4 deid
      character*(*) key_id
      real*4 val1
      real*4 val2
* Local constants:
      real bad_val
      parameter (bad_val = -1.0)
      real epsilon
      parameter (epsilon = 1.0e-6)     ! arbitrary small value
* Local variables:
      real*4 trans_val1
      real*4 trans_val2
* External references:
      real    ccd_transval       ! translates raw values to 'difference system'
      real    ccd_maxkey         ! returns maximum value of key
      logical ccd_iscvf          ! check if CVF position
*-

* Translate the values to our 'difference weighting system'.
      trans_val1 = ccd_transval (deid, key_id, val1)
      trans_val2 = ccd_transval (deid, key_id, val2)

* If OK, return the absolute value, -1 otherwise.
      if (trans_val1.ge.0.0 .and. trans_val2.ge.0.0) then
          ccd_diff = abs (trans_val1 - trans_val2)

          ! don't allow diff=0 unless the inputs were the same
          ! instead return difference between inputs multiplied by
          ! some (small) arbitrary value
          if (ccd_diff.le.0.0 .and. val1.ne.val2)
     &        ccd_diff = epsilon * abs(val1 - val2)

          ! for filter wheels, penalise CVF/non-CVF pairs
          if (key_id.eq.ccd$fcvf) then
              if (ccd_iscvf(deid,nint(val1)) .xor.
     &            ccd_iscvf(deid,nint(val2)))
     &            ccd_diff = ccd_diff + ccd_maxkey(key_id)
          endif

      else
          ccd_diff = bad_val
```

```
      endif

      return

      end

C++++++++++++++++++++++++++++++++++++++++++++++++++++++++++++++++++++++++
C.IDENTIFIER  CCD_TRANSVAL
C.PURPOSE     Returns value in 'difference' system; -1 if undefined.
C.VERSION 1  Steve 03-05-1995 Original
C.VERSION 2  Steve 09-05-1996 Use pixel fraction in PSF selection
C.VERSION 3   Andy 10-02-1998 Alpha tidy up
C.CALLS       None.
C------------------------------------------------------------------------
      real*4 function ccd_transval(deid,key_id,val)
* Include files:
      include 'aac_inc:aac_ccd_constants.inc'
      include 'aac_inc:aac_cam_codes.inc'
* Import:
      integer*4 deid
      character*(*) key_id
      real*4 val
* Local constants:
      real*4 bad_val
      parameter (bad_val=-1.0)
      real*4 val_undef
      parameter (val_undef=-1.0)
* Local variables:
      integer*4 ival
      real*4 dist
      real*4 frac
      real*4 yval1
      real*4 yval2
      real*4 zval1
      real*4 bandwidth
      integer*4 status
* Local data:
      data yval1 /val_undef/
      data yval2 /val_undef/
      data zval1 /val_undef/
* Saved variables:
      save yval1, yval2, zval1
* External references:
      real*4 ccd_wavelength
*-

      if (key_id.eq.ccd$ewhl) then
          ival = nint(val)
          if (ival.eq.cam$ewhl_pol1) then
              ccd_transval = 1.0
          else if (ival.eq.cam$ewhl_pol2) then
              ccd_transval = 2.0
```

```
    else if (ival.eq.cam$ewhl_pol3) then
        ccd_transval = 3.0
    else if (ival.eq.cam$ewhl_hole) then
        ccd_transval = 6.0
    else if (ival.eq.cam$ewhl_dark) then
        ccd_transval = 7.0
    else
        ccd_transval = bad_val
    endif

else if (key_id.eq.ccd$swhl) then
    ival = nint(val)
    if (deid.eq.cam$sw) then
        if (ival.eq.cam$swhl_sw_sm) then        ! SW small mirror
            ccd_transval = 1.0
        else if (ival.eq.cam$swhl_sw_lm) then   ! SW large mirror
            ccd_transval = 3.0
        else if (ival.eq.cam$swhl_sw_ics) then  ! SW ics
            ccd_transval = 4.0
        else
            ccd_transval = bad_val
        endif

    else if (deid.eq.cam$lw) then
        if (ival.eq.cam$swhl_lw_sm) then        ! LW small mirror
            ccd_transval = 1.0
        else if (ival.eq.cam$swhl_lw_lm) then   ! LW large mirror
            ccd_transval = 3.0
        else if (ival.eq.cam$swhl_lw_ics) then  ! LW ics
            ccd_transval = 4.0
        else
            ccd_transval = bad_val
        endif

    else
        ccd_transval = bad_val
    endif

else if (key_id.eq.ccd$pfov) then
    ival = nint(val)
    if (deid.eq.cam$sw) then
        if (ival.eq.cam$sw_pfov1) then
            ccd_transval = 1.0
        else if (ival.eq.cam$sw_pfov2) then
            ccd_transval = 2.0
        else if (ival.eq.cam$sw_pfov3) then
            ccd_transval = 4.0
        else if (ival.eq.cam$sw_pfov4) then
            ccd_transval = 8.0
        else
            ccd_transval = bad_val
        endif
```

```
        else if (deid.eq.cam$lw) then
            if (ival.eq.cam$lw_pfov1) then
                ccd_transval = 1.0
            else if (ival.eq.cam$lw_pfov2) then
                ccd_transval = 2.0
            else if (ival.eq.cam$lw_pfov3) then
                ccd_transval = 4.0
            else if (ival.eq.cam$lw_pfov4) then
                ccd_transval = 8.0
            else
                ccd_transval = bad_val
            endif

        else
            ccd_transval = bad_val
        endif

    else if (key_id.eq.ccd$tint) then
        ccd_transval = val

    else if (key_id.eq.ccd$signal) then
        ccd_transval = val

    else if (key_id.eq.ccd$gain) then
        ival = nint(val)
        if (ival.eq.cam$gain1) then
            ccd_transval = 2.0
        else if (ival.eq.cam$gain2) then
            ccd_transval = 1.0
        else if (ival.eq.cam$gain4) then
            ccd_transval = 3.0
        else
            ccd_transval = bad_val
        endif

    ! do nothing for y - treat as null key and wait for z
    ! we always return the same number, so the difference will be 0
    else if (key_id.eq.ccd$ys) then
        ccd_transval = 1.0
        if (yval1.lt.0.0) then
            yval1 = val
        else if (yval2.lt.0.0) then
            yval2 = val
        else
            ccd_transval = bad_val
        endif

    ! now calculate distance between z & remembered y plus 96*sqrt(2) times
    ! the fractional distance (this assumes the PSFs are sampled at one
    ! third intervals) - the factor is sqrt(2) * 32 * sample rate. The
    ! point is that the fractional distance is always more important than
```

```
! the real distance.
! The first call will correspond to yval1. Return 0 for z1 and the
! calculated value for z2 so the difference will be correct.
else if (key_id.eq.ccd$zs) then
    if (zval1.lt.0.0) then      ! z1
        zval1 = val
        ccd_transval = 0.0

    else if (yval1.ge.0.0 .and. yval2.ge.0) then ! z2
        dist = sqrt ((val   - zval1)**2 +
&                    (yval2 - yval1)**2)
        frac = sqrt ((val   - real(nint(val)) -
&                     zval1 + real(nint(zval1)))**2 +
&                    (yval2 - real(nint(yval2)) -
&                     yval1 + real(nint(yval1)))**2)
        ccd_transval = dist + frac * 96.0 * sqrt(2.0)

        yval1 = val_undef
        yval2 = val_undef
        zval1 = val_undef

    else
        ccd_transval = bad_val
    endif

else if (key_id.eq.ccd$fcvf) then
    ival = nint(val)
    status=cam$normal
    ccd_transval=ccd_wavelength(deid,ival,bandwidth,status)
    if (ccd_transval.lt.0.0) ccd_transval = bad_val

else if (key_id.eq.ccd$proc) then
    ccd_transval = val

else if (key_id.eq.ccd$rev) then
    ccd_transval = val

else
    ccd_transval = bad_val
endif

return

end
```

Appendix E

Deglitching in OLP

At first sight, the images from ISOCAM are crossed by strings of high value pixels produced by cosmic ray impacts. Most of these glitches are due to mild, fast electron energy deposition along a string of pixels. Typically for the LW detector, on average, about 40 to 60 pixels are affected at any time for an integration time of 5 seconds. Those pixels usually recover completely after one or two readouts. However, some impacts can have long lasting effects (up to 5 minutes) on the hit pixel. They are thought to be due to heavy particles. There is one glitch about every second somewhere on the LW channel. Further description of the ISOCAM glitches is given in Section 4.3.

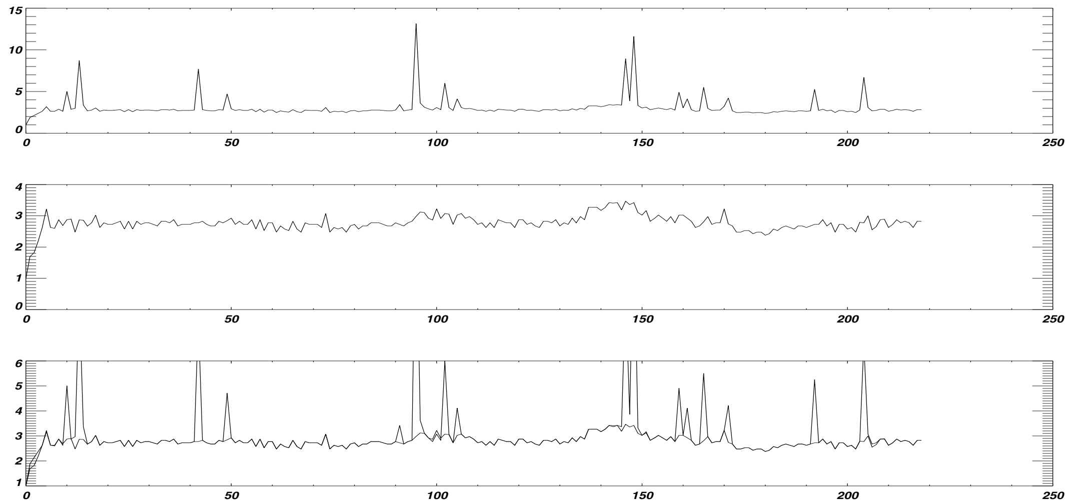

Figure E.1: *An example of deglitching in OLP with the help of the MMT method; original data (top), deglitched data (middle), and both overplotted (bottom).*

Cosmic ray impact suppression (also called deglitching) is not a trivial task for several reasons. First of all the data are rarely fully stabilised (i.e. it takes a long time until the pixel reaches a stabilised value, although the incoming flux is constant) and this implies that not all differences between two successive frames can be attributed to cosmic ray impacts. Secondly, several glitches can hit the same pixel successively and create a long temporal structure which could be considered as a source by a simple algorithm. As the glitch structures can have different sizes, we need a multi-resolution tool in order to perform efficient automatic detection. The wavelet transform is not well adapted to treat this kind of

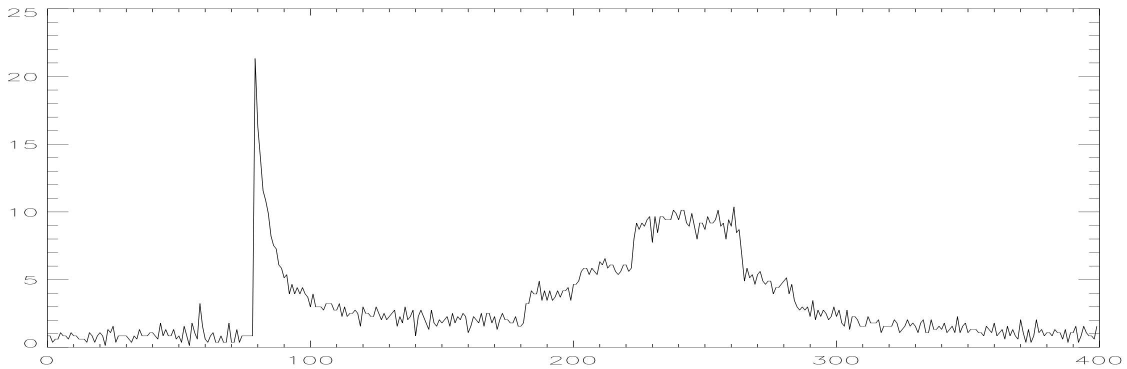

Figure E.2: *Glitch with very long duration. The flux in ADUs is plotted against time given by the exposure index.*

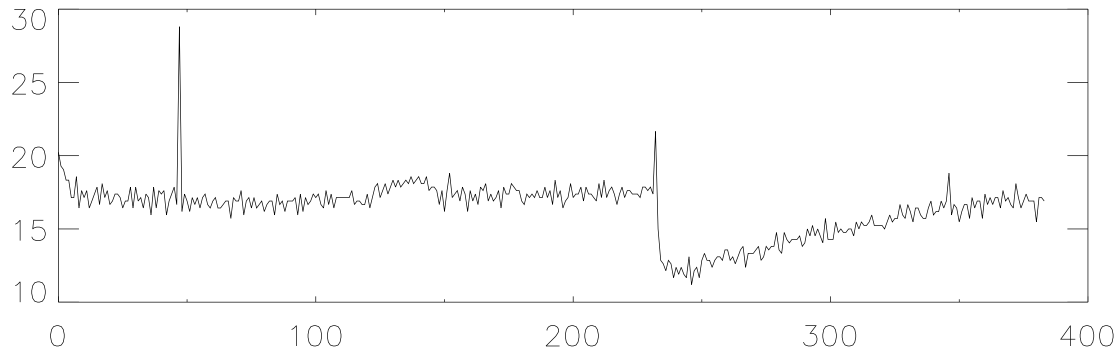

Figure E.3: *Glitch with a negative tail. The flux in ADUs is plotted against time given by the exposure index. Note the gain variation of about 5 ADUs which appears after the second glitch.*

data, due to the linearity of the transform. At a glitch position, a structure would be detected at all scales. This is due to the high intensity of the glitch. The Multi-resolution Median Transform (MMT) (Starck et al. 1998, [57]) is an alternative to the wavelet transform. It is a non-linear multi-resolution transform, and is particularly useful every time we have structures with large dynamics. This is the case for the deglitching problem. The idea developed here is the following (Starck et al. 1999a, [58]): as we observe the same position in the sky during n exposures, we cannot have any structure in the signal which has a temporal size lower than $n \cdot tint$. This means that all the significant structures (i.e. not due to the noise) at small scales are due to the glitches. The method consists in taking the MMT for each pixel (x, y), to set to zero all structures higher than a given level (determined from a noise modelling) in the smaller scales, and to reconstruct the deglitched temporal signal.

Figure E.1 shows the results of such a treatment. Figure E.1 (top) shows the values of a pixel of the camera as time elapses. The x-axis represents the frame number (time / integration time), and the y-axis is the signal in ADUs per second. These data were collected during a raster observation, and the satellite remained at the same position for about 20 frames, and the integration time was equal to 2.1 s. A source is at the limit of detection (frames 135 to 150). All peaks are due to cosmic ray impacts. Figure E.1 (middle) shows the same data after the glitch suppression. The bottom panel shows both data and deglitched data overplotted. We see that the noise and the signal are not modified during this operation.

The method is robust and works for non-stabilised data. The only real limitation is that we cannot detect glitches which last for a time longer than or equal to $n \cdot tint$. That means that the more frames we have per camera configuration, the better the deglitching will be. Some 'special' glitches introduce a gain variation with a very long time duration. These special glitches can be separated in two types:

1. the pixel value decreases slowly until a stabilised value is reached (see Figure E.2);
2. the pixel value decreases first below the stabilised value, and then increase slowly until the stabilised value is reached (see Figure E.3).

In both cases, the stabilisation can be very slow, and the deglitching method presented here does not correct for this effect. As a result, pixels where a glitch has been detected are not used when averaging values corresponding to the same sky position and same configuration.

Appendix F

Optimising ISOCAM Data Processing Using Spatial Redundancy

F.1 Introduction

Much effort has been made to model the response of the ISOCAM array based on the theoretical understanding of infrared detectors (Abergel et al. 1999, [1]; Coulais & Abergel 2000, [21], and references therein) and sophisticated data reduction techniques have been developed to take into account some aspects of the ISOCAM response (Starck et al. 1999a, [58]; Désert et al. 1999, [29]; Aussel et al. 1999, [4]; Altieri et al. 1999, [3]). These methods are close to being optimal for the detection of point sources. Nevertheless, in many observations, instrumental effects still prevent the study of faint extended emission.

To be able to study extended emission, instrumental effects with variable time scales must be corrected. We present here a method that makes use of the spatial redundancy of raster-type observations to correct the Long Term Transient (LTT; see Figure F.1) and memory effects after glitches and strong point sources (see Figure F.2). The details are described in Miville-Deschênes et al. 2000, [41]. The processing steps here described are part of the so-called SLICE package, which is a standalone reduction package within IDL dedicated to the reduction of ISOCAM redundant observations. SLICE can also be used within CIA.

To illustrate these data processing techniques we will show in the following two different observations of the same field, the gamma-ray burst GRB 970402, obtained sequentially in exactly the same configuration (LW10 filter, $6''$ pfov) on revolution 506. The amplitude of the instrumental effects are not the same in both observations, giving us constraints on the validity of the method (see Figure F.3).

Another example showing the result of this type of processing, this time on an image of the ISOGAL survey is shown in Figure F.4 (Omont et al. 1999, [47]; Pérault et al. 1996, [49]).

F.2 Long Term Transient Correction

Unlike the short term transient, no analytical or physical description has been developed so far to correct the LTT which seems to be a general behaviour of the ISOCAM detectors. Here we show how to correct the LTT by a least square minimization technique that makes use of the spatial redundancy of raster type observations.

For a given pixel at a position (x, y) on the detector array and at a given time t, the observed flux $I_{obs}(x, y, t)$ is related to the temporally varying flat-field $F(x, y, t)$, the incident flux $I_{sky}(x, y, t)$ and the

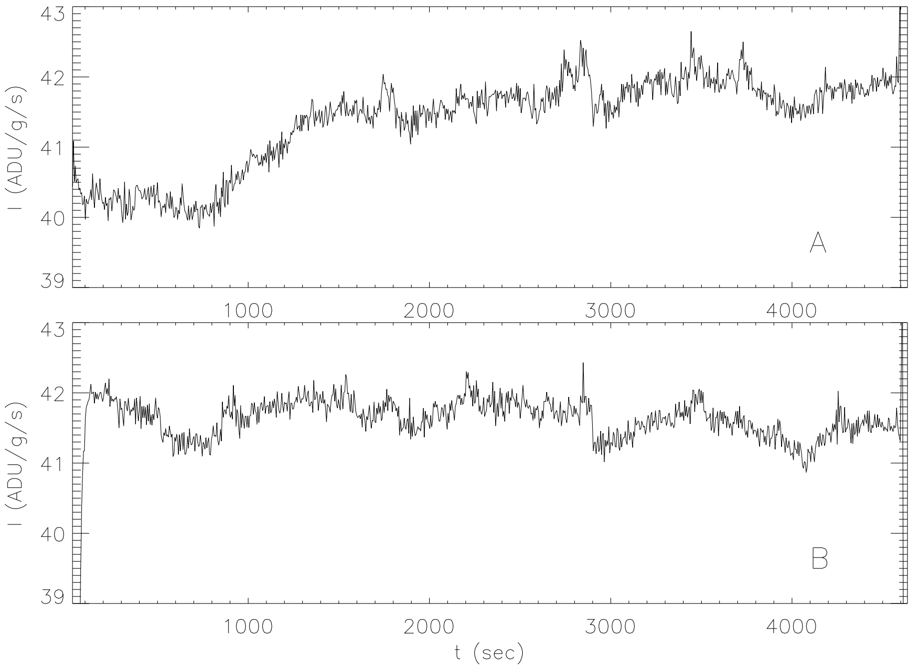

Figure F.1: *Temporal evolution of the flux observed by ISOCAM for two observations of the same field (observation of the gamma-ray burst GRB 970402). The LTT is seen in the first observation (A), but not in the second (B). When observed, the amplitude of the LTT is about 5% of the total sky emission and gradually attenuates on a variable time scale which can be up to several hours. The sky image of the first observation, computed from the raw data, (Figure F.3a) is completely dominated by this long term drift.*

long term drift $\Delta(t)$ by the following equation:

$$I_{obs}(x, y, t) = F(x, y, t)\ I_{sky}(x, y, t) + \Delta(t). \tag{F.1}$$

Here we suppose that $\Delta(t)$ is not pixel dependent.

The offset function $\Delta(t)$ is found using equation F.1 and the spatial redundancy inherent to raster mode observations. We determine $\Delta(t)$ by solving a set of linear equations obtained by comparing flat-field corrected intensities of the same sky positions but obtained at different times.

The function of interest $\Delta(t)$ is estimated by minimizing the following criterion:

$$\begin{aligned}\chi^2 \quad = \quad & \sum_{\alpha,\delta,t_i,t_j} \left[\frac{I_{obs}(\alpha,\delta,t_i)}{F(\alpha,\delta,t_i)} - \frac{I_{obs}(\alpha,\delta,t_j)}{F(\alpha,\delta,t_j)} \right. \\ & \left. - \frac{\Delta(t_i)}{F(\alpha,\delta,t_i)} + \frac{\Delta(t_j)}{F(\alpha,\delta,t_j)} \right]^2 \end{aligned} \tag{F.2}$$

Here the sum is over all the possible pixel pairs that have seen the same region of the sky. The function $\Delta(t)$ is found by solving the linear system determined by the equation:

$$\frac{\partial \chi^2}{\partial \Delta(t_i)} = 0 \tag{F.3}$$

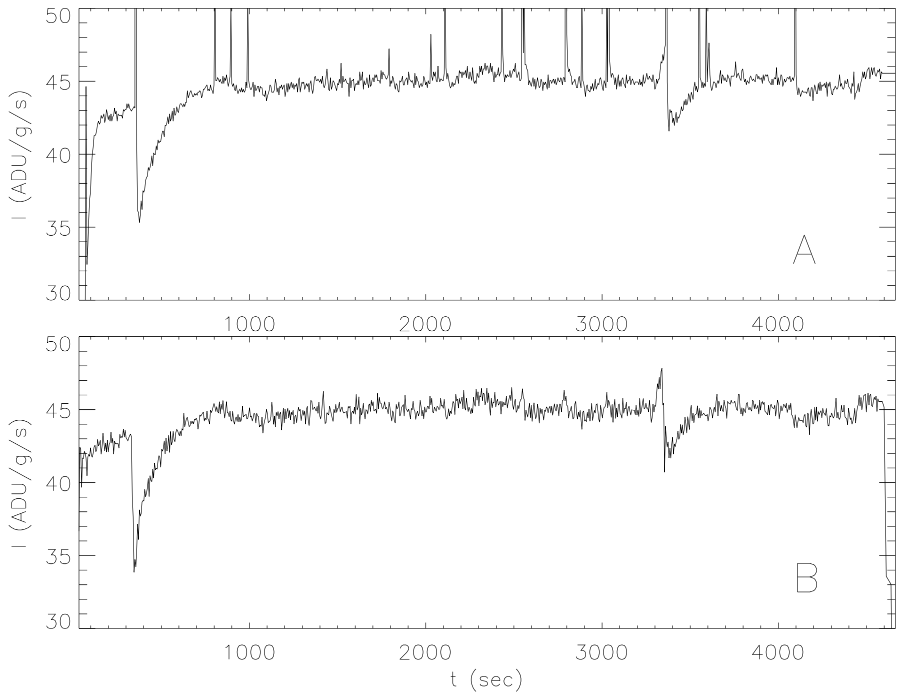

Figure F.2: *Temporal evolution of a typical pixel. A) Raw data - many energetic electrons have hit the pixel causing instantaneous flux steps known as fast glitches. A response change is apparent near* $t = 350$ *seconds caused by an ion impact (slow glitch). B) Fast glitches corrected data - short time flux steps have been identified as glitches and removed from the data cube. The glitch impact is removed correctly by the standard deglitching algorithm (Starck et al. 1999a, [58]) but the detector response is significantly disrupted for more than 500 seconds. These glitches with a memory effect are responsible for most of the periodic patterns seen in Figure F.3a. Such memory effects also occur after the observation of strong point sources.*

The details of this correction can be found in Miville-Deschênes et al. 2000, [41]. The sky image of the first GRB observation, obtained after the LTT correction, is shown in Figure F.3b. At this stage we have used a single flat-field to compute the sky image. However, it is still necessary to use a variable flat-field to correct the artefacts (e.g. periodic patterns) seen in Figure F.3b.

F.3 Variable Flat-Field

After the LTT has been corrected, we then take into account the pixel-to-pixel temporal variations of the detector response. These response variations (that represent ∼1–3% of the average flat-field) are observed at various time scales. To go further in the data processing, we try to correct these pixel-to-pixel response variations with a time dependent flat-field $F(x, y, t)$. Flat-field and sky structures are mixed together in $I_{obs}(x, y, t)$ (see Equation F.1) but the flat-field variations can be extracted from the data by estimating $I_{sky}(x, y, t)$ and by taking advantage of the spatial redundancy.
Here are the guidelines of this method:

1. Construct a sky image.
2. Smooth (median smoothing) the sky image with a 10×10 window.

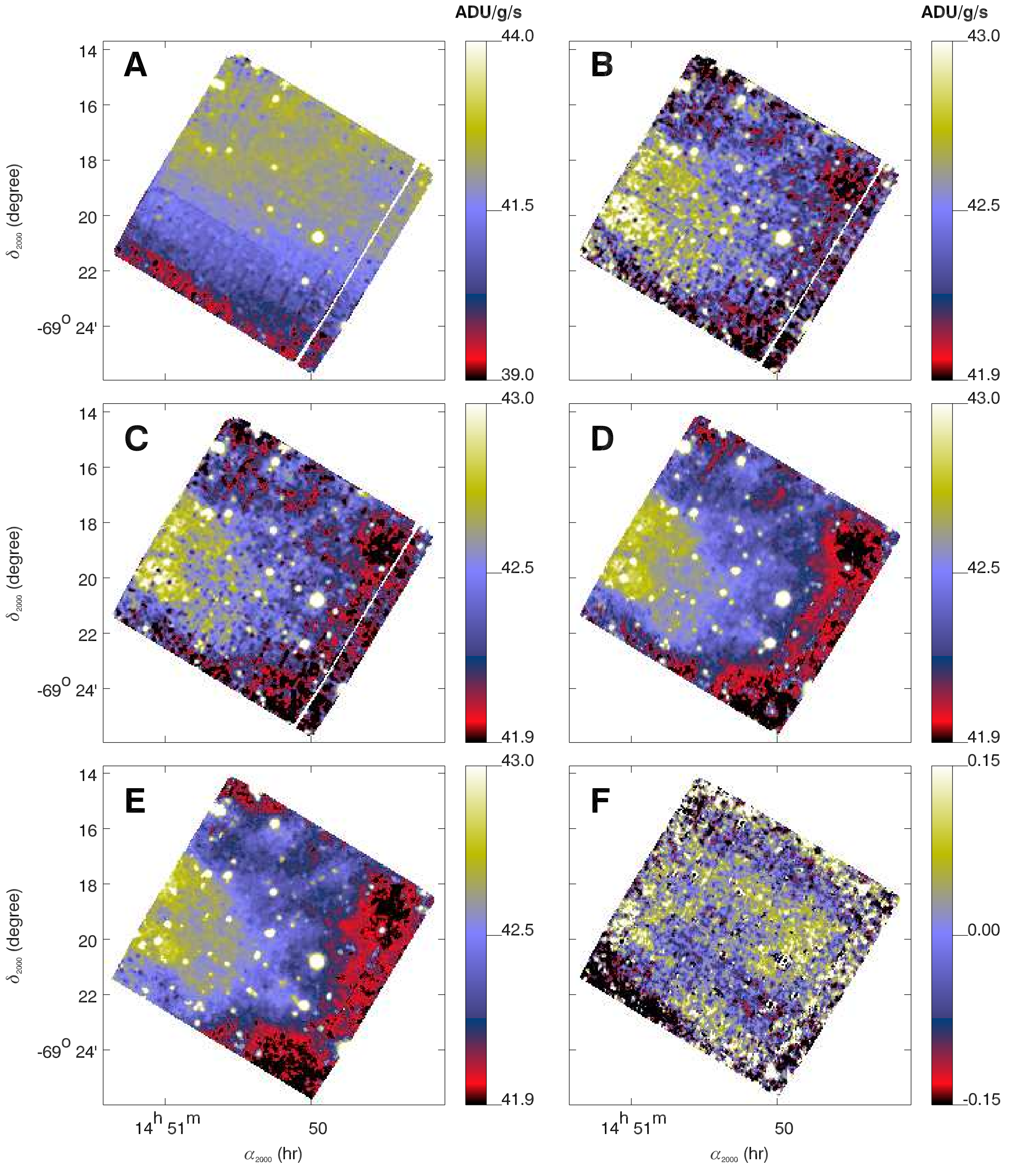

Figure F.3: *LW10 images of the first GRB970402 observation after deglitching, dark subtraction, transient correction (A), long term transient correction (B), variable flat-field (C) and bad pixel removal (D). Image (E) is the final map of the second GRB970402 observation and image (F) is the difference between (D) and (E). For these observations, 1 ADU/G/s corresponds to 0.242 mJy/pix or 0.286 MJy/sr.*

3. Compute an *ideal cube* $I_{sky}(x, y, t)$ by projecting the smoothed sky image on each readout of the data cube.
4. Smooth (median smoothing) $I_{obs}(x, y, t)/I_{sky}(x, y, t)$ on the time axis. The size of the smoothing window should be of the order of the time spent on 5 different sky positions. The result of this smoothing is the variable flat-field.

The sky image of the first GRB observation, obtained with the variable flat-field, is shown in Figure F.3c. The variable flat-field removes almost all periodic patterns due to high-frequency variations of the detector response.

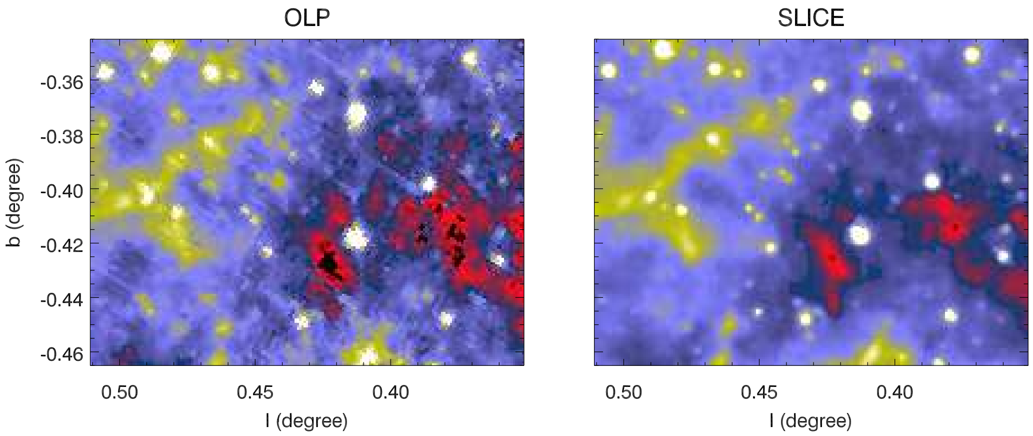

Figure F.4: *A small piece of an LW2 image of the ISOGAL survey.* **Left:** *image obtained from the standard pipeline data processing (OLP v9.1).* **Right:** *image obtained with SLICE, where the spatial redundancy is used to optimise the processing.*

F.4 Bad Pixel Identification

Usual deglitching methods that work on the time history of a given pixel are good to remove extremely deviant flux values. We can go further in the reduction of the noise level by working sky position by sky position instead of working on the time history of every pixel. For a given sky position (α, δ), we compare the N pixels in the data cube that have seen that position with the average flux in the map at the vicinity of the position (α, δ).

Three cases are possible, and here is how we deal with each case:

1. *Most of the N pixels are around the local average B.*
   The new sky flux is the average of ($B - 3 \times noise < I_{obs} < B + 3 \times noise$)
2. *Most of the N pixels are above the local average B.*
   The new sky flux is the average of $I_{obs} > B$
   This case corresponds to point sources.
3. *Most of the N pixels are under the local average B.*
   The new sky flux is the average of ($B - 3 \times noise < I_{obs} < B$).

This method allows us to reduce the noise level and to keep a good photometry of point sources. This is the final step of the data processing. The sky images obtained after bad pixel removal of the first and second GRB observations are presented in Figures F.3d and F.3e.

F.5 Assessment of the Method

From the comparison of the final maps of the two GRB observations shown in Figure F.3 we can estimate the reliability of this processing method. At first glance we see that the structure of the diffuse emission is very similar in both maps; the LTT correction applied seems to restore properly the large scale structure. Furthermore, almost all point like structures are present in both maps, giving confidence in the bad pixel identification performed. The difference of the two final sky images is shown in Figure F.3f. It is dominated by small-scale structure noise but large-scale structures are also apparent, probably due to error in the LTT correction. Extra noise is seen at point source positions. This was expected as memory effects are not fully corrected on point sources and as we are undersampling the point spread function. One also notices that the noise level is higher at the edges of the difference map, due to less redundancy in these regions.

The noise level is reduced by a factor of ten at 8 arcmin scale and a factor of two at the resolution limit. Actually, the final maps are dominated by the readout and photon noise.

Appendix G

List of Acronyms

AAC	ISOCAM Auto-Analysis
ADC	Analogue to Digital Converter
ADU	Analogue Digital Units
AOT	Astronomical Observation Template
CAL	Procedure when ISOCAM is performing an internal flat-field calibration
CAMTU	ISOCAM Time Units
CCG*DARK	ISOCAM Dark Current Exposures
CCG*DEAD	ISOCAM Dead Pixel Map
CCG*DFLT	ISOCAM Detector Flat-Field Library
CCGLWDMOD	LW parameters for the Time Dependent Dark correction
CCG*FRAME	ISOCAM Detector astrometric calibration
CCG*GLITCH	ISOCAM Glitch Model: Currently empty
CCG*LINEAR	ISOCAM Uniform Illumination Library
CCG*OFLT	ISOCAM Optical Flat-Field Library
CCG*PSF	ISOCAM Point-Spread-Function Library
CCG*SPEC	ISOCAM Filter & CVF spectral data
CCG*STRAY	ISOCAM Non-dark local light model
CCG*TRANS	ISOCAM Model transients: Currently empty
CCIM	ISOCAM Images in detector coordinates
CCSH	ISOCAM Continuous Compact Status
CDER	ISOCAM Diagnostic Raw data
CD-ROM	Compact Disk Read Only Medium
CGLL	ISOCAM Glitch List
CIA	ISOCAM Interactive Analysis package
CIER	ISOCAM Image ERD
CID	Charge Injection Device
CIDT	ISOCAM Instrument Dedicated Team
CISP	ISOCAM Standard Processed Data
CISR	ISOCAM Instrument Station Report
CIST	ISOCAM Instrument Science Team
CJAM	ISOCAM Jitter, Memory and Stabilisation information
CLN	ISOCAM procedure to clean the LW array
CLWCVF1	ISOCAM LW CVF1 description table

(*=SW, LW)

CLWCVF2	ISOCAM LW CVF2 description table
CMAP	ISOCAM Celestial IR image
CMOS	ISOCAM Celestial IR mosaic
CNF	ISOCAM Configuration
COLR	ISOCAM Off-Line Processing Report
CPER	ISOCAM ERD for parallel mode
CPSL	ISOCAM Point-Source List
CPSP	ISOCAM Standard Processed Data for parallel mode
CRPIXi	Reference pixels (as for the FITS keywords)
CSSP	ISOCAM Source Spectra
CSTA	ISOCAM Compact Status
CSWCVF	ISOCAM SW CVF description
CUFF	ISOCAM User-Friendly log File
CUS	Calibration Uplink System
CVF	Circular Variable Filter
CWHEELS	ISOCAM Wheel information table
DC	Digital Converter
DSS	Digitized Sky Survey
DFLT	Detector flat-field
DRK	Procedure when ISOCAM is performing a dark current measurement
EGSE	Electrical Ground Support Equipment
ERD	Edited Raw Data
EWHL	Entrance Wheel position
FCVF	Filter wheel position
FITS	Flexible Image Transport System
FLT	Flat-field
GST	Ground Station Time
GBPP	Ground Based Preparatory Programme
ICD	Internal Calibration Device
IDA	ISO Data Archive
IDL	Interactive Data Language
IDLE	Operating mode when ISOCAM is off
IDUM	Instrument Data Users Manual
IIPH	Instrument Instantaneous Pointing History
IRPH	Instrument Reference Pointing History
ISG	Instrument Support Group
ISO	Infrared Space Observatory
ISOCAM	Infrared Space Observatory instrument: camera
ITK	Instrument Time Key
LTT	Long Term Transient
LW	Long Wavelength channel of ISOCAM
MMT	Multi-resolution Median Transform
MOSFET	Metal-Oxide Semiconductor Field-Effect Transistor
N_{stab}	Number of stabilisation exposures
OBS	Procedure when ISOCAM is obtaining astronomical data
OBDH	On Board Handling System
OFLT	Optical flat-field
OLP	Off-Line Processing
OP-MODE	ISOCAM Operational mode
ORBIT	Orbital parameter file

OTF	On-Target Flag
PFOV	Pixel Field of View
PGA	Proposal Generation Aids
PI	Principal Investigator
POPS	Post-Operations Phase
PSF	Point Spread Function
QLA	Quick-Look Analysis
RATE	ADU/s
rms	root mean square
RTA	Real-Time Technical Assessment
SAO	Small Amplitude Oscillations
SCD	Standard Calibrated Data
SED	Spectral Energy Distribution
SPD	Standard Processed Data
SPDT	Survey Product Display Tool
SRF	Spectral Response Function
SW	Short Wavelength channel of ISOCAM
SWHL	Selection Wheel position
TDF	Telemetry Distribution file
TDT	Target Dedicated Time
TINT	Integration Time
UTC	Universal Time (conventional)
UTK	Uniform Time Key
ZB	Zodiacal Background

Bibliography

[1] Abergel A., Miville-Deschênes M.A., Désert F.-X., Pérault M.X., Aussel H. & Sauvage M. 1999, *The transient behaviour of the LW channel of ISOCAM*, ExA 10, 353

[2] Altieri B., Metcalfe L., Ott S., Pérault M. & Vigroux L. 1998, *CAM Calibration explanatory document*, Version 1.0, 2 October 1998 (see ISOCAM documentation under: `http://www.iso.vilspa.esa.es`)

[3] Altieri B., Metcalfe L., Kneib J.P. et al. 1999, *An ultra-deep ISOCAM observation through a cluster-lens*, A&A 343, L65

[4] Aussel H., Cesarsky C., Elbaz D. & Starck J.-L. 1999, *ISOCAM observations of the Hubble Deep Field with the PRETI method*, A&A 342, 313

[5] Biviano A., Sauvage M., Gallais P. et al. 1998a, *The ISOCAM Dark Current Calibration Report*, (see ISOCAM documentation under: `http://www.iso.vilspa.esa.es`)

[6] Biviano A., Altieri B., Blommaert J. et al., 1998c, *ISOCAM CVF Calibration Report*, Version 1.1, 20 May 1998 (see ISOCAM documentation under: `http://www.iso.vilspa.esa.es`)

[7] Biviano A., Blommaert J., Laurent O. et al. 1998b, *ISOCAM Flat-field Calibration Report*, Version 1.1, 19 May 1998 (see ISOCAM documentation under: `http://www.iso.vilspa.esa.es`)

[8] Biviano A. 1998d, *ISOCAM Calibration Error Budget Report*, Version 3.1, 14 August 1998 (see ISOCAM documentation under: `http://www.iso.vilspa.esa.es`)

[9] Biviano A., Sauvage M., Gallais P. et al. 2000, *The ISOCAM/LW detector dark current behaviour*, ExA 10, 255

[10] Blommaert J. 1998, *ISOCAM Photometry Report*, Version 2.1.1, 18 December 1998 (see ISOCAM documentation under: `http://www.iso.vilspa.esa.es`)

[11] Blommaert J., Metcalfe L., Altieri B. et al. 2000, *The ISOCAM responsivity in orbit. Standard star photometry*, ExA 10, 241

[12] Blommaert J., Boulanger F. & Okumura K. 2001a, *ISOCAM CVF Photometry Report*, IDC Report, SAI/2001-034/Rp

[13] Blommaert J., Okumura K. & Boulanger F. 2001b, *ISOCAM photometry*, in 'The Calibration Legacy of the ISO Mission', Eds. L. Metcalfe & M.F. Kessler, ESA SP-481 (in press)

[14] Boulade O. & Gallais P. 2000, *The ISOCAM detectors: an overview*, ExA 10, 227

[15] Claret A. & Dzitko H. 1998, *ISOCAM glitch library*, 30 June 1998, (see ISOCAM documentation under: `http://www.iso.vilspa.esa.es`)

[16] Claret A. & Dzitko H. 2001, *Understanding and Modelling glitch effects in ISOCAM*, in 'The Calibration Legacy of the ISO Mission', Eds. L. Metcalfe & M.F. Kessler, ESA SP-481 (in press)

[17] Claret A., Dzitko H., Engelmann J. & Starck J.-L. 2000, *Glitch effects in ISOCAM long wave detector*, ExA 10, 305

[18] Cohen M., Walker R.G. & Witteborn F.C. 1992, *Spectral irradiance calibration in the infrared. II. α Tau and the recalibration of the IRAS low resolution spectrometer*, AJ 104, 2030

[19] Cohen M., Witteborn F.C., Walker R.G., Bregman J.D. & Wooden D.H. 1995, *Spectral irradiance calibration in the infrared. IV. 1.2–35 micron spectra of six standard stars*, AJ 110, 275

[20] Cohen M., Witteborn F.C., Carbon D.F., Davies J.K., Wooden D.H. & Bregman J.D. 1996, *Spectral irradiance calibration in the infrared. VII. New composite spectra, comparison with model atmospheres, and far-infrared extrapolations*, AJ 112, 2274

[21] Coulais A. & Abergel A. 2000, *Transient correction of the LW-ISOCAM data for low contrasted illumination*, A&ASS 141, 533

[22] Coulais A. & Abergel A. 2002, *Frequently Asked Questions about Fouks-Schubert model and transient correction method for LW-ISOCAM*, in 'Exploiting the ISO Data Archive. Infrared Astronomy in the Internet Age', Eds. C. Gry, S.B. Peschke, J. Matagne et al., ESA SP-511 (in press)

[23] Coulais A., Fouks B.I., Giovanelli J.-F., Abergel A. & Sée J. 2000, *Transient response of IR detectors used in space astronomy: what we have learned from the ISO satellite*, in 'Infrared Spaceborn Remote Sensing VIII', Proc. SPIE 4131, 205

[24] Coulais A., Abergel A., Pérault M. & Fouks B. 2001, *What can be characterised for low-background IR detectors from ground-based experiments?*, in 'The Calibration Legacy of the ISO Mission', Eds. L. Metcalfe & M.F. Kessler, ESA SP-481 (in press)

[25] Decin L. 2001, *Stellar models in IR calibration*, in 'The Calibration Legacy of the ISO Mission', Eds. L. Metcalfe & M.F. Kessler, ESA SP-481 (in press)

[26] Decin L., Vandenbussche B., Waelkens C. et al. 2003a, *ISO-SWS calibration and the accurate modelling of cool-star atmospheres: II. General results*, A&A 400, 679

[27] Decin L., Vandenbussche B., Waelkens C. et al. 2003b, *ISO-SWS calibration and the accurate modelling of cool-star atmospheres. IV. G9 to M2 stars*, A&A 400, 709

[28] Delaney M. & Ott S. (Eds.) 2002, *ISOCAM Interactive Analysis User's Manual*, SAI/96-5226/Dc, Version 5.0

[29] Désert F.-X., Puget J.-L., Clements D., Pérault M., Abergel A., Bernard J.P. & Cesarsky C. 1999, *A classical approach to faint extragalactic source extraction from ISOCAM deep surveys. Application to the Hubble Deep Field*, A&A 134, 342

[30] Dzitko H., Claret A. & Engelmann J. 2000, *Cosmic ray effects on the ISOCAM LW detector*, ExA 10, 279

[31] Fouks B.I. 1992, *Non-stationary behaviour of low background photon detectors*, in 'Photon Detectors for Space Instrumentation', ESA SP-356, 167

[32] Fouks B.I. & Schubert J. 1995, *Precise theoretical description of the photoresponse for detectors of ISOPHOT's Si:Ga array*, Proc. SPIE 487, 2475

[33] Fouks B.I., Coulais A. & Normand, J. 2002, *Accurate physical model for direct modelling of point source transients for ISOCAM LW detector*, in 'Exploiting the ISO Data Archive. Infrared Astronomy in the Internet Age', Eds. C. Gry, S.B. Peschke, J. Matagne et al., ESA SP-511 (in press)

[34] *fv: The Interactive FITS File Editor*, available at:
`http://heasarc.gsfc.nasa.gov/docs/software/ftools/fv/`

[35] Gallais P. & Boulade O. 1998, *Report on trend analysis of CAM daily calibration measurements* (see ISOCAM documentation under: `http://www.iso.vilspa.esa.es`)

[36] Hammersley P.L., Jourdain de Muizon M., Kessler M.F. et al. 1998, *Infrared standards for ISO. I. A new calibration of mid infrared photometry*, A&AS 128, 207

[37] Hammersley P.L. & Jourdain de Muizon M. 2001, *The development of stellar photometric standards for ISO*, in 'The Calibration Legacy of the ISO Mission', Eds. L. Metcalfe & M.F. Kessler, ESA SP-481 (in press)

[38] Holtzman J.A., Burrows C.J., Casertano S., Hester J.J, Trauger J.T., Watson A.M. & Worthey G. 1995, *The photometric performance and calibration of WFPC2*, PASP 107, 1065

[39] Jourdain de Muizon M. & Habing H.J. 1992, *The ISO Ground-Based Preparatory Programme Working Group*, in 'Les Houches Series: Infrared Astronomy with ISO', Eds. Th. Encrenaz & M.F. Kessler, 129

[40] Kessler M.F, Müller T.G., Leech K. et al. 2003, *The ISO Handbook:Volume I, ISO – Mission & Satellite Overview* ESA SP-1262, SAI-2000-035/Dc, Version 2.0

[41] Miville-Deschênes M.A., Boulanger F., Abergel A. & Bernard P. 2000, *Optimising ISOCAM data processing using spatial redundancy*, A&AS 146, 519

[42] Moneti A., Metcalfe L. & Schulz B. 1997, *Reference Wavelengths for ISO: CAM and PHOT Filters*, SAI/97-002/Dc, Version 1.0

[43] *NOST standard 100-1.0*, available at:
`http://fits.gsfc.nasa.gov/`

[44] Okumura K. 1998, *ISOCAM PSF Report*, Version 1.0, 26 June 1998 (see ISOCAM documentation under `http://www.iso.vilspa.esa.es`)

[45] Okumura K., Pérault M. & Longval Y. 1998, *Ghosts in ISOCAM images*, Version 1.1, 4 November 1998, (see ISOCAM documentation under `http://www.iso.vilspa.esa.es`)

[46] Okumura K. 2000, *ISOCAM Field Distortion Report*, Version 1.0, 7 November 1998, (see ISOCAM documentation under `http://www.iso.vilspa.esa.es`)

[47] Omont A. and the ISOGAL Collaboration, 1999, *The ISOGAL Survey*, 'The Universe as Seen by ISO', Eds. P. Cox & M.F. Kessler, ESA-SP 427, 211

[48] Ott S., Metcalfe L., Pollock A. & Tuffs R. 2000, *Innovative cosmic ray rejection in ISOCAM data*, in 'Astronomical Data Analysis Software and Systems (ADASS) IX', Eds. N. Manset, C. Veillet & D. Crabtree. ASP Conf. Series 216, 543
(ASP, ISBN 1-58381-047-1)

[49] Pérault M., Omont A., Simon G. et al. 1996, *First ISOCAM images of the Milky Way*, A&A 315, L165

[50] Román P. & Ott S. 1999, *Report on the behaviour of ISOCAM LW darks*, Version 1.2, June 1999, (see ISOCAM documentation under `http://www.iso.vilspa.esa.es`)

[51] Sauvage M., Blommaert J., Boulanger F., Cesarsky C. & Cesarsky D.A. 1996, *ISOCAM mapping of the Whirlpool galaxy M51*, A&A 315, L89

[52] Saxton R.D. (Ed.), *ISO Data Product Document*, Issue 12, 8 June 2000, SAI/94-1266/Dc

[53] Schubert J., Roth G., Wolf J., Lemke D. & Fouks B.I. 1994, *Correction and curing of in-orbit-induced non-ideal behaviour of ISOPHOTS's photodetectors*, Proc. SPIE 2268, 283

[54] Siebenmorgen R., Abergel A., Altieri B. et al. 1996, *First results from the ISOCAM parallel mode*, A&A 315, L169

[55] Siebenmorgen R. 1999, *Polarisation observations with ISOCAM* in 'ISO Polarisation Observations', Eds. R.J. Laureijs & R. Siebenmorgen, ESA-SP-435, 41

[56] Siebenmorgen R., Schartel N. & Ott S. 2000, *The ISOCAM parallel mode* in 'ISO Surveys of a Dusty Universe', Eds. D. Lemke, M. Stickel & K. Wilke, Lecture Notes in Physics 548, 275.

[57] Starck J.-L., Murtagh F. & Bijaoui A. 1998, *Image Processing and Data Analysis: The Multiscale Approach*, Cambridge University Press, Cambridge (GB)
ISBN:0521590841

[58] Starck J.-L, Abergel A., Aussel H. et al. 1999a, *ISOCAM data processing*, A&AS 134, 135

[59] Starck J.-L, Aussel H., Elbaz D., Fadda D. & Cesarsky C. 1999b, *Faint source detection in ISOCAM images*, A&A 138, 365

[60] Tiphène D., Rouan D., Epstein G. & Le Coupanec P., 2000, *Modelling transient effects in the IR array of the short wavelength channel of ISOCAM* ExA 10, 347

[61] van der Bliek N.S., Bouchet P., Habing H.J. et al. 1992, *Standard stars for the Infrared Space Observatory, ISO*, The Messenger 70, 28

[62] Vinokurov L.A. & Fouks B.I. 1991, *Non-linear photoresponse of extrinsic photoconductors*, Sov. Phys. Semicond. 25, 1207

[63] Vigroux L.G., Cesarsky C., Boulade O. et al. 1993, *ISOCAM –the Infrared Space Observatory camera: results of testing and calibrations*, Proc. SPIE 1946, 281

[64] Walker R.G. & Cohen M. 1992, *An atlas of selected calibrated stellar spectra*, NASA Contractor's Report CR-177604

Index